



LAWRENCE
LIVERMORE
NATIONAL
LABORATORY

LLNL-TR-429029

Final Report LDRD 04-ERD-019

Development of absolute spectroscopic diagnostics for non-LTE plasmas

H. A. Scott

April 28, 2010

Disclaimer

This document was prepared as an account of work sponsored by an agency of the United States government. Neither the United States government nor Lawrence Livermore National Security, LLC, nor any of their employees makes any warranty, expressed or implied, or assumes any legal liability or responsibility for the accuracy, completeness, or usefulness of any information, apparatus, product, or process disclosed, or represents that its use would not infringe privately owned rights. Reference herein to any specific commercial product, process, or service by trade name, trademark, manufacturer, or otherwise does not necessarily constitute or imply its endorsement, recommendation, or favoring by the United States government or Lawrence Livermore National Security, LLC. The views and opinions of authors expressed herein do not necessarily state or reflect those of the United States government or Lawrence Livermore National Security, LLC, and shall not be used for advertising or product endorsement purposes.

This work performed under the auspices of the U.S. Department of Energy by Lawrence Livermore National Laboratory under Contract DE-AC52-07NA27344.

Final Report LDRD 04-ERD-019

Development of absolute spectroscopic diagnostics for non-LTE plasmas

H. A. Scott

Overview:

This project sought to further our understanding of non-Local Thermodynamic Equilibrium (NLTE) processes by providing benchmark data to validate computational models. This has been a difficult regime to study in the laboratory, where experimental scales produce strong gradients while interpretation requires well-characterized uniform plasmas. It has also been a difficult regime to simulate, as evidenced by the large discrepancies in predictions of NLTE spectra for fixed plasma properties. Not surprisingly, discrepancies between data and calculations of recombining laser-produced plasmas have been in evidence since the 1980's. The goal here was to obtain data of sufficient accuracy to help resolve these discrepancies and enable better modeling of the NLTE processes that are integral to high-energy density experiments.

Advances in target fabrication, diagnostic development and simulation capabilities provided the foundations for this project. Uniform plasmas were to be achieved by using aerogel foams of low enough density ($\sim\text{mg/cm}^3$) and thickness ($\sim\text{mm}$) to be volumetrically heated by a laser. The foams were doped with Ti to provide K- and L-shell emission and recombination spectra during the experiments. A new absolutely calibrated transmission grating spectrometer provided absolute temporal measurements at 18 frequencies, in addition to a CCD image of the time-integrated spectrum. Finally, atomic models of varying degrees of sophistication and detail, combined with NLTE radiation transport and hydrodynamics, were used to simulate the experiments and understand the observed spectra.

We give here a summary of the main achievements, challenges and results of this project. Details are available in the documents included as appendices.

Summary:

The first set of experiments was performed on the NIKE laser at NRL in March, 2004, with the goals of evaluating the performance of the diagnostics and the achieved plasma uniformity. By varying the laser parameters, we determined the required parameters for creating L-shell emission and were able to obtain K-shell (He-like) Ti. Pinhole x-ray images of the K-shell emission showed transverse plasma uniformity depended upon the target quality. Not all targets had acceptable quality, as it proved difficult to fabricate targets of the desired thickness ($\frac{1}{2}$ mm).

Using thicker targets also adversely affected the production of uniform conditions through the plasma, as the plasma was expected to have a moderate optical thickness ($\sim\text{few}$) to the laser radiation at early times during the laser pulse. Large differences in predictions of target

performance by different codes were traced to the differences in the calculation of laser absorption, and this is discussed at length in the reports from UCSD.

The first absolutely calibrated, time resolved L-shell emission spectra (from 4 to 26 Å) were also obtained in this series of experiments. The spectral resolution was not sufficient to match any individual spectral features. However, combined with the time resolution, it was sufficient to demonstrate that the emission shifted to lower photon energies later in time, consistent with the plasma recombining as it cooled.

Simulations of these targets produced time-integrated emission in 3 different wavelength bands that matched the experimental measurements within a factor of three and provided a constraint on the average plasma temperature. The simulations also found rise times for the spectral bands similar to those actually observed. However, the highly non-uniform plasma conditions along with the poor spectral resolution did not place any detailed constraints on the NLTE modeling.

The first set of experiments succeeded in mapping out the achievable plasma parameters and in identifying the major constraints and deficiencies due to target fabrication and experimental design. The second set of experiments was designed to provide increased spectral resolution, through modifications to the spectrometer, and increased plasma uniformity. Simulations predicted that illuminating the targets from two sides would provide good uniformity and still achieve the desired plasma temperatures with the decreased laser intensity achievable with this configuration. This also allowed the use of layered targets, with undoped foam regions sandwiching the doped foam to provide hydrodynamic tamping. Thomson scattering would provide an independent measurement of electron temperature in the plasma.

The second set of experiments, originally planned for the summer of 2005, was repeatedly delayed. Due to personnel and budget constraints, the additional temperature diagnostics were to be provided by thin layers of spectroscopic dopants rather than Thomson scattering. A set of experiments was finally performed in September 2006, just before the termination of this LDRD. No analysis has been done on the data obtained in these experiments.

This project did produce some significant achievements. The absolutely-calibrated spectrometer was successfully fielded, tested and improved. This unique instrument, which measured emission spectra with spatial, spectral and temporal resolution, has not been replicated elsewhere. The collaboration with UCSD trained two students in NLTE radiation-hydrodynamics simulations, with one student spending a summer at LLNL. This modeling effort, which encompassed several widely-used codes, uncovered significant differences between some codes and deficiencies in all codes, leading to a development effort to improve the performance of LLNL codes for this type of simulation. Concurrently, attempts to model the spectral data contributed to the improvements in NLTE atomic models made over the last several years.

Publications included as appendices:

1. C.A. Back, U. Feldman, J.L. Weaver, J. Seely, C. Constantin, G. Holland, R.W. Lee, H.-K. Chung and H.A. Scott, “Absolute, time-resolved emission of non-LTE L-shell spectra from Ti-doped aerogels”, JQSRT 99 (2006) 21.
2. M.S. Tillack, K.L. Sequoia, J. O’Shay, C.A. Back and H.A. Scott, “Optimization of plasma uniformity in laser-irradiated underdense targets”, Inertial Fusion Science and Applications 2005, Biarritz France, Sept. 2005.
3. C.A. Back, J.F. Seely, J.L. Weaver, U. Feldman, R. Tommasini, S.G. Glendinning, H.-K. Chung, M. Rosen, R.W. Lee, H.A. Scott, M. Tillack and J.D. Kilkenny, “Underdense radiation source: Moving towards longer wavelengths”, J. Phys. IV France 133 (2006) 1173.
4. K.L. Sequoia, M.S. Tillack, H.A. Scott, “A comparison of Hyades and Cretin for modeling laser absorption in underdense plasmas”, UCSD-CER-06-09 (2006).
5. M.S. Tillack, J. O’Shay, E.S. Simpson, C.A. Back and H.A. Scott, “Radiation-Hydrodynamic Analysis of Ti-Doped SiO₂ Aerogel Exposed to 4-ns Laser Irradiation”, UCSD-CER-05-01 (2005).

Absolute, time-resolved emission of non-LTE L-shell spectra from Ti-doped aerogels

C.A. Back^{a,*}, U. Feldman^b, J.L. Weaver^c, J.F. Seely^c, C. Constantin^a,
G. Holland^c, R.W. Lee^a, H.-K. Chung^a, H.A. Scott^a

^aLawrence Livermore National Laboratory, P.O. Box 808, L-21, Livermore, CA 94551, USA

^bArtep Inc. 2922 Excelsior Ct., Ellicott City, MD 21042, USA

^cNaval Research Laboratory, 4555 Overlook Drive, SW, Washington DC 20375, USA

Received 30 March 2005; accepted 25 April 2005

Abstract

Outstanding discrepancies between data and calculations of laser-produced plasmas in recombination have been observed since the 1980s. Although improvements in hydrodynamic modeling may reduce the discrepancies, there are indications that non-LTE atomic kinetics may be the dominant cause. Experiments to investigate non-LTE effects were recently performed at the NIKE KrF laser on low-density Ti-doped aerogels. The laser irradiated a 2 mm diameter, cylindrical sample of various lengths with a 4-ns square pulse to create a volumetrically heated plasma. Ti L-shell spectra spanning a range of 0.47–3 keV were obtained with a transmission grating coupled to Si photodiodes. The diagnostic can be configured to provide 1-dimensional spatial resolution at a single photon energy, or 18 discrete energies with a resolving power, $\lambda/\delta\lambda$ of 3–20. The data are examined and compared to calculations to develop absolute emission measurements that can provide new tests of the non-LTE physics.

© 2005 Elsevier Ltd. All rights reserved.

Keywords: Non-LTE; Ti L-shell emission; Laser-produced plasma; Transmission grating; Aerogel

*Corresponding author.

E-mail address: tinaback@llnl.gov (C.A. Back).

1. Introduction

The evolution of a non-local thermodynamic equilibrium (non-LTE) plasma is complex and can often be counter-intuitive. Many different and competing factors can cause departures from LTE. It is fairly straightforward to make analytic estimates to determine when an idealized uniform plasma becomes non-LTE because collisional rates are too low to ensure a Boltzmann distribution of the level populations. But even for a plasma with high densities where collisional rates are much larger than radiative rates, radiation fields that are not at the local temperature can drive a plasma out of LTE. For non-ideal plasmas, such as laboratory plasmas whose spatial size is finite and whose evolution is on time-scales comparable to, or even shorter than those of atomic processes, non-LTE physics can be very hard to avoid and very hard to simulate.

In this paper we present initial laser-produced plasma experiments to quantitatively measure Ti-L-shell spectra. The goal is to absolutely measure non-LTE plasma emission under well-characterized plasma conditions.

In order to illustrate why definitive absolute measurements of non-LTE plasmas are difficult to make, we briefly review three cases from the literature. First, earlier work showed the value of time-resolved diagnostics and target fabrication [1] by showing that there was improved agreement between simulations and data when emission was time-resolved and lateral plasma gradients were eliminated. However, even in this straightforward case where the optically thin K-shell emission was recorded, the late-time emission was not in agreement with calculations. This work concluded that the differences between the temporal data and calculations implied problems in simulating the energy transported along the target surface and/or the ionization balance.

Later experiments employed point projection to obtain time and space-resolved absorption measurements [2]. These experiments thus removed the axial gradient dependence and provided a more robust measurement of the ionization balance because it employed absorption to probe the ground states instead of relying on the emission from excited states, which contain a small fraction of the populations and, therefore, strongly depend on recombination rates and the details of the atomic model. These experimental results showed that at later times the ionization balances change slowly, comparing well with calculations. However, these experiments do not provide a benchmark for modeling because the temperature and density were not independently measured.

More recent measurements determine the ionization balance of Au by self-consistency between two independent observables: the time-resolved ion acoustic waves emitted from a localized position; and, the time-resolved emission spectra measured for a region where the temperature and density is bounded by other measurements [3]. After careful analysis, the measured ionization balance was found to be nearly one charge state higher than the calculations. Although multiple diagnostics were successfully fielded, a definitive reason for the discrepancy is still elusive. Probable causes, according to the authors, are inadequate atomic kinetics or the lack of steady-state conditions. It remains a challenge to simultaneously measure the parameters necessary to fully characterize non-LTE plasmas.

To design experiments to benchmark simulations, it is helpful to consider the approximations employed in the calculations. For many applications, a fluid dynamical description of the plasma is sufficient. Thus, in most simulations the temperature is “evolved” by estimating the change in the energy density of a simulation “cell” based on the local parameters. The macroscopic

quantities of electron temperature, T_e , electron density, N_e , and ion temperature, T_i , are derived from the energy density and then used to describe the plasma behavior.

The challenge of modeling non-LTE plasmas lays in the determination of T_e and N_e . Unlike the modeling of LTE plasmas where the ionization and density are related to the temperature through the Saha–Boltzmann equations, the modeling of a non-LTE plasma requires a detailed treatment of the collisional and radiative rates. Therefore, the simulations require an added level of complexity because they must retain and track level populations in order to properly compute the ionization, excitation, and free electron kinetics. Consequently, in contrast to LTE plasmas, no unique correspondence exists between the T_e and N_e for non-LTE plasmas.

Particularly, challenging cases occur when collisional coupling is dominant for the upper excited states, but not for the ground states. This condition often occurs in mid to high Z laser-produced plasmas that reach temperatures where significant ionization occurs for the L- or M-shell at electron densities on the order of 10^{20} – 10^{21} cm $^{-3}$. In these plasmas, radiative processes can significantly affect the ionization balance. Furthermore, radiative losses can be large, especially in laboratory plasmas. Therefore, not only the ionization balance, but also the emissivity of the plasma can be significantly affected by non-LTE kinetics. In these cases, plasma simulations often become computationally more expensive and often less self-consistent.

Benchmarking plasma simulations is difficult, but necessary. The on-going international non-LTE Kinetic Code Comparison workshops [4] have highlighted the fact that different codes produce disparate results for even relatively simple K-shell test cases. For ions with more electrons, such as those in laser-produced plasmas, the emission of L-shell, M-shell and even N-shell can affect the energy balance much more significantly than K-shell emission. Furthermore, as the Z of the element increases the complexity of the calculated atomic model also increases, compounding the difficulties. For example, a spectroscopically accurate description of a Ti L-shell ion, requires $>10^4$ levels. However, the representation of this ionic species within a radiation-hydrodynamic simulation requires a reduction in the number of levels to ~ 100 through the use of effective rates and intelligent level groupings. Approximations such as these, which are needed to render the atomic physics tractable for simulations, must be experimentally validated.

In these experiments, we study a plasma created by volumetrically heating a low-density Ti-doped aerogel targets. We have previously shown that gas-filled targets, having initial densities lower than the critical density of the incident laser, [5,6] absorb energy primarily through inverse Bremsstrahlung and form a uniform plasma. Fortunately, a significant advance in target fabrication has led to the production of silica aerogels with densities as low as 2 mg/cc that can be doped with mid- Z elements. Recent experiments have measured supersonic heat wave propagation in these aerogels, indicating that they are volumetrically heated before significant hydrodynamic motion affects the plasma, as was found for the gas-filled targets [7,8]. Thus, the density of the target is chosen to ensure volumetric heating, while the Z and concentration of the dopant are chosen for the desired wavelength and optical depth of the emission to be studied.

Given the need to reduce the number of levels by orders of magnitude for Li-like and any higher iso-electronic sequence ions for mid- and high- Z ions, a full validation of non-LTE radiation codes must examine the atomic data and population kinetics before testing the radiation transport algorithms. In these experiments we measure the absolute emission of optically thin systems in order to validate the atomic kinetics. We specifically choose to focus on the L-shell of Ti because computational developments and new algorithms now make possible a more complete physical

representation of these shells. In future experiments we will test the radiation transport by measuring emission from optically thick systems.

2. Experimental setup

The experiments were performed using the NIKE laser to create plasmas from cylindrical aerogel targets. The laser was configured to deliver up to 37 beams of 0.248 μm wavelength light incident within a cone angle of 12° from the axis of the cylinder. The intensity of the overlapped beams of the laser was varied from 1×10^{12} to $6 \times 10^{13} \text{ W/cm}^2$ by using different combinations of the spot size and number of beams on target. The average energy of a single beam for all shots was $\sim 42.5 \text{ J}$. For most comparisons of different targets, the beam spot size was fixed. In order to examine the spatial uniformity of the emission, the beam focal spot was varied by using apertures to produce 380, 750 and 940 μm diameter spots. The rise time of the laser pulse is $\sim 250 \text{ ps}$. Fig. 1 shows a schematic of the experimental setup and the location of the diagnostics.

The targets were low-density SiO_2 aerogels that were doped with 3 or 6 at% titanium. The material is produced by supercritically heating a mixture of titanium and silicon alkoxides above 250°C to remove the solvent. The resulting aerogel has a porous structure with cell sizes of $< 0.1 \mu\text{m}$. Being roughly comparable to the laser wavelength, this cell size is not expected to introduce significant structure in the heated plasma. A batch of 10–12 targets are made at one time by casting the aerogel into support glass rings with $\sim 2 \text{ mm}$ inner diameter, 1 or 2.2 mm length, and 200 μm thick.

Aerogel targets used in the experiment had mass densities of 2.5, 2.7, 3.0, and 8.0 mg/cc. A piece of aerogel from each batch of targets was used to determine the aerogel density to $\pm 0.1 \text{ mg/cc}$. In all cases, the laser spot from the cone of beams was focused within the central 1 mm diameter portion of the target on the front face. Alignment was performed by focusing a low-power HeNe alignment laser from a reference position on the target support and then translating the target to the correct position. When correctly aligned, the scattered light from the HeNe was visible along the axis of the aerogel.

The plasma emission was recorded by a set of spectral diagnostics: two time-resolved absolute transmission grating spectrometers, a time-integrated Bragg crystal X-ray spectrometer, the Henway; and two time-integrated pinhole cameras filtered for $> 4 \text{ keV}$ emission to monitor the Ti K-shell emission.

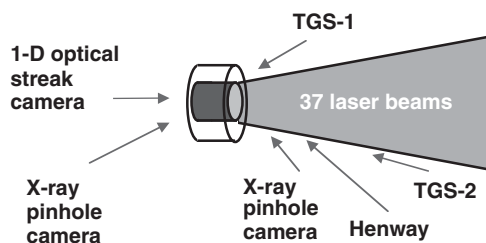


Fig. 1. Experimental setup showing the irradiation of a cylindrical target by 37 beams of NIKE and the diagnostics. The laser is incident on one face of the cylinder and typically illuminates the central mm of a 2 mm diameter target.

The transmission grating spectrometers (TGS) provided absolutely calibrated, time-resolved Ti L-shell emission measurements [9]. The TGS couples a transmission grating with linear Si photodiode arrays. The bandwidths of the diodes are determined by apertures in a stainless steel mask that are aligned with the photodiodes. Thus, each diode records a well-defined bandwidth of the dispersed X-rays.

The dispersed X-rays also fall onto a detector consisting of a phosphor, fiber optic, and CCD. The phosphor is $\sim 10\mu\text{m}$ of gadolinium oxysulfide doped with terbium deposited on a $1\mu\text{m}$ polypropylene film to make it sensitive to soft X-rays. This detector lies underneath the mask-diode combination and records a time-integrated spectral image together with the shadow of the mask apertures. In the non-spectral direction, the mask apertures are long enough to allow X-rays pass onto this detector as well as the diodes. The exact wavelength passing through the mask is sensitive to the position of the source, therefore, this image is valuable because it records the spatial relationship between the spectral wavelength and the diodes.

In order to show the relationship between the components, Fig. 2 shows the time-integrated CCD image, lineouts at different positions on the CCD, and the image of the time-resolved data reconstructed from the diodes. The CCD image shows the spectra relative to the shadows of two masks; one is above and the other is below the unobstructed spectra. The lineouts through the masked region are compared to the lineout through the unmasked region. In this way, the bandwidth of the signal recorded by each diode is unambiguously identified. The diode data is shown in Fig. 2 as a reconstructed image of the intensity as a function of wavelength on the horizontal axis, and time on the vertical axis. Since the zero order, the dispersed spectra, and the mask positions are recorded on the CCD, a precise in situ determination of the wavelength of the diodes is obtained for every experiment.

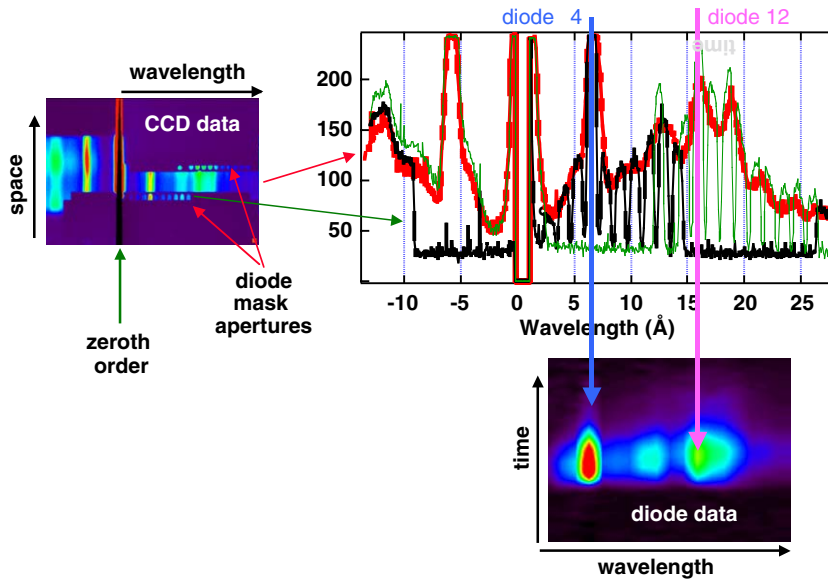


Fig. 2. Raw CCD images, lineouts, and an image of the data reconstructed from the diodes to display intensity as a function of wavelength and time. The diode wavelengths are known to high accuracy because the shadow of the diode mask apertures are visible on the CCD image.

The physical width of the diode aperture is 0.8 mm which corresponds to a $\delta\lambda$ for each diode of 1.23 Å. Over the L-shell emission, the resolution of the instrument varies from a resolving power of 21.2–3.2. At the peak of the Ti emission at 780 eV, the resolving power is 13.7. While at the peak of the Si K-shell emission, averaged over the $n = 2 - 1$ transitions, at 1878 eV, the resolving power is only 5.4. The diode signal is recorded on 1 GHz Tektronics TDG 684 scopes, which provide a temporal resolution of ~ 300 ps and a dynamic range of ~ 1000 . A timing fiducial pulse is recorded with the data on every experiment, so the temporal jitter between experiments is ~ 100 ps.

The analysis focused on data from the TGS-2 spectrometer, which is located in the vacuum enclosure, on a line-of-sight 14.3° from the target, just outside the 12° outer cone of the NIKE beams. This spectrometer has a 90 μm entrance slit and uses a 5000 l/mm Au transmission grating that was calibrated at the Brookhaven synchrotron light source [10]. The Si photodiodes are produced by International Radiation Detectors, Inc. and single 1 mm square diodes have also been calibrated [11]. The diodes in the array are assumed to have the same sensitivity as an individual diode, we therefore estimate the calibration to be within 10%.

Another TGS-1 spectrometer used a 2500 l/mm grating and was mounted on a fixed port at 42.2° from the aerogel axis. This grating was similarly calibrated and the measurements from this spectrometer were used to cross correlate the temporal and absolute value of the signals from TGS-2 [12,13].

The other diagnostics were used to assess the plasma conditions attainable at the NIKE laser. The Henway monitored the presence of Ti and Si K-shell emission giving a spectroscopic measure of peak temperatures. The pinhole cameras were used to monitor the spatial uniformity of the K-shell Ti emission.

3. Analysis of data

These experiments build on previous experiments that show aerogel targets can be volumetrically heated by a laser [7,8]. This illumination geometry is similar to the one-sided illumination, previously used at the Omega laser. However, the NIKE laser provides a 4 ns long pulse at a shorter wavelength. Therefore, these first experiments were designed to determine the accessible plasma conditions.

Overall, the analysis shows that we can successfully create low temperature L-shell emission at the minimum intensity in these experiments, $1 \times 10^{12} \text{ W/cm}^2$ and K-shell emission at a threshold intensity of $2.4 \times 10^{14} \text{ W/cm}^2$ or greater. The spectral diodes show that a wavelength shift is observed in the F- to He-like Ti emission as the plasma temperature increases. We expect conditions to span plasma temperatures in the range of 200–1000 eV.

We will discuss in detail the data from the TGS-2 diagnostic with respect to target types and laser fluence. However, time-integrated imaging diagnostics provided supplemental information. For instance, X-ray pinhole images filtered for $> 2 \text{ keV}$ X-rays showed significant lateral heating, i.e. heating in the direction perpendicular to the laser irradiated surface, takes place for the high-energy experiments where the emission is observed from volumes of the aerogel that are not directly illuminated by the laser. The time-integrated Bragg spectrometer data showed the presence of K-shell Ti emission for mid- and high-intensity experiments. However, for the lowest

laser intensities when the target is not sufficiently heated, the Ti K-shell and Si K-shell emission disappear.

Overall characteristics of the spectra can be examined by comparing the CCD and diode data with a series of calculations that span the range of the expected T_e of the plasma. Fig. 3 shows data on the top and Ti L-shell calculations on the bottom of the graph. In the upper half of the graph with the data, the lines represent the time-integrated CCD lineouts, while the symbols are the absolute emission measured simultaneously by the diodes at the time of peak intensity. The solid line is emission from the “high” fluence experiment which irradiated a 2.2 mm long, 3 at% Ti-doped 2.7 mg/cc aerogel with $5.7 \times 10^{13} \text{ W/cm}^{-2}$. This target produced the longest and brightest Ti L-shell emission. The dotted line is emission from the “low” fluence experiment which irradiated a 1.0 mm long, 6% Ti-doped 2.5 mg/cc aerogel at $4.6 \times 10^{12} \text{ W/cm}^{-2}$. The CCD lineouts are normalized to the absolute diode signals that were simultaneously obtained in the experiment. Because the diagnostic is linear in wavelength, the units for the spectra in this paper are consistently in erg/s/sr/\AA . Since we do not have time-resolved images of the source, the absolute measurements are not given per unit area, except in Fig. 8 where the source area is approximated by the laser focal spot.

The theoretical spectra are calculated for a 1 mm long uniform plasma created from a 2 at% Ti-doped 2 mg/cc aerogel. Since the resolving power of the CCD approaches 120, the calculated spectra are convolved with this instrumental resolution. The data in Fig. 3 shows that the CCD lineouts have significantly less spectral detail than the calculated spectra. For these experiments, the CCD spectra are comparable to those reconstructed from the diodes. The source broadening dominates the instrumental broadening for both.

The relative intensities of the spectra agree extremely well for the time-integrated CCD and time-resolved diode data. This means that the bulk of the emission is emitted while the plasma is in the ionization state it achieves at the peak emission for both “low” and “high” laser fluence

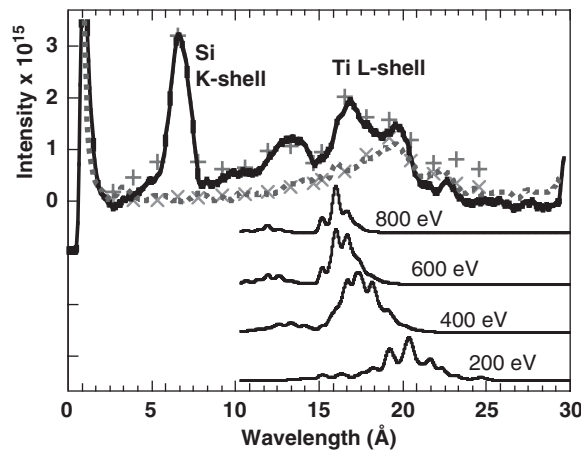


Fig. 3. Time-integrated intensity lineouts from the CCD and the diodes for the “high” (solid) and “low” (dashed) fluence cases discussed in the text. The lower energy laser shot produces a spectrum that peaks at longer wavelengths as expected. Synthetic spectra are also shown for a uniform plasma for an ion density of $6 \times 10^{19} \text{ cm}^{-3}$ and a plasma length of 1 mm.

experiments. This graph also shows that the peak of emission shifts to longer wavelengths as the incident laser energy decreases. Since the $T_e \sim I^{2/3}$, the shift to longer wavelengths is consistent with the plasma becoming cooler, as is demonstrated by the calculations.

The decrease in laser energy by a factor of 10 produces a ~ 5 factor produces a shift in the ionization balance and a decrease in the peak emission between the “high” and “low” fluence experiments. This large drop in the magnitude is not reflected in the calculations for the idealized plasma. The “high” and “low” fluence experiments use different targets, but the actual number of Ti atoms in the targets were comparable because the factor of 2 increase in dopant for the “low” fluence target was matched by the long 2.2 mm length and the 10% decrease in density of the “high” fluence target. Therefore, the steeper drop observed in the “low” fluence data when compared to the calculations may be an indication that the total source size was smaller because the laser does not efficiently heat the aerogel.

Fig. 4a shows the time-resolved spectra for the “high” fluence experiment. The spectra are virtually identical for 3.5–4.5 ns, meaning that the plasma achieves a steady state at end of the 4 ns long pulse. Fig. 4b shows spectra for every ns from 4 to 8 ns after the start of the laser. The data show the average ionization decreases and shifts to longer wavelengths during the cooling and recombination of the plasma.

Fig. 5a shows temporal histories of the same “high” fluence experiment for three wavelengths. The shortest wavelength, 6.6 Å is the K-shell Si emission and peaks ~ 2 ns. The temporal history

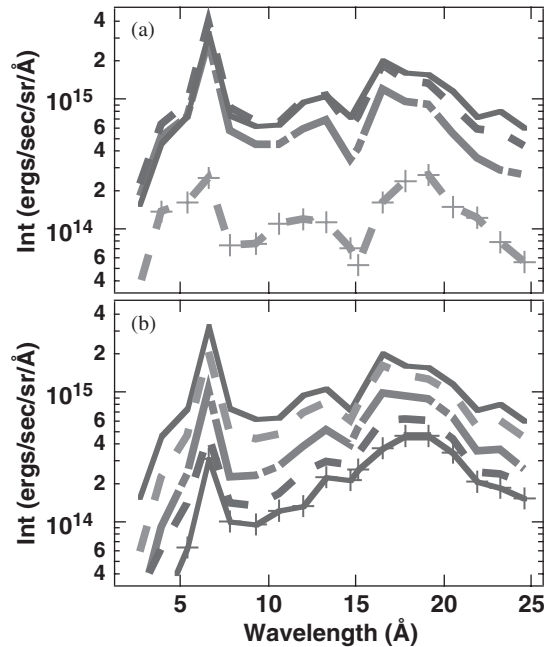


Fig. 4. Time-resolved spectra reconstructed from the diodes for the 1579 J shot onto the 2.2 mm long, 2.7 mg/cc, 3% Ti dopant aerogel. Lineouts in (a) are in order of increasing intensity, taken during the heating at 0.5, 1.5, 2.5, and 4.0 ns after the start of the laser pulse, and increasing in intensity to the peak of the pulse, (b) the spectra taken after the end of the laser pulse are shown at 4, 5, 6, 7, and 8 ns, decreasing monotonically from peak emission at 4 ns.

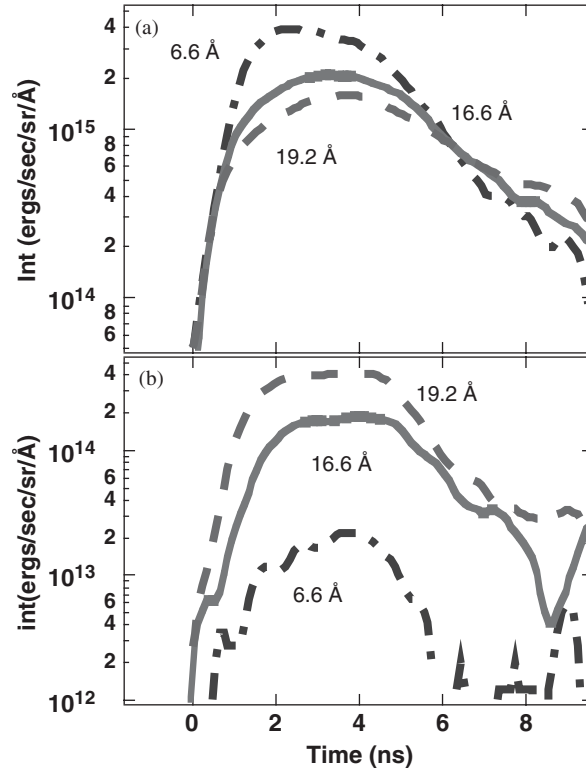


Fig. 5. Comparison of data at different photon energies from the same target. (a) “high” fluence target and (b) “low” fluence target.

indicates that opacity effects start to affect the K-shell emission and the measured emission is lower because the diagnostic is recording photons generated in the cooler expanding plasma boundary layer. On the other hand, the emission from the spectral peak of the Ti L-shell at 16.6 \AA gently rises and plateaus near the end of the pulse. It does not seem to be affected by optical depth effects. Relative to the 16.6 \AA emission, the longer wavelength Ti L-shell emission at 19.2 \AA , which is dominated by the higher ion charge states, tends to peak slightly later, and does not fall as fast after the end of the laser pulse.

In Fig. 5b we show the same temporal histories for the “low” fluence experiment. For the “high” fluence experiments, the onset of emission is immediate for all wavelengths. However, for the lower fluence experiments, the signals can start up to 0.8 ns late. The delay is particularly striking for the K-shell Si emission where the higher ionization potential requires a much hotter temperature to create the necessary ions. The relative temporal delay depends on the time-of-flight and cable length differences, which remain fixed for all the experiments. Due to the presence of the timing fiducial, the relative shifts in the onset of emission from different experiments on the same diode are accurate to $< 100 \text{ ps}$. Therefore the relative delays of the Si signal in the low fluence experiments are not artifacts or the diagnostic.

Comparisons of different targets show that the absolute emission does not necessarily vary as expected with the target composition. In Fig. 6, we show the 16.5 \AA (750 eV) emission as a

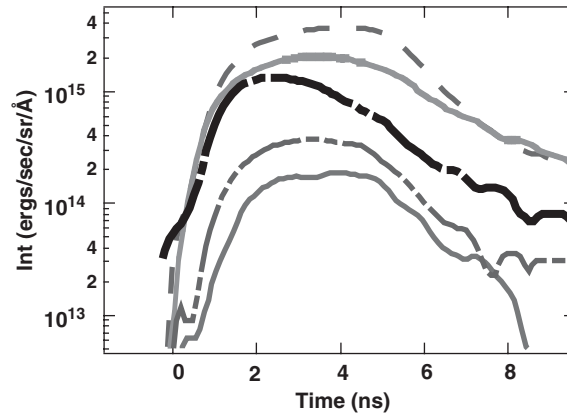


Fig. 6. Comparison of temporal histories for 16.6 Å (750 eV) emission from different targets. In order of increasing signal, the first three curves represent an energy scan on a 1 mm long 6 at% Ti-doped aerogel. The next curve (solid) is for maximum energy on a 2.2 mm long 3 at% Ti-doped aerogel. The last curve (dashed) is for a 2.2 mm long, 8 mg/cc density aerogel. Refer to the text for details.

function of time for different targets irradiated with the same laser spot size. The dotted–dashed lines represent a series of experiments with increasing laser fluence onto 1 mm long 6 at% Ti-doped aerogel targets. The lowest intensity curve is for the “low” fluence experiment defined before which had $4.6 \times 10^{12} \text{ W/cm}^2$ on target. The next two, in order of increasing intensity were both 3 mg/cc targets irradiated with 2.4×10^{13} and $5.7 \times 10^{13} \text{ W/cm}^2$, respectively. The solid curve is for the “high” fluence experiment already discussed before. The dashed curve is for a denser 8 mg/cc aerogel with a 2.2 mm length and 3 at% dopant concentration, irradiated with $5.7 \times 10^{13} \text{ W/cm}^2$. In general, we observe an increasing delay in the onset of emission as the laser fluence decreases.

For optically thin emission from the dopant, the absolute emission should increase in direct proportion to the increase in concentration of the dopant or the density of the material. However, the peak values of the curves show that this simple prediction does not hold. For instance, the magnitude of the signal for the 8 mg/cc target is a factor of 1.8 higher than the 2.7 mg/cc target, while the signal should have increased a factor of 3 based on the change in density. Since the focal spot and laser intensity were the same, it suggests that the higher density target was heated more transonically and lost more energy through electron conduction to the volume of plasma that was not directly irradiated by the laser.

The temporal histories give some indication of the physical size of the target that is being heated is not correlated with its length. The intensity of the 1 mm long target irradiated at maximum energy peaks before the end of the laser pulse. In fact, every wavelength peaks before the end of the pulse. This effect may indicate that hydrodynamics is playing a role during the 4 ns long laser pulse. Indeed, Si emission from shorter, 0.5 mm long undoped aerogels peaked even earlier in time and showed an even more pronounced erosion in the post-laser emission. This decrease during the pulse implies that axial rarefaction from the target may significantly affect the plasma emission for targets having lengths 1 mm or less.

Furthermore, for the mid-intensity fluence experiments, we compared the emission from targets of different length. We measured a virtually identical signal from a 1 mm long target and a 2.2 mm

long target for the same fluence and focal spot, which indicates that the laser is heating a volume of plasma equal to, or less than, 1 mm long. Since the signal comes to a near plateau at the end of the pulse, we conclude that this length is near the maximum that can be heated in this laser configuration.

In addition to allowing analysis of the temporal behavior and absolute intensity of the emission, the TGS also enables a crude measure of the temperature from the ratio of the O, Si, and Ti lines. Fig. 7 shows FLYCHK calculations using the ion density of the aerogel material [14]. Based on the ratio of the Si to Ti peak is extremely sensitive to temperature, even though the Si emission is optically thick. For the highest laser fluence, the temperature of the plasma is at least 400 eV. For the lower fluences, Si is calculated to disappear for $T_e < 300$ eV.

Finally, in Fig. 8 we show temporally resolved diode data as a function of wavelength at 4 ns. Here, we have reduced the data by subtracting out the Si and O contributions to the spectrum. To achieve this, we measured the Si and O contributions from a non-doped SiO₂ target of the same density and under the same laser irradiation conditions. The data compared to calculations show that the peak value shifts to lower temperature for the lower energy experiment as expected. Also, the absolute value of the data for the “high” fluence case is only a factor of 3 lower than calculations for a uniform plasma. Therefore, these results show a close agreement between the data and calculations.

These data are encouraging because they are consistent with our expectations of a non-LTE ionization balance. Calculations of the ionization balance produce significantly different results for non-LTE versus LTE or coronal models in the regime of temperature and density accessible to these experiments. In the density regime from 10^{18} – 10^{21} cm⁻³, both collisional and radiative processes play a role in determining ionization distributions. On the other hand, at sufficiently low electron density, the charge state distribution is independent of electron density. In this latter case,

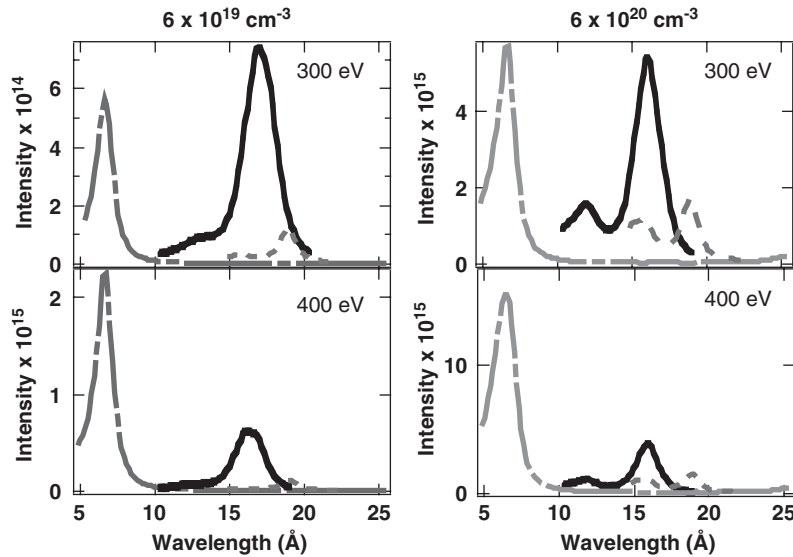


Fig. 7. FLYCHK calculations showing the sensitivity of Si, Ti, and O emission to the electron temperature and the ion density. The dotted-dashed, solid, and dashed lines represent the Si, Ti, and O, respectively.

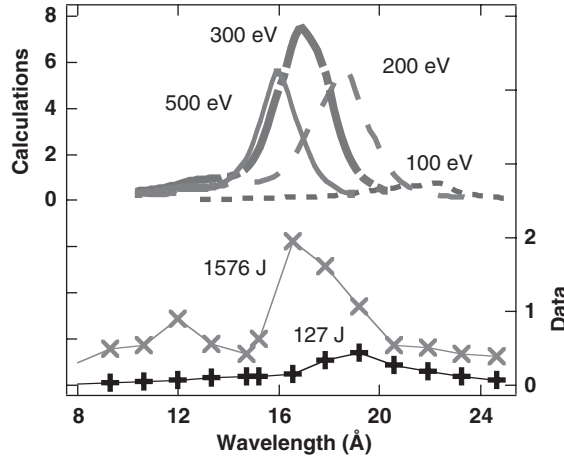


Fig. 8. Calculations and data reduced for the contribution of Ti alone for the “high” fluence and “low” fluence experiments. The values are intensity $\times 10^{17}$ in units of $\text{erg}/\text{cm}^2/\text{s}/\text{sr}/\text{\AA}$, where the area of the source is assumed to be the area of the $940\text{ }\mu\text{m}$ diameter focal spot. The calculations are for a plasma length of 1 mm and an ion density of $6 \times 10^{19}\text{ cm}^{-3}$ and are identified by their T_e .

the populations are determined by collisional ionization rates balanced by radiative and dielectronic recombination rates. At higher electron densities, collisional processes become dominant and the plasma moves toward the LTE state. At the intermediate densities that will be studied in these experiments, dielectronic recombination rates decrease and three-body recombination rates become competitive. In these conditions, the charge state distributions must be investigated with complete kinetics simulations and the complexity is exacerbated when there are numerous contiguous ionization stages without large variations in their ionization potentials, e.g., in L-shell ions.

In both cases, the width of the Ti emission indicates that there is a larger spread of ion species in the experimental data than in the calculations. Subsequent calculations of laser-heated targets performed by CRETIN [15] showed a factor of 2 difference in temperature between the illuminated and un-illuminated sides of the target. The calculated temperature drop is almost linear with the distance the heat wave propagates into the target. When inverse Bremsstrahlung is the dominant mechanism for the absorption of laser energy, the temperature is correlated with the intensity in the beam. Thus, as the beam propagates into the material, the intensity and the temperature decrease. Qualitatively, calculations also show that a delay in the onset of the emission is predicted. This onset is sensitive to the atomic physics model more than the T_e history and is currently under study. Future experiments will be partly focused on reducing the temperature gradient by using a two-sided illumination into the target.

4. Conclusions

These experiments to benchmark non-LTE kinetic codes use a laser to volumetrically heat an underdense target to create a plasma that emits predominantly in the soft X-ray regime. The

experimental goal is first to measure the absolute spectral emission from a plasma that has a uniform temperature and density and is in steady-state. Next, we will compare these data with predictions from simulations that are constrained by the measured temperature and density.

The data have been analyzed to determine the range of temperature and density conditions attainable by the NIKE laser, the signal levels, and the spectral resolution necessary for further studies. In the next experiments, we plan to reduce axial gradients by using tamped targets and also increase the spectral resolution of the primary diagnostic by improving the masks and adding a source-limiting aperture. We also have plans to include a time-resolved X-ray streak camera to monitor the K-shell emission simultaneously with the L-shell emission. Due to the high absolute sensitivity of the spectrometer, we eventually hope to measure spectral features with intensities that are small compared to the underlying continuum, e.g., emission from forbidden transitions.

Acknowledgments

We especially thank Steven Obenschain and the entire NIKE crew for their support of this work. In addition, we thank the target fabrication specialists, Joe Satcher and John Poco, who were instrumental in developing and fabricating these low-density-doped aerogel. Additional support from Tom Walsh and Mike Wilson for target assembly also helped make these experiments a success.

This work was performed under the auspices of the US Department of Energy (DOE) by the University of California, Lawrence Livermore National Laboratory (LLNL) under Contract No. W-7405-Eng-48. The project (04-ERD-019) was funded by the Laboratory Directed Research and Development Program at LLNL.

References

- [1] Kauffman RL, Lee RW, Estabrook K. Dynamics of laser-irradiated planar targets measured by X-ray spectroscopy. *Phys Rev A* 1987;35:4286.
- [2] Back CA, Chenais-Popovics C, Renaudin P, Geindre JP, Audebert P, Gauthier JC. Study of K α absorption structures in a subcritical-density laser-produced plasma. *Phys Rev A* 1992;46:3405.
- [3] Glenzer SH, Fournier KB, Wilson BG, Lee RW, Suter LJ. Ionization balance in inertial confinement fusion hohlraum. *Phys Rev Lett* 2001;87 045002–1.
- [4] Lee RW, Nash JK, Ralchenko Y. Review of the NLTE kinetics code workshop. *JQSRT* 1997;58:737.
- [5] Back CA, Grun J, Decker C, Suter LJ, Davis J, Landen OL, Wallace R, Hsing WW, Laming JM, Feldman U, Miller MC, Wuest C. Efficient multi-keV underdense laser-produced plasma radiators. *Phys Rev Lett* 2001;87:275003.
- [6] Back CA, Davis J, Grun J, Suter LJ, Landen OL, Hsing WW, Miller M C. 2003, multi-keV X-ray conversion efficiency in laser-produced plasmas. *Phys Plasmas* 2003;10:2047.
- [7] Fournier KB, Constantin C, Poco J, Miller MC, Back CA, Suter LJ, Satcher J, Davis J, Grun J. Efficient multi-keV X-ray sources from Ti-Doped aerogel targets. *Phys Rev Lett* 2004;92 165005–1.
- [8] Constantin C, Back CA, Fournier KB, Gregori G, Landen OL, Glenzer SH, Dewald EL, Miller MC. Supersonic propagation of ionization waves in an under-dense laser-produced plasma. *Phys Plasmas* 2005;12:063104-1.
- [9] Weaver JL, Colombant DG, Mostovych AN, Busquet M, Feldman U, Klapisch M, Seely JF, Brown C, Holland GE. An experimental benchmark for improved simulation of absolute soft X-ray emission from polystyrene targets irradiated with the Nike laser. *Phys Rev Lett* 2005;94 045002–1.

- [10] Seely JF, Brown C, Holland GE, Hanser F, Wise J, Weaver JL, Korde R, Viereck RA, Grubb R, Judge DL. Calibration of an extreme-ultraviolet transmission grating spectrometer with synchrotron radiation. *Appl Opt* 2001;40:1623.
- [11] Seely JF, Boyer CN, Holland GE, Weaver JL. X-ray absolute calibration of the time response of a silicon photodiode. *Appl Opt* 2002;41:5209.
- [12] Weaver JL, Holland GE, Feldman U, Seely JF, Brown CM, Serlin V, Deniz AV, Klapisch M. The determination of absolutely calibrated spectra from laser produced plasmas using a transmission grating spectrometer at the NIKE laser facility. *Rev Sci Instrum* 2001;72:108.
- [13] Weaver JL, Feldman U, Seely JF, Holland GE, Serlin V, Klapisch M, Colombant D, Mostovych A. Absolutely calibrated, time-resolved measurements of soft X-rays using transmission grating spectrometers at the Nike laser facility. *Phys Plasmas* 2001;8:5230.
- [14] Chung HK, Chen MH, Morgan WL, Lee RW. FLYCHK: simple but generalized population kinetics and spectral model. *High Energy Density Physics* 2005;1:1.
- [15] Scott HA. Cretin—a radiative transfer capability for laboratory plasmas. *JQSRT* 2001;71:689.

Optimization of plasma uniformity in laser-irradiated underdense targets*

M. S. Tillack¹, K. L. Sequoia¹, J. O'Shay¹, C. A. Back² and H. A. Scott³

¹*University of California San Diego, 9500 Gilman Drive, La Jolla CA, 92093-0438, USA*

²*General Atomics, P.O. Box 85608, San Diego CA, 92186-5608, USA*

³*Lawrence Livermore National Laboratory, P.O. Box 808, Livermore CA, 94561, USA*

Abstract. We used the Hyades [1] and Helios [2] radiation-hydrodynamic simulation tools, and the Cretin atomic kinetics code [3] to model low-density SiO₂ aerogel carriers doped with trace amounts of Ti and subjected to high-energy pulsed laser irradiation. Underdense targets are expected to respond to laser irradiation more uniformly as compared with solid targets, and therefore provide a better platform upon which to perform measurements of the properties of warm dense matter. We report modeling results for several cases of interest, with laser intensities in the range of 5×10^{12} – 6×10^{13} W/cm², SiO₂ densities in the range of 2–8 mg/cm³ and Ti doping in the range of 0–6%. Recommendations are given for the conditions under which relatively uniform temperature and density can be obtained.

1. INTRODUCTION

Studies of the properties of warm dense matter using lasers are complicated in part due to difficulties interpreting data from targets that evolve rapidly and contain large spatial gradients during irradiation. This is especially true in non-LTE plasmas, whose emissions depend on the complex time-dependent evolution of excited states. Clean, well-characterized benchmark data are needed in order to validate models of atomic processes in these plasmas.

Analyses were performed to help guide experimental studies of the radiative properties of non-LTE laser plasma such as those described in [4]. In that work, Ti L-shell spectra were measured in order to help resolve discrepancies between data and models of plasmas in recombination. Two experimental cases were considered: a “low-fluence” case at 4.6×10^{12} W/cm² using a 1-mm thick target containing 2.5 mg/cc of SiO₂+6 at% Ti, and a “high-fluence” case at 5.7×10^{13} W/cm² using a 2.2-mm thick target containing 2.7 mg/cc of SiO₂+3 at% Ti. In all modeling cases, the laser wavelength was 248 nm and the intensity ramped from zero to full intensity in 0.2 ns, remained flat for 3.6 ns and then ramped down to zero in 0.2 ns.

In order to isolate individual effects, we first examined a base case with pure SiO₂ at 2.5 mg/cc and laser intensity of 4.6×10^{12} W/cm², and then individually explored the effect of doping and laser intensity. Different models of radiation transport and ionization were evaluated. Finally, alternative target designs were analyzed using 2-sided illumination with and without end caps.

*work supported through LLNL Agreement #B551392 authorized under Prime Contract W-7405-ENG-48 from DOE/NNSA.

2. PHYSICS MODELS

In underdense targets, inverse bremsstrahlung is the primary mechanism for energy absorption. Figure 1 shows the absorption length for several electron densities and temperatures. Limitations in target fabrication prevent us from fielding targets with thickness less than ~ 1 mm and density below ~ 2 mg/cc, which corresponds to about $5 \times 10^{20} \text{ cm}^{-3}$ in SiO_2 . Under these conditions, plasma temperatures below 300 eV are difficult to heat entirely by direct illumination.

In any case, radiation emission plays an important role in the energy balance. These plasmas are fully non-LTE, as verified by the McWhirter condition and results of modeling, which indicate much slower electron-ion collision frequency as compared with mean radiative transition rates. Hyades [1] and Helios [2] were used to examine radiation transport; these are commercially available 1D Lagrangean radiation hydrodynamic simulation tools. In both cases, multi-group radiation transport was used; Helios utilizes spectrally resolved opacity data (from the PROPACEOS code), whereas Hyades employs a hydrogenic model of the atoms.

Obtaining uniform density in underdense targets is significantly easier than obtaining uniform temperature. Non-LTE Cretin simulations show that $Z_{\text{eff}} \sim 8$ at 100 eV, indicating SiO_2 has been stripped to the K-shell. Above this temperature, the average charge state gradually increases to 10. For laser intensities below 10^{14} W/cm^2 , simulations show that hydrodynamic expansion during the laser pulse is small enough that the density is determined by the charge state. Above 10^{14} W/cm^2 the hydrodynamic expansion is so rapid that uniform densities can not be maintained.

Figure 2 highlights one of the primary difficulties in non-LTE modeling of underdense targets. The retained internal energy (including electrons, ions, radiation and kinetic energy) is plotted together with the energy escaped by radiation for several different cases using pure SiO_2 . Hyades and Helios predict substantially different amounts of retained energy when multi-group transport is used. In general, Helios plasmas retain more energy, leading to higher observed electron temperatures.

Hyades provides several options for the ionization model. These include Saha, LTE average atom and non-LTE average atom. Figure 3 shows the electron temperature profile for several combinations of opacity and ionization models for the low-fluence case (the target is originally between 0 and 1 mm). Direct experimental measurements of temperature are not available, but the spectroscopic data suggest that a temperature of ~ 200 eV is appropriate for the low-fluence experimental conditions. More data are needed in order to better understand the model results. At this time, we are continuing to explore the sensitivities of the results to the models in order to help design the next set of experiments.

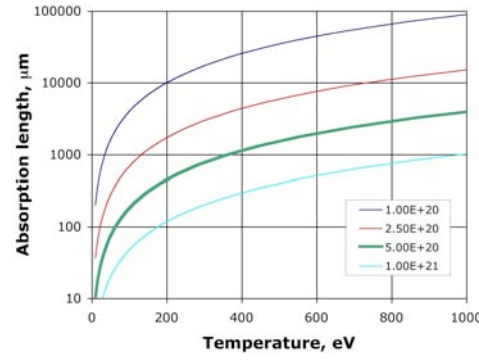


Figure 1. Inverse bremsstrahlung absorption length for underdense SiO_2

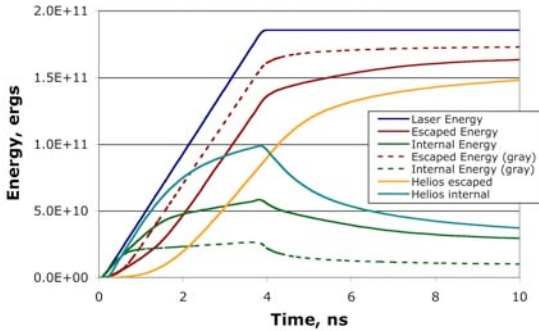


Figure 2. Energy balance for low-fluence cases

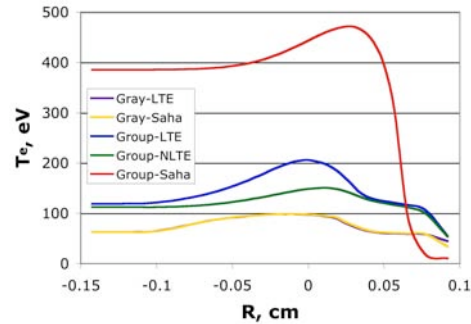


Figure 3. Hyades temperatures obtained using different physics models at 2 ns

3. EFFECT OF DOPING, LASER INTENSITY AND ALTERNATIVE TARGET DESIGNS

As seen in Figure 4, the addition of a dopant, even at the relatively low levels used here, results in significant reductions in temperature, and the spatial gradients become larger. The spectrally resolved opacity shows differences primarily for photon energies around 800 eV. In most cases we observe that higher opacity degrades the temperature uniformity. Since opacity generally decreases with temperature, we might expect that the high fluence case would have more uniform profiles. Figure 5 shows temperature profiles at 2.5 ns (high-fluence case with 2.2 mm target), and tends to confirm this.

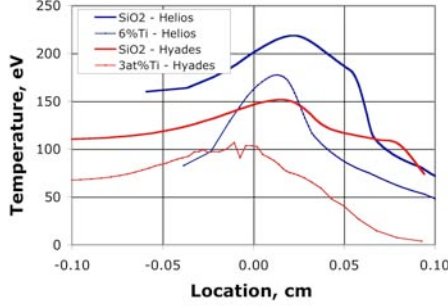


Figure 4. Effect of doping on temperature at 2.5 ns

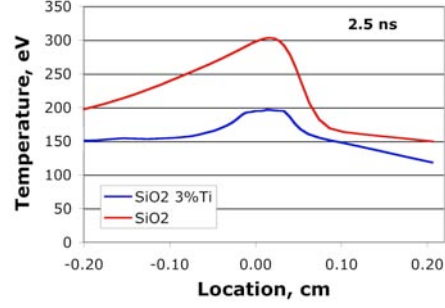


Figure 5. Hyades result at $5.7 \times 10^{13} \text{ W/cm}^2$

As shown above, uniform heating of targets is possible when the temperature is sufficiently high to reduce the optical depth at the laser wavelength, but achieving uniform temperatures becomes increasingly difficult at lower intensities when the electron temperature remains below 300-400 eV. A straightforward technique to improve the uniformity is to use 2-sided irradiation. We explored two such geometries. First we divided the energy of the low-fluence case into two equal counterpropagating parts striking a 1-mm SiO_2 target (Fig. 6). In the second example (Fig. 7) we used a 3% doped core surrounded by 0.5-mm undoped side regions. In both of these geometries the profiles improved.

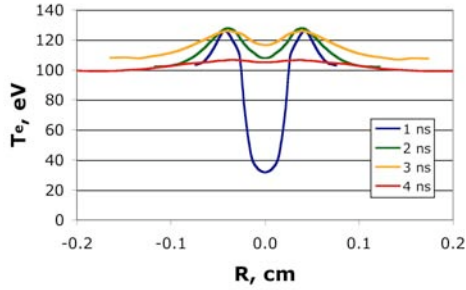


Figure 6. Electron temperature with double-sided illumination

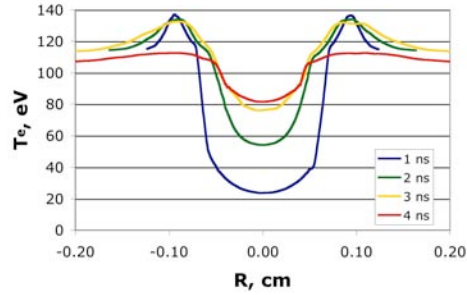


Figure 7. Electron temperature for the "pillbox" target

References

- [1] J. T. Larsen and S. M. Lane, "HYADES – A plasma hydrodynamics code for dense plasma studies," *Journal of Quantitative Spectroscopy & Radiative Transfer* **51** (1994) 179-186.
- [2] I. E. Golovkin, J. J. MacFarlane, P. R. Woodruff, L. A. Welser, D. L. McCrorey, R. C. Mancini, J. A. Koch, "Modeling of Indirect-Drive ICF Implosions using 1D Hydrodynamic Code with Inline Collisional-Radiative Atomic Kinetics," *IFSA 2003*, Monterey CA, Sept. 2003, 166-169.
- [3] H. A. Scott, "Cretin – a radiative transfer capability for laboratory plasmas," *Journal of Quantitative Spectroscopy & Radiative Transfer* **71** (2001) 689-701.
- [4] C.A. Back, U. Feldman, J.L. Weaver, J.F. Seely, C. Constantin, G. Holland, R.W. Lee, H.-K. Chung, H.A. Scott, "Absolute, time-resolved emission of non-LTE L-shell spectra from Ti-doped aerogels," *Journal of Quantitative Spectroscopy & Radiative Transfer* (available online, June 2005).

Underdense radiation sources: Moving towards longer wavelengths

C.A. Back¹, J.F. Seely², J.L. Weaver², U. Feldman³, R. Tommasini⁴,
S.G. Glendinning⁴, H.-K. Chung⁴, M. Rosen⁴, R.W. Lee⁴, H.A. Scott⁴,
M. Tillack⁵ and J.D. Kilkenny¹

¹ General Atomics, PO Box 85608, San Diego, California 92186-5608, USA

² Naval Research Laboratory, 4555 Overlook Drive, Washington, DC 20375, USA

³ Artep Inc., 2922 Excelsior Ct., Ellicott City, MD 21042, USA

⁴ Lawrence Livermore National Laboratory, PO Box 808, Livermore, California 94551, USA

⁵ U. C. San Diego, 9500 Gilman Drive, La Jolla, CA 92093, USA

Abstract. Underdense radiation sources have been developed to provide efficient laboratory multi-keV radiation sources for radiography and radiation hardening studies. In these plasmas laser absorption by inverse bremsstrahlung leads to high x-ray conversion efficiency because of efficient ionization of the low density aerogel or gas targets. Now we performing experiments in the soft x-ray energy regime where the atomic physics models are much more complicated. In recent experiments at the NIKE laser, we have irradiated a Ti-doped SiO₂ aerogel with up to 1650 J of 248 nm wavelength light. The absolute Ti L-shell emission in the 200-800 eV range is measured with a diagnostic that uses a transmission grating coupled to Si photodiodes. We will give an overview of the temporally-resolved absolutely calibrated spectra obtained over a range of conditions. Eventually we hope to extend our studies to x-ray production in the EUV range.

1. INTRODUCTION

Accurate understanding of x-ray production mechanisms is essential for design and fabrication of x-ray sources that are used for backlighting, material testing and EUV lithography. Although the x-ray production is important, the physical processes that contribute to this essentially non-LTE regime are difficult to study because plasma gradients profoundly affect the physical observables. The outstanding discrepancy between data and calculations of laser-produced plasmas in recombination has been in evidence since the 1980's [1]. Predictions of the x-ray source duration, importantly for times greater than the laser pulse duration are inaccurate. While the problem might be in the hydrodynamics, there are also indications that non-LTE atomic kinetics may be the dominant cause of discrepancies. Recent international workshops on non-LTE kinetics have uncovered vast discrepancies in predictions from 16 different codes for plasma temperature and density cases that were chosen for relevance to laboratory plasma studies [2]. The inability to accurately model x-ray laser recombination schemes is a prominent illustration that the models are incomplete.

At the temperatures and densities of typical laser-produced plasmas, the emission of L-shell, M-shell and even N-shell can affect the energy balance much more significantly than K-shell emission. In addition, as the Z of the element increases, the complexity of the calculated atomic model also increases. For instance, a relatively complete model of a Ti Li-ion can have up to 20,000 levels. An approximate model of the same ion stage may need to be reduced to approximately 100 levels in order to run simulations with the current computational capabilities. Figure 1 shows a comparison of the Ti L-shell lines calculated by a detailed atomic physics code, HULLAC, compared to those calculated using FLY. Although simpler models may allow for reasonably accurate calculation of energy balance, this figure

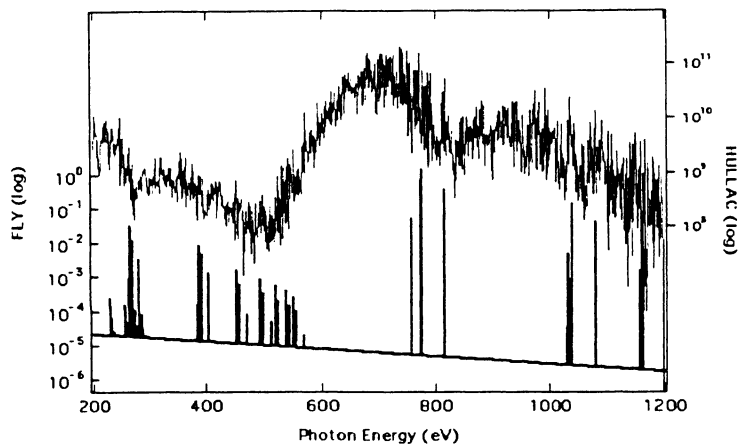


Figure 1. Calculations of Ti L-shell spectra by HULLAC (top) and FLY (bottom) for $T_e = 400 \text{ eV}$ and $n_e = 10^{21} \text{ cm}^{-3}$.

shows that the richness of the spectra is lost in the simpler model. Clearly, there is a need for data to validate the reduced models.

2. NON-LOCAL THERMODYNAMIC EQUILIBRIUM EXPERIMENTS

The experiments were performed using the NIKE laser to create plasmas from cylindrical aerogel targets. The laser was configured to deliver up to 37 beams of $0.248 \mu\text{m}$ wavelength light incident within a cone angle of 12° from the axis of the cylinder. The intensity of the overlapped beams of the laser was varied from 1×10^{12} to $5 \times 10^{13} \text{ W/cm}^2$ by using different combinations of the spot size and number of beams on target. The average energy of a single beam for all shots was $\sim 42.5 \text{ J}$. The risetime of the laser pulse is $\sim 250 \text{ ps}$.

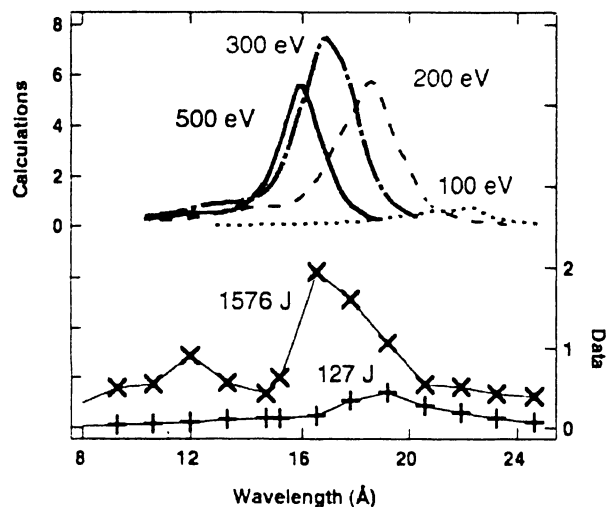


Figure 2. Calculations and data for a Ti-doped aerogel heated by the NIKE laser. The calculations are for a 1 mm long plasma having an ion density of $6 \times 10^{19} \text{ cm}^{-3}$ and are identified by their electron temperature. The values of intensity on the vertical axes are $\times 10^{17}$ in units of $\text{ergs/cm}^2/\text{sec}/\text{sr}/\text{\AA}$.

The use of low density aerogel foams ~ 3 mg/cc doped with 3-6 at.% Ti permit us to measure the temporal evolution of the K and L-shell emission of highly-ionized species. Under these laser conditions, the foams are volumetrically heated [3, 4] [5] [6]]. The primary diagnostic was a transmission grating spectrometers (TGS) that provided absolutely calibrated, time-resolved Ti L-shell emission measurements [7]. Figure 2 shows the temporally resolved data as a function of wavelength at 4 ns. Here we have reduced the data by subtracting out the Si and O contribution to the spectrum as measured from a non-doped SiO_2 target of the same density and under the same laser irradiation conditions. The data compared to calculations shows that the peak value shifts to lower temperature for the lower energy shot.

3. CONCLUSIONS

These experiments provide valuable L-shell spectra that can be analyzed to determine the ionization balance, the absolute emissivity and the temporal dependence of the plasma. In the future, higher spectral resolution will enable the creation of benchmarks that will be used to refine and validate the non-local thermodynamic equilibrium models.

Acknowledgment

The authors thank S. Obenschain and the NIKE laser crew for their support. This work was performed under the auspices of the U.S. Dept. of Energy by the Univ. of California, Lawrence Livermore National Laboratory under contract No. W-7405-ENG-48. The project (04-ERD-019) was funded by the LDRD Program at LLNL.

References

- [1] P.G. Burkhalter, *et al.*, Phys. Fluids **26**, 3650 (1983).
- [2] R.W. Lee, J.K. Nash, Y. Ralchenko, J. Quant. Spec. Radiat. Transfer **58**, 737 (1997).
- [3] C.A. Back, J. Grun, C. Decker, *et al.*, Phys. Rev. Lett. **87**, 275003 (2001).
- [4] C.A. Back, J. Davis, J. Grun, *et al.*, Phys. Plasmas **10**, 2047 (2003).
- [5] K.B. Fournier, C. Constantin, J. Poco, *et al.*, Phys. Rev. Lett. **92**, 165005-1 (2004).
- [6] C. Constantin, C.A. Back, K.B. Fournier, *et al.*, Phys. Plasmas **12**, 063104 (2005).
- [7] J.L. Weaver, D.G. Colombant, *et al.*, Phys. Rev. Lett. **94**, 045002-1 (2005).

**A comparison of Hyades and Cretin
for modeling laser absorption in
underdense plasmas**

K. L. Sequoia, M. S. Tillack and H. A. Scott

6 December 2006



Center for Energy Research
University of California, San Diego
9500 Gilman Drive
La Jolla, CA 92093-0417

A comparison of Hyades and Cretin for modeling laser absorption in underdense plasmas

K. L. Sequoia¹, M. S. Tillack¹, H. A. Scott²

¹*University of California San Diego, 9500 Gilman Drive, La Jolla CA, 92093-0438, USA*

²*Lawrence Livermore National Laboratory, P.O. Box 808, Livermore CA, 94561, USA*

Abstract. In a laser produced plasma (LPP), the temperature and density profile and history are determined by the laser energy absorbed by the plasma. Therefore, it is extremely important that the absorption coefficients are calculated accurately when modeling LPP's. We have compared the inverse bremsstrahlung absorption coefficients of the radiation-hydrodynamic code Hyades [1] with the non-LTE atomic kinetics / radiation transfer code Cretin [2]. We found that the absorption coefficients disagree at relatively low electron temperatures (1-100 eV), and then begin to converge as the temperature rises above 100 eV. These discrepancies lead to a dramatically different temperature and density evolution of the LPP.

1. INTRODUCTION

It is difficult to model LPP's due to their rapid evolution and sharp spatial gradients. In addition, these plasmas are often non-LTE so that textbook equations for the ionization balance, radiation field, and velocity distribution no longer apply. Instead, detailed tracking of populations, through rate equations, is necessary to model LPP's. Several codes have been developed in an attempt to model non-LTE plasmas, but there is uncertainty in the codes' ability to predict radiative properties of non-LTE plasmas. In order to validate the modeling, experimental data must be collected from a clean, well characterized plasma for comparison.

The experimental design calls for SiO₂ aerogel targets with 3 at% Ti to be volumetrically heated by a laser [3]. The density of the targets is 3 mg/cc. The density was made as low as possible so that the laser could penetrate to the center of the target, and so that the plasma would be optically thin to the radiation produced from the plasma.

Hyades [1], a radiation-hydrodynamics code, simulations were used to guide the experimental activities. Simulations were performed to predict the electron temperature, T_e , achieved for various laser intensities. Temperatures of a few hundred eV are needed to create L-shell emission from Ti, which is the emission to be studied in this project. The Hyades results showed large temperature gradients that were not expected with the laser intensity and target design. This led to an investigation of the laser absorption model in Hyades and a comparison with the model in Cretin [2], a non-LTE atomic kinetics / radiation transfer code.

2. HYADES LPP RESULTS

The target is 2 mm thick, with 0.5 mm thick outer regions, which contain no Ti, as shown in

Figure 1. Figure 2 shows the electron temperature profile for a prospective target. A laser, with an intensity of $2.3 \times 10^{12} \text{ W/cm}^2$, is incident on each side of the target to allow for uniform heating. The much lower temperature in the central region is an indication that the laser is only heating the outer portion of the target, and that reradiation and conduction provide the heating for the doped region. This is confirmed in Figure 3 where the laser absorption is plotted as a function of position. If this is true, then the experiment cannot provide useful data for benchmarking the non-LTE codes. However, it has been demonstrated that the laser penetrates an aroge target to heat volumetrically [4,5]. The fact that the laser was fully absorbed in the first 0.5 mm of the target suggests that the absorption model is over predicting the inverse bremsstrahlung absorption (IBA) coefficient.

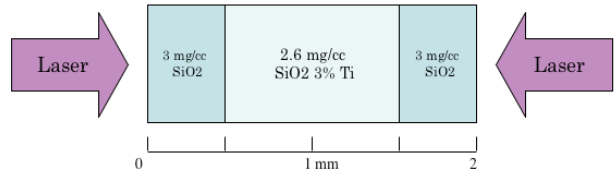


Figure 1. The target geometry is a doped core with an undoped tamping layer on the outside.

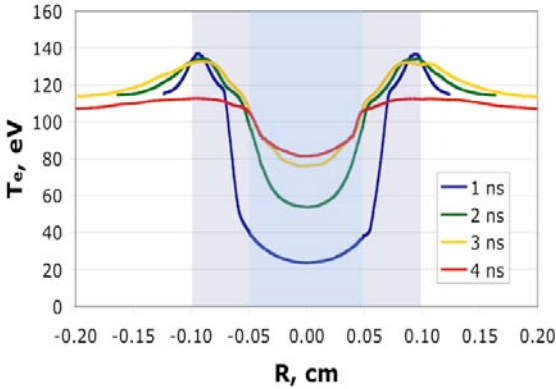


Figure 2. The temperature profile of the target showing the outer undoped region getting hot while the central doped region remains too cool.

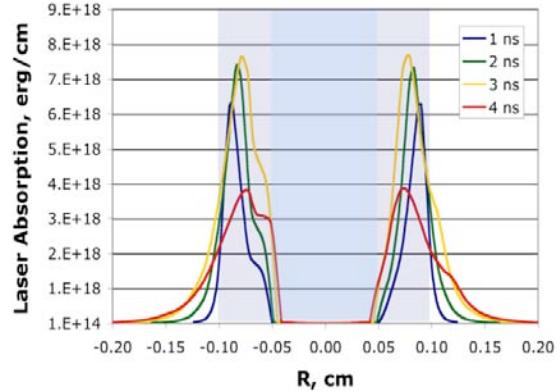


Figure 3. Showing that the laser only penetrates the outer layers of the target.

To determine if the IBA coefficient in Hyades was really the problem, a comparison case between Hyades and Cretin was made. A test case was constructed by turning off any physics in the codes that could have an affect on the temperature and absorption, fixing the temperature to a value relevant to the experimental studies, 700 eV, and introducing a laser of the appropriate intensity, $5 \times 10^{12} \text{ W/cm}^2$. The modeled target was composed of four, 25 micron thick SiO_2 zones. The mass density was set to 3 mg/cc. Four zones were designated since this is the minimal number of zones allowed in Hyades. The targets were made thin so that each region would see nearly the same laser intensity. We then compared the laser energy absorbed in each code, shown in Figure 4. It is obvious here that there is a disagreement in the IBA between Hyades and Cretin.

The discrepancies in the IBA in the test case led to a more thorough investigation to compare the temperature dependence for the absorption coefficients. Similar cases to the test case were run for the range of temperatures that would be encountered in the experimental campaign. In Figure 5, it can be seen that Hyades has a much higher absorption than Cretin at low temperatures. The

difference reduces as the temperature increases, but is still a factor of two even at 1 keV. The most dramatic difference occurs around 6 eV where Hyades is 20 times higher than Cretin. Additionally, Hyades shows an increase in the absorption with temperature from 1 to 6 eV. It should be mentioned that Hyades was not intended to work in the temperature and density ranges in question, and that there is little question of its accuracy in the regime where it was intended to work.

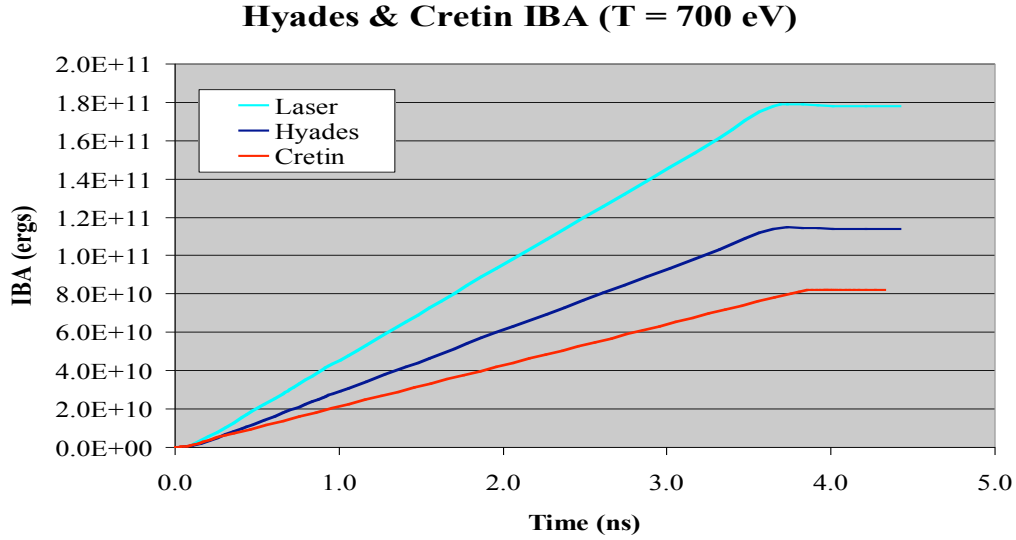


Figure 4. A comparison of Hyades and Cretin IBA for a underdense SiO_2 aerogel target at 700 eV

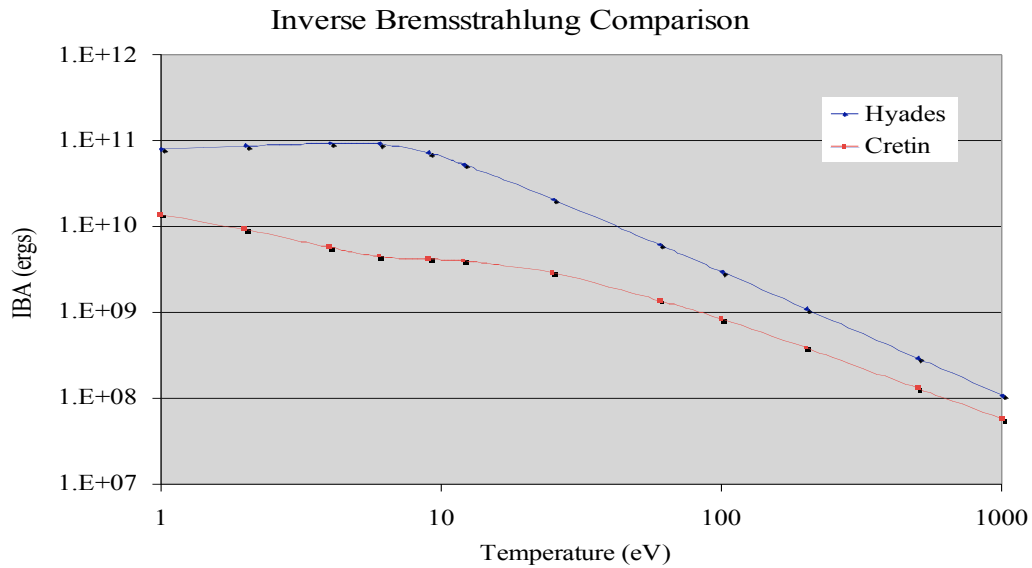


Figure 5. The temperature dependence of the IBA for Hyades and Cretin

3. HYADES IBA prescription

There are two reasons for the higher absorption in Hyades. The first is related to an approximation made to the stimulated emission term in the IBA calculation. Equation (1) is the prescription used in Hyades. The $T_e^{3/2}$ dependence comes from an approximation that is only valid for $kT_e \gg h\nu$. Equation (2) indicates how the IBA could be calculated if this approximation was not used. This approximation leads to the narrowing differences between the two codes at T_e increases, and the relatively large differences at low T_e .

$$\alpha = const * \frac{\langle n_i (Z^*)^2 \rangle n_e}{T_e^{3/2} \omega_0^2 \sqrt{\epsilon'}} \ln \Lambda_{ei} \quad (1)$$

$$\alpha = const * \left(1 - \exp\left(\frac{-h\nu}{kT}\right) \right) \frac{\langle n_i (Z^*)^2 \rangle n_e}{h\nu T_e^{1/2} \omega_0^2 \sqrt{\epsilon'}} \ln \Lambda_{ei} \quad (2)$$

$$\ln \Lambda_{ei} = \frac{1}{2} \ln \left[\max \left\{ 2, 1 + \frac{b_{\max}^2}{b_{\min}^2} \right\} \right] \quad (3)$$

$$b_{\max}^2 = \max \{ \chi_D^2, R_o^2 \} \quad (4)$$

$$b_{\min}^2 = \frac{h^2}{48\pi^2 m_e kT_e}$$

$$\ln \Lambda_{ei} = \frac{1}{2} \ln \left[1 + \frac{b_{\max}^2}{b_{\min}^2} \right] \quad (5)$$

The second problem lies in the calculation of the Coulomb logarithm, $\ln \Lambda_{ei}$, for which the Hyades formula is given in equation (3-4). Calculating the Coulomb logarithm this way leads to an over estimate for lower temperatures. This compounds the over estimation already caused by the stimulated emission approximation. In contrast, Cretin calculates the Coulomb logarithm using equation (4-5).

4. Summary and Conclusions

We have shown that Hyades predicts higher than expected laser absorption. This results in over heating of the outer zones of the illuminated target, while the inner zones are only heated by conduction and reradiation. The reason Hyades over predicts the laser absorption is that an approximation is made for the stimulated emission and an error in the Coulomb logarithm. However, at high values of T_e , the IBA in Hyades will be accurate since these affects are only important below about 2 keV.

The plasma uniformity and peak temperatures were of key importance for the modeling of laser irradiated aerogels. The overestimate of the IBA makes Hyades inaccurate for these low density and temperature conditions. Cretin was used, instead of using Hyades to calculate the temperature and density profiles. The ability to do Hydrodynamic calculations was added to Cretin in order to account for plasma expansion.

References

- [1] J. T. Larsen and S. M. Lane, “HYADES – A plasma hydrodynamics code for dense plasma studies,” *JQSRT* 51, 179-186 1994.
- [2] H. A. Scott, “Cretin – a radiative transfer capability for laboratory plasmas,” *JQSRT* 71, 689–701 2001.
- [3] C. A. Back, U. Feldman, J. L. Weaver, J. F. Seely, C. Constantin, G. Holland, R. W. Lee, H.-K. Chung, H. A. Scott, “Absolute, time-resolved emission of non-LTE L-shell spectra from Ti-doped aerogels,” 99, 21-34 2006.
- [4] K. B. Fournier, C. Constantin, J. Poco, M. C. Miller, C. A. Back, L. J. Suter, J. Davis J. Satcher, J. Grun, “Efficient multi-keV X-ray sources from Ti-Doped aerogel targets,” *Phys Rev Lett* 92, 165005 2004.
- [5] C. Constantin, C. A. Back, K. B. Fournier, G. Gregori, O. L. Landen, S. H. Glenzer, E. L. Dewald, M. C. Miller, “Supersonic propagation of ionization waves in an under-dense laser-produced plasma,” *Phys Plasmas* 12, 063104 2005.
- [6] Y. T. Lee, R. M. More, “An electron conductivity model for dense plasmas,” *Phys. Fluids* 27, 1273-1286, 1984.

Radiation-Hydrodynamic Analysis of Ti-Doped SiO₂ Aerogel Exposed to 4-ns Laser Irradiation

**M. S. Tillack, J. O'Shay, E. S. Simpson,
C. A. Back and H. A. Scott**

10 January 2005



Center for Energy Research
University of California, San Diego
9500 Gilman Drive
La Jolla, CA 92093-0420

Radiation-Hydrodynamic Analysis of Ti-Doped SiO₂ Aerogel Exposed to 4-ns Laser Irradiation

10 January 2005

M. S. Tillack, J. O'Shay,¹ E. S. Simpson
UC San Diego

Mechanical and Aerospace Engineering Department

¹ Electrical and Computer Engineering Department

C. A. Back and H. A. Scott
Lawrence Livermore National Laboratory

Abstract

We used the Hyades [1] and Helios [2] radiation-hydrodynamic simulation tools to explore the response of low-density SiO₂ aerogel carriers doped with trace amounts of Ti and subjected to high-energy pulsed laser irradiation. At sufficiently low density, these targets are expected to respond to laser irradiation more uniformly as compared with solid targets, and therefore provide a better platform upon which to perform measurements of the properties of hot dense matter. In this report we describe our initial modeling results for several cases of interest, with laser intensities in the range of 4.9×10^{12} to 3.7×10^{14} W/cm², SiO₂ densities in the range of 2 to 8 mg/cm³ and Ti doping in the range of 0 to 6%.

Table of Contents

1. Background
 - 1.1 Problem description
 - 1.2 Codes and modeling options
 - 1.3 Overview
2. Base Case Analysis
 - 2.1 Base case results for pure SiO₂ at 4.9×10^{12} W/cm²
 - 2.1.1 Hyades base case results
 - 2.1.2 Helios base case results
 - 2.2 Effect of opacity models on the base case results
 - 2.2.1 Opacity models and averaging techniques
 - 2.2.2 Comparison of Hyades results with Planck vs. Rosseland averaging
 - 2.2.3 Comparison of Hyades and Helios models using identical (gray) Sesame data
 - 2.2.4 Attempts at spectrally resolved results with Hyades
 - 2.2.5 Comparison of gray vs. spectrally-resolved opacities in Helios
3. Variation of parameters
 - 3.1 Addition of dopant
 - 3.1.1 Gray opacity results with Hyades
 - 3.1.2 Spectrally resolved results with Helios
 - 3.2 Increase in SiO₂ density from 2 to 8 mg/cm³
 - 3.3 Decrease of thickness to 0.5 mm
 - 3.4 Increase of laser intensity from 4.9×10^{12} W/cm² to 3.7×10^{14} W/cm²
 - 3.4.1 High intensity Hyades results
 - 3.4.2 High intensity Helios results, with and without doping
4. Summary and conclusions

Acknowledgements

Appendices

- A. Original statement of work
- B. Input and source files
 - B.1 Hyades base case input file
 - B.2 Source listing for spectral averaging routine
 - B.3 Source listing for Sesame mixture generator

List of Figures

1. Electron temperature history at 50 equal-mass zones for the Hyades base case
2. Electron density history at 50 equal-mass zones for the Hyades base case
3. Electron temperature spatial profile at 2.5 ns for the Hyades base case
4. Time history of laser flux in the outermost half of the target for the Hyades base case
5. Charge state history at 50 equal-mass zones for the Hyades base case
6. Electron density spatial profile at 2.5 ns for the Hyades base case
7. Time history of the radial location of the Lagrangian zones for the Hyades base case
8. Electron temperature history at 100 equal-mass zones for the Hyades base case
9. Electron density history at 100 equal-mass zones for the Hyades base case
10. Electron temperature history for the Helios base case
11. Internal and radiated energy for the Hyades base case
12. Internal energy for the Helios base case
13. Radiated energy for the Helios base case
14. Electron density history for the Helios base case
15. Electron temperature spatial profile at 2.5 ns for the Helios base case
16. Electron density spatial profile at 2.5 ns for the Helios base case
17. Comparison of Rosseland and Planck Sesame opacity for SiO₂
18. Comparison of single-group Sesame and Propaceos data with Planck averaging
19. Comparison of single-group Sesame and Propaceos data with Rosseland averaging
20. Hyades electron temperature at 2.5 ns using single-group Planck averaging
21. Electron density history for Helios using Sesame gray opacity and EOS
22. Electron density spatial profile at 2.5 ns for Helios using Sesame gray opacity and EOS
23. Electron temperature history for Helios using Sesame gray opacity and EOS
24. Electron temperature spatial profile at 2.5 ns for Helios using Sesame gray opacity and EOS
25. Electron temperature history using the Hyades group radiation transport module
26. Charge state history using the Hyades group radiation transport module
27. Electron temperature history from Helios using a single radiation group
28. Comparison of electron temperature profiles using one or 500 radiation groups
29. Rosseland mean opacity for SiO₂, Ti and a mixture of SiO₂-6%Ti
30. Internal energy EOS for SiO₂, Ti and a mixture of SiO₂-6%Ti

31. Electron temperature profile at 2.5 ns for SiO₂-6%Ti using gray opacities in Hyades
32. Electron density profile at 2.5 ns for SiO₂-6%Ti using gray opacities in Hyades
33. Electron temperature history for SiO₂-6% Ti using Helios
34. Electron temperature spatial profile at 2.5 ns for SiO₂-6% Ti using Helios
35. Electron temperature spatial profile at 2.5 ns for SiO₂-2% Ti using Helios
36. Electron density spatial profile at 2.5 ns for SiO₂-6% Ti using Helios
37. Contour plot of electron density for the 6% Ti case
38. Time history of laser flux in the outermost 10 nodes of the 8 mg/cm³ target
39. Electron density history for the 8 mg/cm³ target
40. Electron temperature history for the 8 mg/cm³ target
41. Mesh radiative heat flux as a function of time for the 8 mg/cm³ target
42. Time history of laser flux in the 0.5-mm thick, 2 mg/cm³ target
43. Electron temperature history for the 0.5-mm target
44. Electron temperature profile at 2.5 ns for the 0.5-mm target
45. Electron density profile at 2.5 ns for the 0.5-mm target
46. Electron temperature profiles at various times with 3.7×10^{14} W/cm² laser intensity
47. Electron density profiles at various times with 3.7×10^{14} W/cm² laser intensity
48. Time history of the charge state with 3.7×10^{14} W/cm² laser intensity
49. Radial location of the Lagrangian zones with 3.7×10^{14} W/cm² laser intensity
50. Time history of the laser flux with 3.7×10^{14} W/cm² laser intensity
51. Electron temperature history for SiO₂-6% Ti using Helios
52. Electron temperature spatial profile at 2.5 ns for SiO₂-6% Ti using Helios
53. Electron temperature spatial profile at 2.5 ns for SiO₂-0% Ti using Helios
54. Electron density spatial profile at 2.5 ns for SiO₂-6% Ti using Helios
55. Electron temperature history for SiO₂-6% Ti using Helios with gray opacities

1. Background

1.1 Problem description

A new project was initiated at LLNL during 2004 to develop absolute spectroscopic diagnostics. The research involves experiments and theory aimed at investigating atomic kinetics of highly ionized plasmas. The experiments use low-density SiO₂ aerogel foams that permit measurement of the temporal evolution of the K and L-shell emission of highly-ionized species using new absolute spectroscopic diagnostics. The data are expected to be sufficiently accurate to enable the creation of benchmarks, which can be used to refine and potentially validate the non-local thermodynamic equilibrium (NLTE) models used at LLNL and other research laboratories. In particular, recombination processes with electron densities in the range of 10^{19} to 10^{22} cm⁻³ for mid-Z elements will be addressed in experiments where an independent measure of the electron temperature is made for a sample with a well-known initial mass density. The experiments will provide *temporally-resolved absolute* measurements of the emission over a spectral range of 200 to 1000 eV.

This project addresses long-standing discrepancies in the study of laser-produced plasmas. Discrepancies between data and calculations of laser-produced plasmas in recombination have been evident since the 1980's. [3] One example of a large discrepancy is in predictions of the x-ray source duration for times greater than the laser pulse duration. The problem might be in the hydrodynamics; however, there are indications that non-LTE atomic kinetics may be the dominant cause of discrepancies. Recent international workshops on non-LTE kinetics have uncovered major disagreements in predictions from 16 different codes for plasma temperature and density cases that were chosen for relevance to laboratory plasma studies. [4] The inability to accurately model x-ray laser recombination schemes is a prominent illustration that the models are incomplete.

In order to help interpret the results of experiments, we have begun to model low-density doped aerogels using available numerical models. Radiation-hydrodynamic simulations were performed using Hydades [1] and Helios [2] over a range of parameters for laser intensities from 4.9×10^{12} to 3.7×10^{14} W/cm². Different modeling options were explored, with a particular emphasis on radiation transport and atomic physics models, in order to determine their relative importance and the need for more sophisticated modeling in the future. All of the modeling results presented in this work assume local thermodynamic equilibrium (LTE).

1.2 Codes and modeling options

Models of the behavior of high-Z dense laser plasmas include one or more of the following three components in order to characterize the material responses:

- (1) The basic hydrodynamics and energy transport. This includes laser absorption models, hydrodynamic models which utilize tabulated or computed equations of state for pressure and internal energy, and a radiation energy transport model. Radiation hydrodynamic codes often make simplifications for the radiation emission and transport, and may assume local thermodynamic equilibrium. Examples of radiation transport algorithms include flux-limited diffusion or multi-angle short characteristics.
- (2) Equation of state and opacity data or models. EOS and opacity data are essential in order to provide an accurate prediction of plasma responses. They can be obtained from databases, such as Sesame, or generated internally by the software package. Opacity data may be spectrally resolved or spectrally averaged (*i.e.*, “gray”).
- (3) A time-dependent collisional radiative (CR) solver for non-LTE plasmas. CR models require data on the relevant atomic processes which influence the ionization, excitation and emission of atoms, including:
 - Collisional ionization, recombination, excitation, and deexcitation
 - Photoionization and stimulated recombination
 - Photoexcitation and stimulated emission
 - Spontaneous decay
 - Radiative recombination
 - Dielectronic recombination, autoionization, and electron capture.

The codes solve rate equations for the evolution of the various atomic levels. For mid to high Z elements, the large number of transitions usually requires some form of simplification, or “compression”, of the data.

One of the codes we used for our plasma analysis is Hyades [1]. HYADES is a one-dimensional, three-temperature, Lagrangian hydrodynamics and energy transport code. The electron and ion components are treated separately in a fluid approximation and are loosely coupled to each other, each in thermodynamic equilibrium and described by Maxwell-Boltzmann statistics. Radiative energy transport is treated in a single-group (gray approximation) or in a multi-group prescription; in the former, the radiation is assumed Planckian, and the latter model allows for small departures from a pure Planckian. Hence, the multi-group method may be used to include some atomic shell effects and crude x-ray line effects. The radiation is coupled only to the electron fluid. The diffusion approximation is used for modeling all energy transport phenomena. The degree of ionization is determined by a Saha, Thomas-Fermi, LTE average-atom, time-dependent or steady-state nonLTE average-atom, or fully stripped models.

The thermodynamic and equation of state quantities are derived from realistic (Sesame or other theoretical models) tables, an in-line quotidian equation of state (QEOS), or an ideal gas model. Likewise, the tabular Rosseland mean and Planck mean opacities used in the gray radiation transport model are obtained from reasonable models. The hydrodynamic motion is treated in the Lagrangian formalism since the plasma may expand to cover a large spatial extent, as well as ranging over several orders of magnitude in density. In the Lagrangian prescription, the mesh moves with the material; that is, each elemental mass (zone) is conserved for all time. In contrast is the Eulerian prescription in which the mesh stays fixed and the material moves through it.

The other code we used in our analysis is Helios [2]. Helios is a 1-D radiation-hydrodynamics code developed by Prism Computational Sciences Inc. The hydrodynamic models are similar to Hyades. EOS and opacity data can be obtained from Sesame, but the default uses EOS and spectrally resolved opacity data obtained from the PROPACEOS code (PRism OPACity and Equation Of State code). PROPACEOS computes data for LTE plasmas or optically thin non-LTE plasmas. A full CR version of Helios is available, in which basic atomic data is supplied by the ATBASE suite of codes. In the work presented here, we have included only LTE cases.

1.3 Overview

The primary goal of this numerical study is to characterize the response of low-density Ti-doped aerogels irradiated in experiments at the Janus and Nike laser facilities. The set of parameters to be investigated is summarized in Table I. For all cases the laser source term remained the same: 248 nm light ramping up in 0.2 ns, flat top for 3.6 ns, followed by a 0.2 ns rampdown.

Table I. Experimental laser and target parameters

Case #	Description	Ti wt%	SiO ₂ density (mg/cm ³)	laser intensity (TW/cm ²)
0	modeling base case	0	2	4.9
1	experimental base case	2	2	4.9
2	high Ti dopant case	6	2	4.9
3	high SiO ₂ density case	2	8	4.9
4	thin target case	2	2	4.9
5	high laser intensity case	2	2	370
6	high intensity, high doping	6	2	370

Due to uncertainties in the validity of the numerical models in the codes and the sensitivity of the results to modeling assumptions, we first examined a “modeling base case” consisting of pure SiO₂. This is labeled “Case 0” in the table. In all other respects it is identical to the experimental base case. We explored the grid dependence, radiation transport model and the source of opacity data for Hyades, and compared the results with Helios.

After fully characterizing the modeling base case, we performed parametric variations by changing one parameter at a time. First, the Ti dopant level was increased from 0 to 6 wt%. After that, the target initial density was increased by a factor of 4. Based on our observations of strong laser absorption in this and the base case, we added a case with a thinner (0.5 mm) target in order to explore the effect of the optical depth with respect to the incident laser. Finally, the laser intensity was increased to 3.7×10^{14} W/cm².

Key parameters that we examined in the analysis included electron temperature, electron density, charge state and laser flux vs. time and zone. We are looking for the plasma to achieve a relatively uniform electron density during the laser pulse, and a relatively uniform temperature. This

should also lead to a relatively uniform average charge state in the plasma. Finally, we are interested to determine whether the incident laser is penetrating effectively into the underdense plasma, or if heating of the rear side of the target is dominated by conduction and/or radiation from the front (laser-facing) side.

2. Base Case Analysis

2.1 Base case results for pure SiO₂ at 4.9×10^{12} W/cm²

2.1.1 Hyades base case results

In order to establish a clear, well-characterized reference case for the purpose of comparison, we first examined a simple target with pure SiO₂ (*i.e.*, no doping) at 2 mg/cm² density. The Hyades input file is listed in Appendix B1. This case, as with all the cases presented here, used a temporal profile consisting of a 0.2-ns linear ramp-up to full laser intensity, followed by a 3.6-ns flat-top and then a 0.2-ns ramp-down to zero. The flat-top intensity for the base case was 4.9×10^{12} W/cm². We chose to use a uniform grid, with no feathering near the illumination source, for three reasons: (1) this grid allowed us to perform the most direct side-by-side comparison of Hyades and Helios, (2) results are easier to interpret in a uniform grid (where the spatial coordinate and mass coordinate are simply related), and (3) these low-density targets do not exhibit sharp gradients as with fully-dense targets, and so we do not expect feathering to be necessary. The equation of state and opacity were derived from Sesame [5] data tables. For the Hyades base case, gray (spectrally averaged) opacities were used.

Figures 1 and 2 show the time histories of electron temperature and density in each Lagrangian zone. Excluding the outermost zone (which we show later to be an artifact of the grid), a peak temperature of ~130 eV is reached at the end of the pulse. The variation in temperature through the target is about a factor of two, with the minimum (located at the back side) of ~55 eV. The temperature gradient is relatively smooth from front to back. Figure 3 shows the spatial profile of electron temperature at 2.5 ns into the pulse; about 60% of the plasma has very uniform temperature (~55 eV), whereas the outermost 40% is more strongly heated.

Figure 4 shows the integrated laser intensity through the plasma, zone by zone, for the outermost half of the target. This parameter depicts the amount of laser light which reaches any given location in the target as a function of time. Clearly, the rear side of the target is not reached by the incident laser during the 4-ns pulse.

Inverse bremsstrahlung is the dominant mechanism for laser absorption in this underdense target. The absorption follows an exponential decay:

$$dI/dx = -\alpha I$$

where the absorption coefficient α is given by:

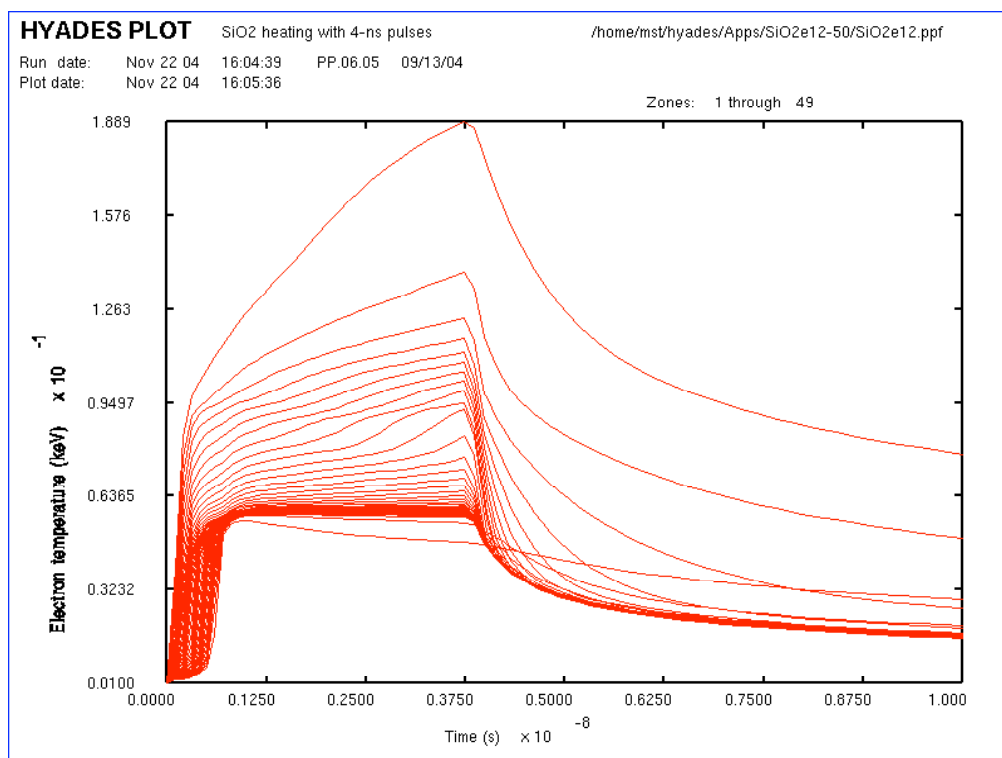


Figure 1. Electron temperature history at 50 equal-mass zones for the Hyades base case

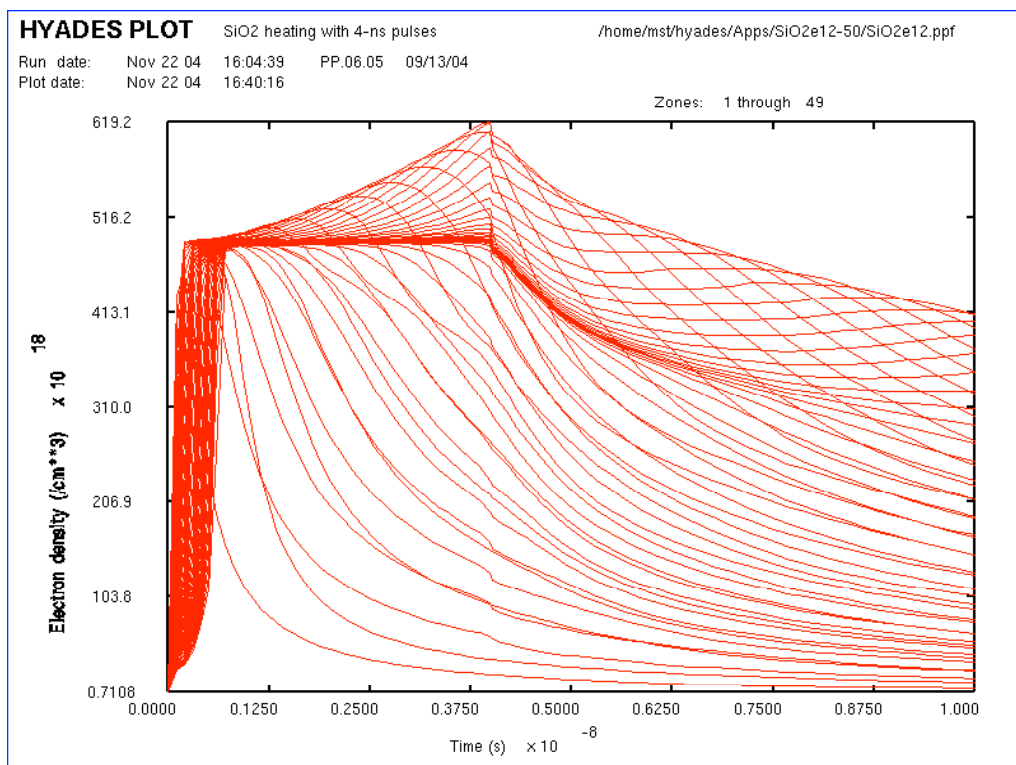


Figure 2. Electron density history at 50 equal-mass zones for the Hyades base case

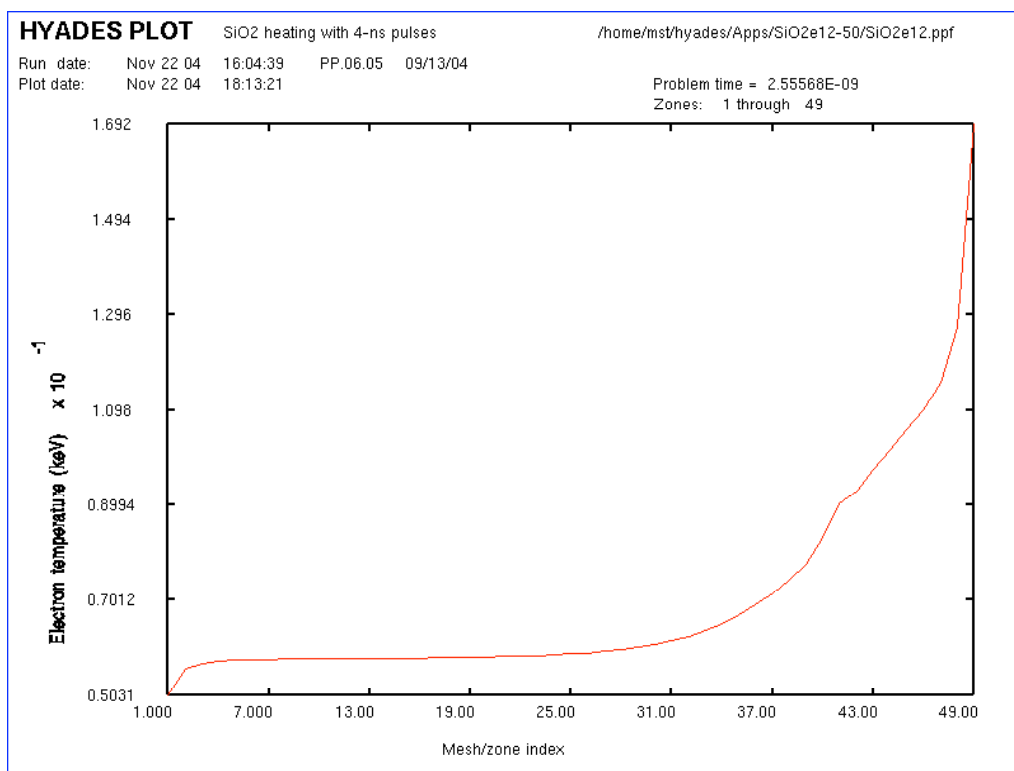


Figure 3. Electron temperature spatial profile at 2.5 ns for the Hyades base case

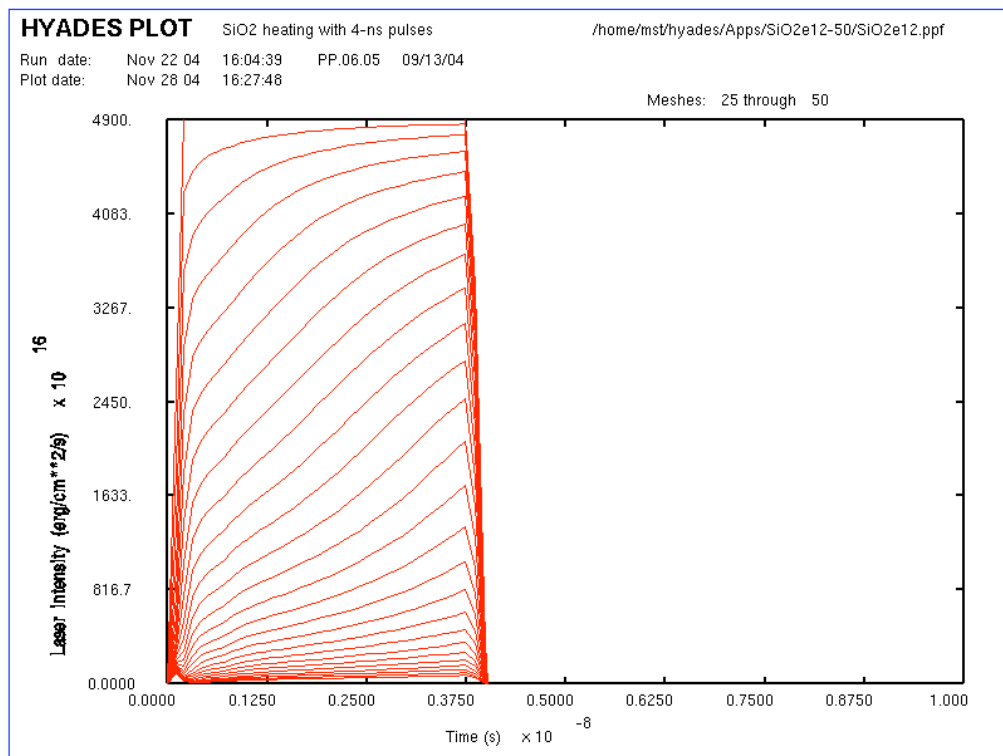


Figure 4. Time history of laser flux in the outermost half of the target for the Hyades base case

$$\alpha = 10^{-16} T_e^{-3/2} Z \ln \Lambda (n_e^2/n_{cr})$$

All units are cgs except temperature, which is measured in eV.

In a laser absorption wave, laser energy deposited at the wave front raises the electron temperature, allowing light propagation behind the front. [6] This occurs because the absorption coefficient drops as the plasma heats up. Based on Figures 1–4, the front half of the target appears to have burned through by the end of the pulse. This portion of the target maintains a temperature gradient, probably related to the exponential decay of the incident laser energy. The rear side of the target maintains a more uniform temperature as a result of radiation exchange at wavelengths where the target is optically thinner.

As seen in Figure 2, the electron density shoots up rather quickly during the ramp-up phase and remains relatively constant at $\sim 5 \times 10^{20}/\text{cm}^3$ over a portion of the laser pulse. Figures 5 and 6 help us to explain this behavior. Figure 5 shows the average charge state history in each zone. The entire target achieves a He-like state ($Z_{\text{eff}}=8$ for an average target Z of 10) very quickly, during the ramp-up phase, and then remains in that state until the laser is removed. At that point, the plasma slowly recombines. Notice that a gradual increase in charge state occurs during the laser pulse in the outermost 10 zones, which are most strongly heated (120–180 eV).

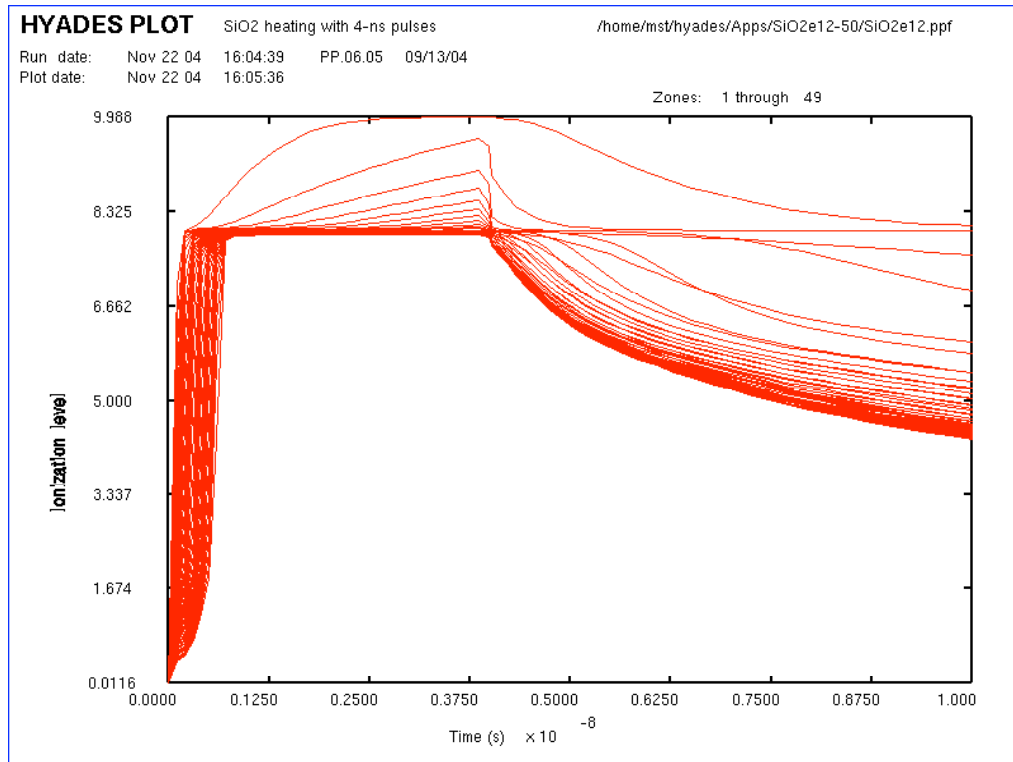


Figure 5. Charge state history at 50 equal-mass zones for the Hyades base case

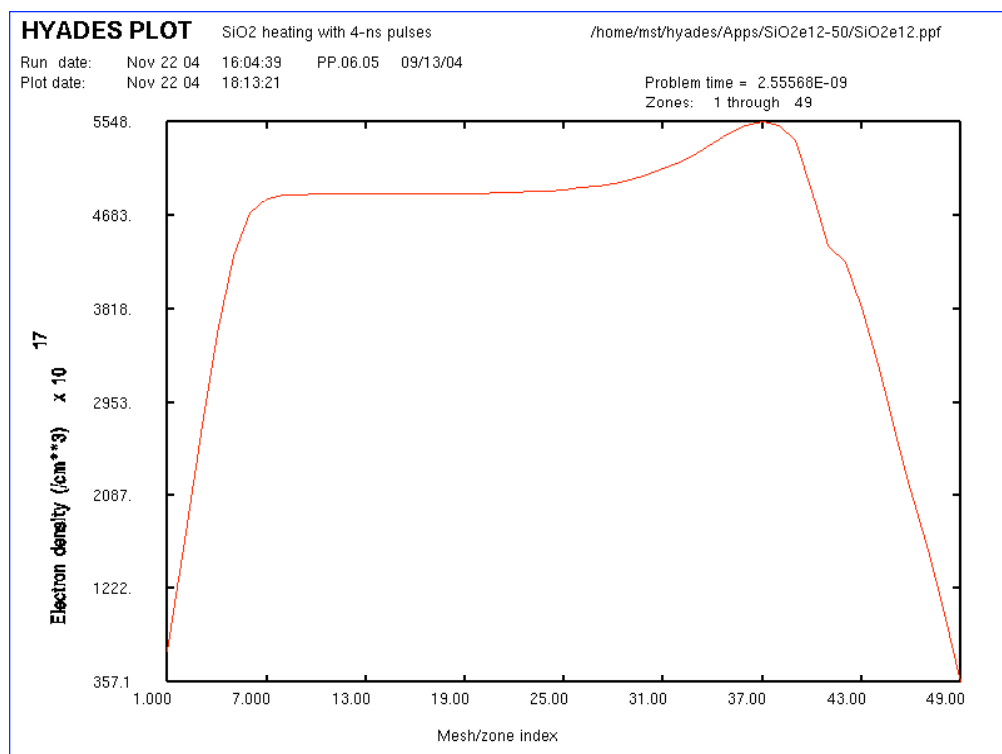


Figure 6. Electron density spatial profile at 2.5 ns for the Hyades base case

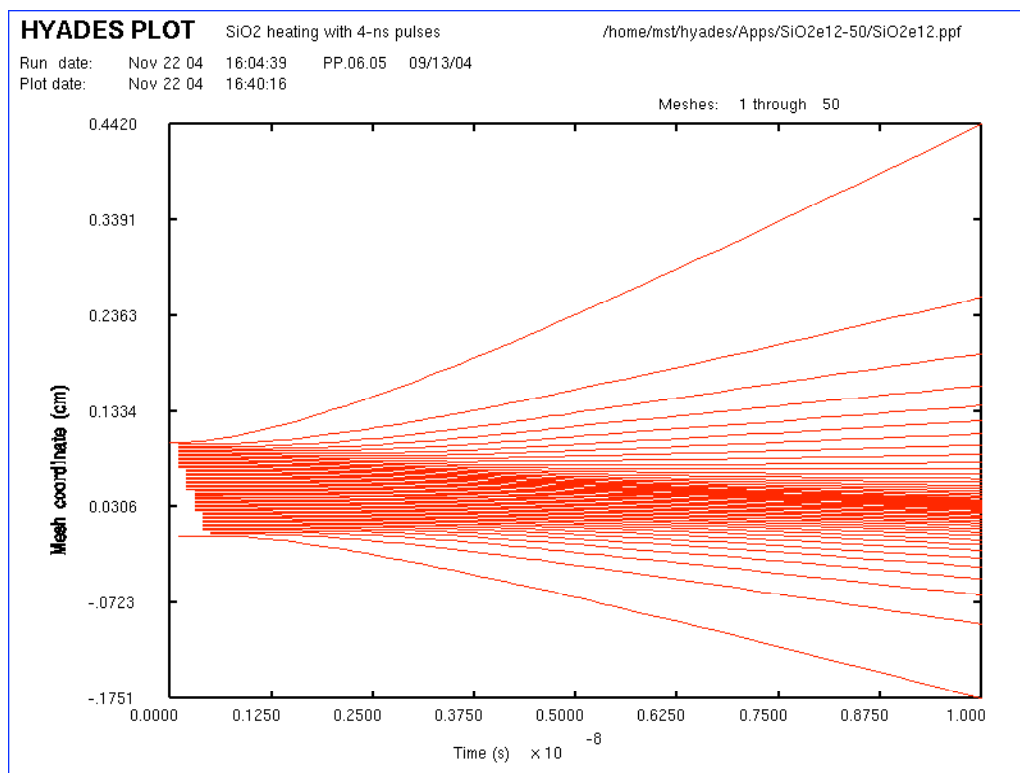


Figure 7. Time history of the radial location of the Lagrangian zones for the Hyades base case

Figure 6 helps to clarify the density history shown in Figure 2. It shows the spatial profile of electron density at 2.5 ns. The profile is relatively flat except at the outer edges. The curves in Figure 2 that drop down during the pulse are caused by hydrodynamic expansion on both sides of the target. For this value of laser intensity, the expansion velocity is relatively modest, such that the majority of the target remains intact even at the end of the 4-ns pulse. Figure 7 shows the R-t plot of the zones. It confirms that the outermost zones are expanding during the laser pulse, causing a rapid drop in density for those zones.

We examined the grid dependence of the Hyades results by running a case with 100 equally spaced nodes (instead of 50). The electron temperature and density histories are shown in Figures 8–9. The average charge state and R-t plots are nearly indistinguishable, and therefore are not shown here.

The temperature profile in Figure 8 is nearly identical to that of Figure 1, except for the outermost zone in the 50-zone case. That zone appears to be considerably hotter than the case with a finer grid. The densities in Figure 9 are also very similar to those of Figure 2. The peak density is about 10% higher in the case with a coarse grid as compared with the finer grid. For the purposes of the parametric study shown in the following sections, we decided to use 50 zones because the results are easier to interpret without a separate graphical postprocessor (*i.e.*, using the existing HYADPLOT routine).

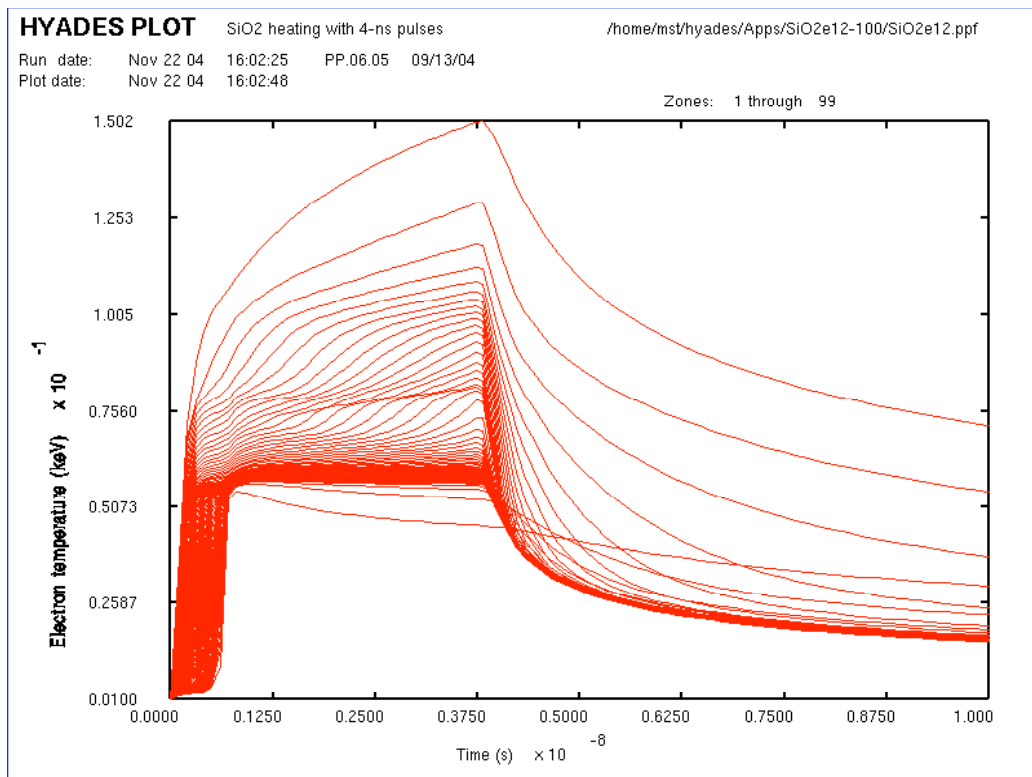


Figure 8. Electron temperature history at 100 equal-mass zones for the Hyades base case

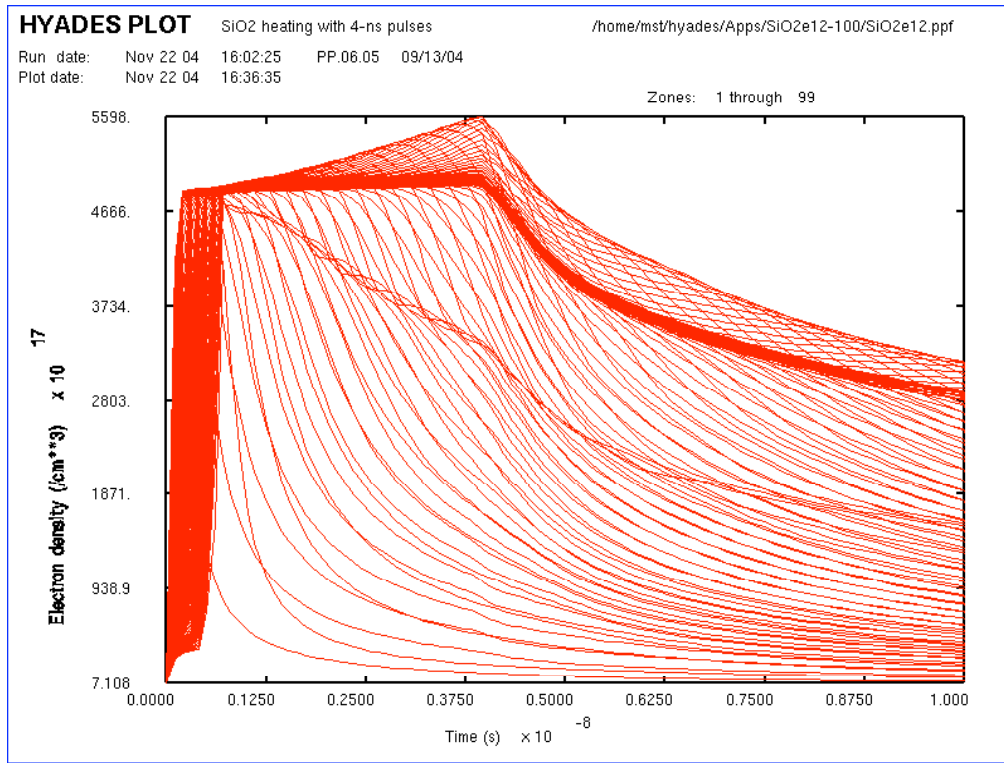


Figure 9. Electron density history at 100 equal-mass zones for the Hyades base case

2.1.2 Helios base case results

Helios provides a relatively independent check on the validity of the results presented in the preceding section. It includes laser absorption and hydrodynamic models similar to Hyades, but also provides spectrally resolved opacities as a built-in feature. We used the same input parameters for the Helios base case and a grid with 100 equally spaced nodes. Both the equation of state and spectrally resolved opacities were obtained from the PROPACEOS database. The default number of frequency groups was 50.

Figure 10 shows the electron temperature history corresponding to that of Figure 1. The peak temperature is ~ 215 eV as compared with 130 eV predicted by Hyades. Note that the temperature rises more slowly in the rear part of the target as compared with Hyades. Helios predicts continued heating of the rear side of the target in the late part of the laser pulse, whereas Hyades predicts a relatively flatter time history in the rear of the target. The temperature of the rear side increases nearly monotonically in time until it reaches almost 100 eV at the end of the pulse, whereas Hyades predicts a nearly constant 55 eV during the pulse. Most likely these differences arise due to the different opacity models used in Helios and Hyades.

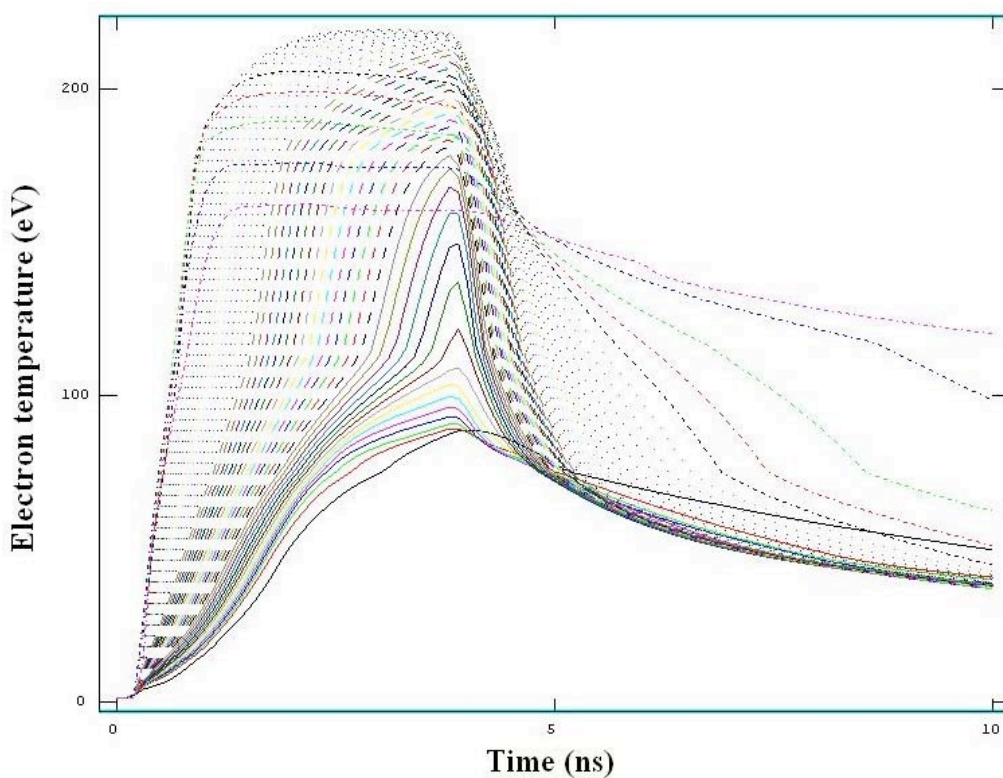


Figure 10. Electron temperature history for the Helios base case

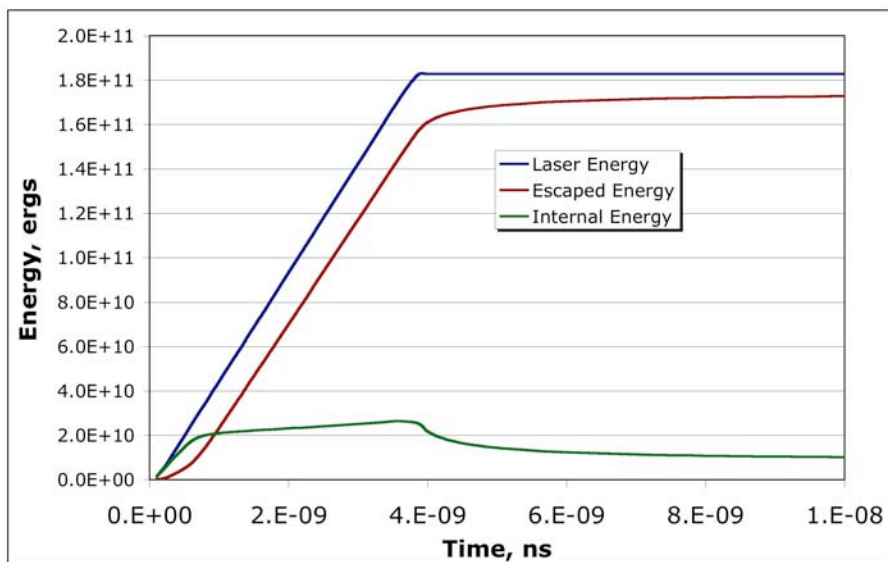


Figure 11. Internal and radiated energy for the Hyades base case

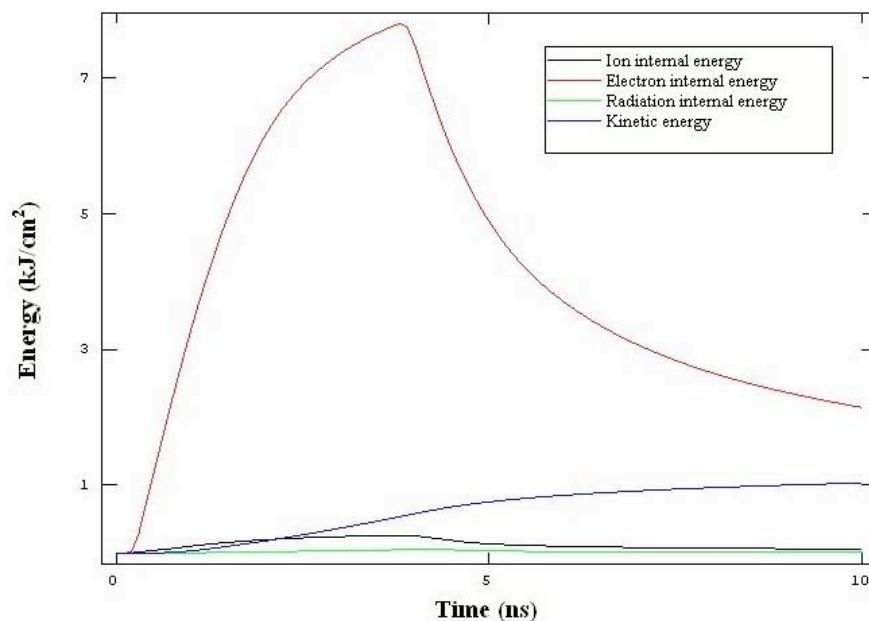


Figure 12. Internal energy for the Helios base case

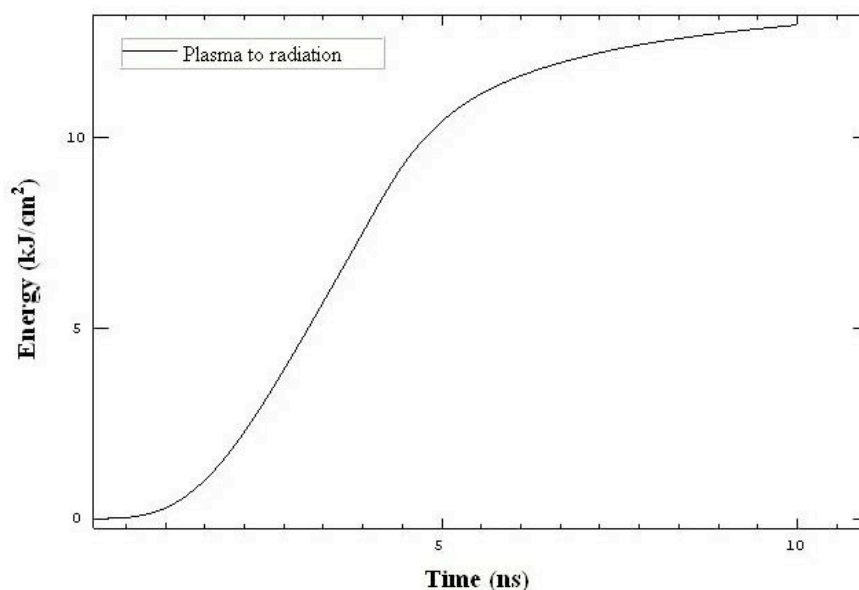


Figure 13. Radiated energy for the Helios base case

In order to elucidate the substantial difference in electron temperature between these two codes, we examined the energy balance vs. time for the modeling base case. Figures 11–13 show the evolution of internal energy and radiated energy for Hyades and Helios. The total energy for each is approximately equal to the incident laser energy of 18.6 kJ. Almost 90% of the incident laser energy promptly escapes by radiation in Hyades. After the initial heatup, the internal energy is modest, at about 10% of the total. Conversely, Helios predicts nearly *half* of the total energy during the laser pulse is retained in the electrons, with only half being promptly emitted.

As the plasma cools following the pulse, emission continues until a final state similar to Hyades is reached, with about 1 kJ (~5%) of energy in particle kinetic energy and the remainder radiated away.

Figure 14 shows the electron density history predicted by Helios, as compared with that of Figure 2. In this case, the agreement is remarkably good. The peak value of density ($5 \times 10^{20}/\text{cm}^3$), as well as the temporal and spatial profiles, are very well matched. This is not entirely surprising, as the density is determined primarily by the charge state, which is relatively insensitive to temperature in this regime with a closed K-shell.

Helios consistently exhibits a rise in electron density within the target immediately after the laser source is removed. This appears to be caused by a recoil effect from the sudden change in pressure balance. Immediately after the laser is removed, hydrodynamic expansion near the two surfaces continues to push the target inward. This causes a mass density increase near the center, with a corresponding increase in electron density. This phenomenon is explored in more detail in Section 3.1 where the presence of dopant appears to enhance the effect.

Figures 15 and 16 are provided for comparison with the spatial profiles shown in Figures 3 and 5. Unlike Hyades, Helios predicts a drop in temperature at the front side closest to the plasma at 2.5 ns into the pulse. This cooling is plausible as a result of adiabatic expansion. As described above, the internal structure of the temperature profile is again evident: Hyades predicts a rather flat profile whereas Helios predicts a hotter (~200 eV) front side and colder (~100 eV) rear side.

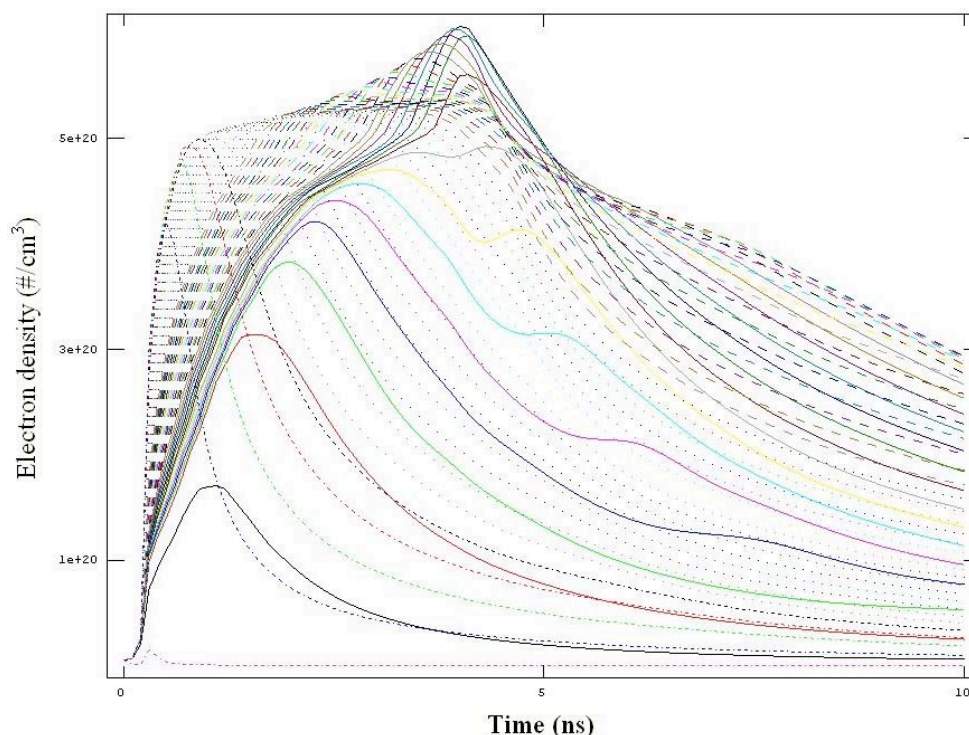


Figure 14. Electron density history for the Helios base case

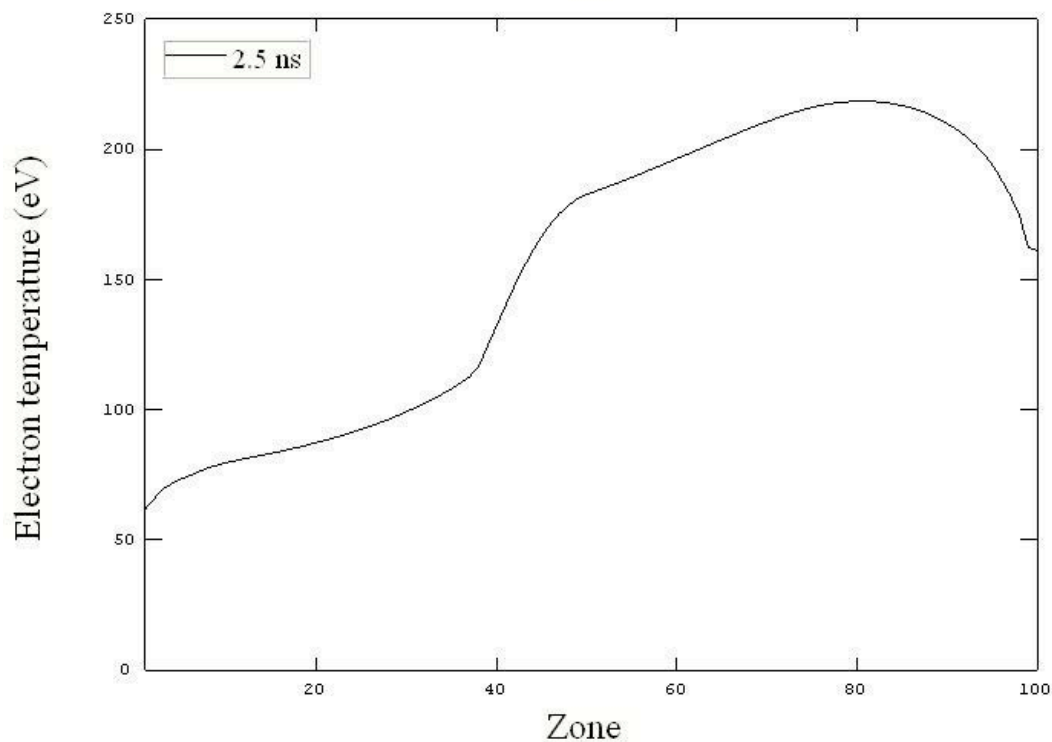


Figure 15. Electron temperature spatial profile at 2.5 ns for the Helios base case

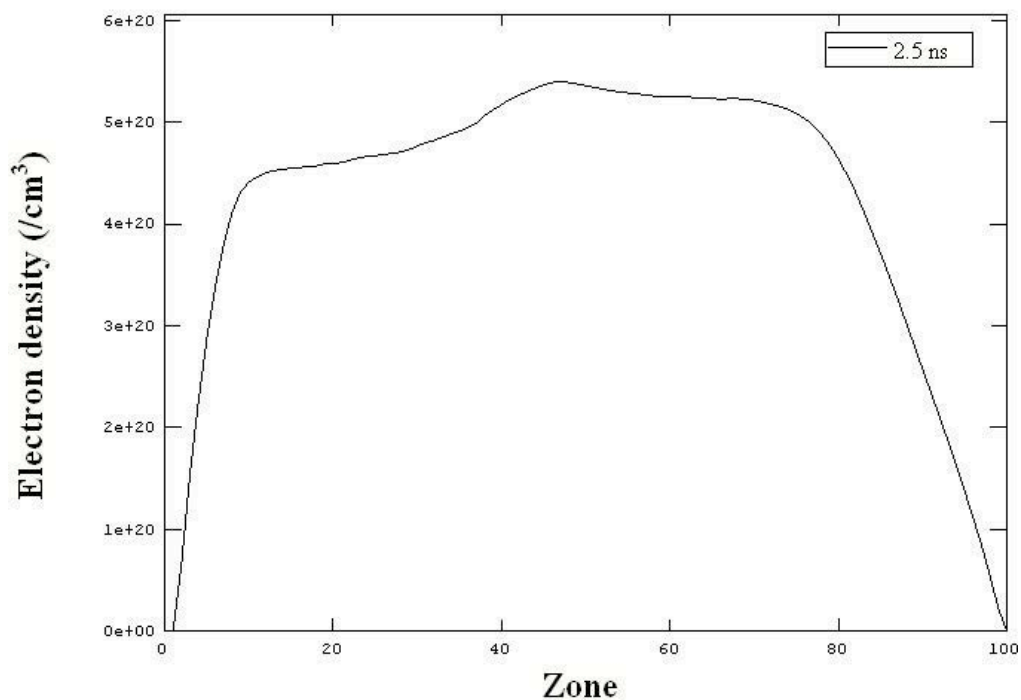


Figure 16. Electron density spatial profile at 2.5 ns for the Helios base case

2.2 Effect of opacity models on the base case results

Since radiation transport is one of the dominant mechanisms by which targets heat, cool and transport energy, treating the opacity, or absorption and re-radiation of photons is fundamental to determine the plasma evolution. In an effort to understand the differences between radiation transport driven by gray opacities *vs.* spectrally-resolved opacities, we attempted to swap input files between Hyades and Helios, and interpret the results. Not only would this allow us to assess the importance of full spectral resolution in modeling, but would provide a side-by-side comparison between two independent radiation hydrodynamics codes.

The following effects were explored:

1. We compared Hyades results using Rosseland average *vs.* Planck average opacities
2. We compared the Helios and Hyades models using identical Sesame data. This allows us to determine the extent to which differences are caused by the modeling approaches as opposed to the data used.
3. We attempted to model spectrally resolved results in Hyades using two different techniques: (a) group radiation transport with the built-in opacity model, and (b) imported data obtained from the Propaceos library. Neither of these approaches was successful.
4. We compared Helios results using spectrally resolved Propaceos data and single-group averaged data.

2.2.1 Opacity models and averaging techniques

There are two common methods for spectral averaging of opacities: Planck mean and Rosseland mean. The Planck mean opacity (a_p) is simply an average over wavelengths, which is weighted by a blackbody spectrum ($e_{\lambda b}$) [7]:

$$a_p(T, n) = \frac{\int_0^{\infty} a_{\lambda}(\lambda, T, n) e_{\lambda b}(\lambda, T) d\lambda}{\sigma T^4}$$

where the spectrum is given by:

$$e_{\lambda b} = \frac{2\pi C_1}{\lambda^5 (e^{C_2/\lambda T} - 1)}$$

It is most useful for estimating emission, and in some optically thin cases. The Rosseland mean opacity (a_R) is a flux-weighted average of the diffusivity (inverse of absorption):

$$\frac{1}{a_R(T, n)} = \frac{\int_0^{\infty} \frac{1}{a_{\lambda}(\lambda, T, n)} \frac{de_{\lambda b}}{dT}(\lambda, T) d\lambda}{\int_0^{\infty} \frac{de_{\lambda b}}{dT}(\lambda, T) d\lambda}$$

where the derivative of the Planck spectrum can be written as:

$$\frac{de_{\lambda b}}{dT} = \frac{2\pi C_1 C_2}{\lambda^6 T^2} \frac{e^{C_2/\lambda T}}{(e^{C_2/\lambda T} - 1)^2}$$

Rosseland mean opacity is more appropriate in cases which are dominated by radiation diffusion (which is the form of radiation transport assumed in Hyades as the default). Figure 17 shows the two averaged opacities as a function of temperature for a density of 2 mg/cm³ in SiO₂ using Sesame data. The Planck mean is higher at lower temperatures, but drops off quickly above about 1 keV. The Rosseland mean opacity remains finite at very high temperatures.

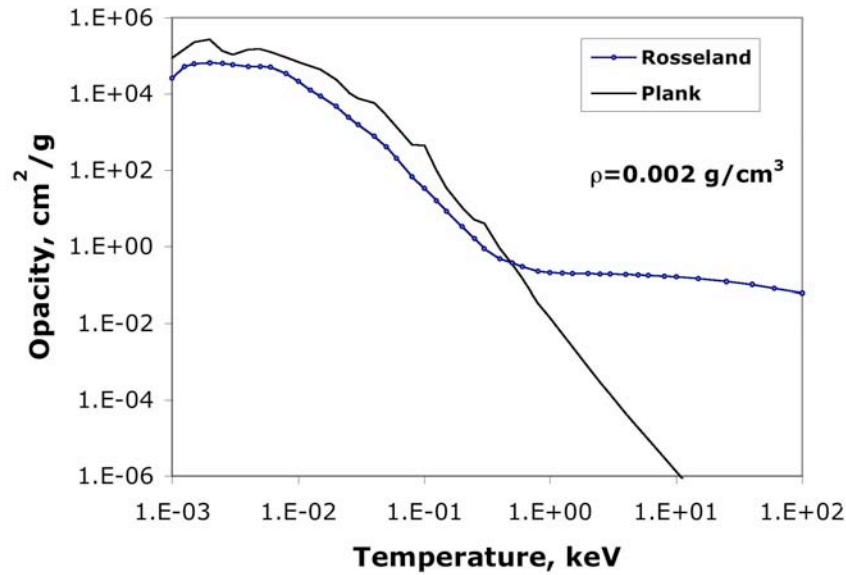


Figure 17. Comparison of Rosseland and Planck Sesame opacity for SiO₂

Helios allows the user to implement spectral averaging in the code by choosing a single frequency group in the input parameters. The type of averaging is determined automatically by the code; the user has no control over this. In order to examine the single-group Planck and Rosseland averages, we wrote a short Fortran routine to perform the averages from the full Propaceos data files. Appendix B.2 contains the source code listing. Figures 18 and 19 compare the Sesame single-group opacities with the averaged opacities we calculated from Propaceos. The Propaceos data is consistently higher than Sesame in the range of 100–1000 eV, which is an important range of energies for the present work. This could easily explain the substantial differences observed in the electron temperature and energy balance.

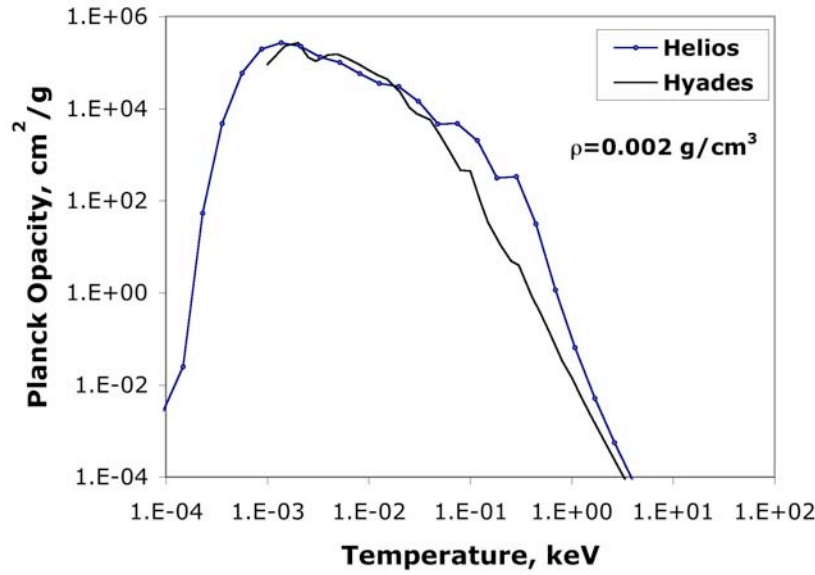


Figure 18. Comparison of single-group Sesame and Propaceos data with Planck averaging

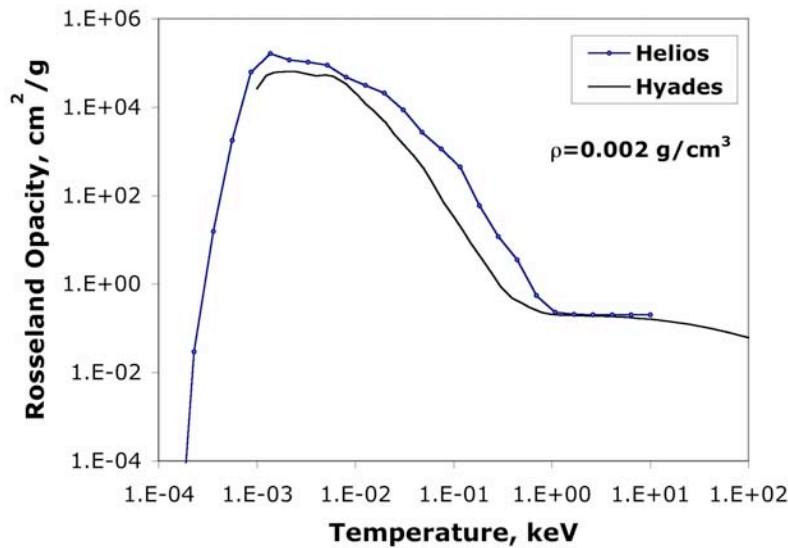


Figure 19. Comparison of single-group Sesame and Propaceos data with Rosseland averaging

2.2.2 Comparison of Hyades results with Planck vs. Rosseland averaging

Rosseland mean averaged data are the default used by Hyades. However, the optical thickness of some of our plasmas is rather small, and so Planck averaged data may be more appropriate. We ran the base case with Planck averaged Sesame data for comparison. Figure 20 shows the electron temperature profile through the target at 2.5 ns into the pulse. Comparing with Figure 3, the results are very similar. Differences are at the level of 10%.

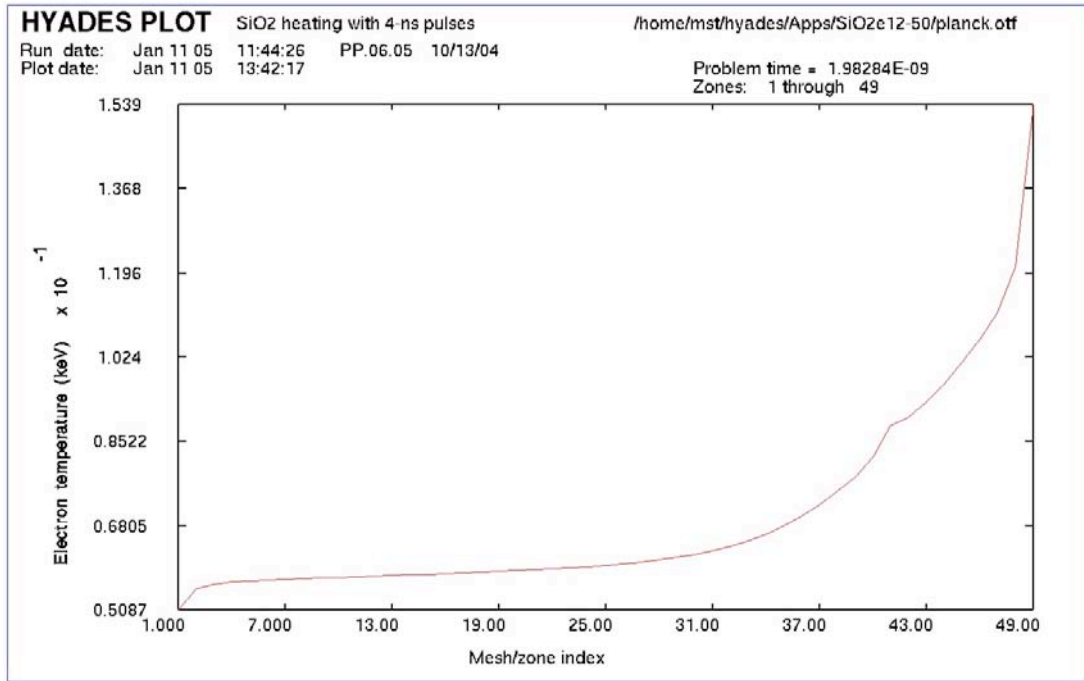


Figure 20. Hyades electron temperature at 2.5 ns using single-group Planck averaging

2.2.3 Comparison of Hyades and Helios models using identical (gray) Sesame data

Importing gray opacities from the Hyades Sesame library into Helios allows us to directly compare the results from two laser-plasma simulation codes using identical input data sets (Sesame EOS and opacity). It also provides some insight into whether or not single-group opacity tables are sufficient in capturing the radiation signature of under-dense plasmas.

We wrote a simple C++ program that extracted single-group opacity data from the Hyades Sesame library and reformatted it for Helios. Below are the results from Helios using Sesame EOS and opacity data. For comparison, results from the analogous Hyades run (identical input data) are shown in Figures 1–4.

As shown in Figures 21 and 22, the densities for these runs are approximately the same. A more surprising result is that the peak electron temperature for the Helios run is more than a factor of 3 higher than that of the Hyades run (see Figures 23 and 24). Since the input data sets are identical, this difference can only be attributed to the internal algorithms of the codes; *i.e.*, laser energy absorption processes, ionization models, energy coupling between radiation field and electrons, *etc.* We are continuing to explore this surprising result.

Comparing Figures 21–24 with Figures 1–3 and 6, we can establish the difference in target behavior with the same code but different opacity datasets. Using Sesame data, temperatures predicted by Helios are over a factor of two higher. Electron densities are more similar, with changes of the order of 10%. As we observed earlier, the electron density is relatively insensitive to temperature when the atoms are stripped down to a closed shell.

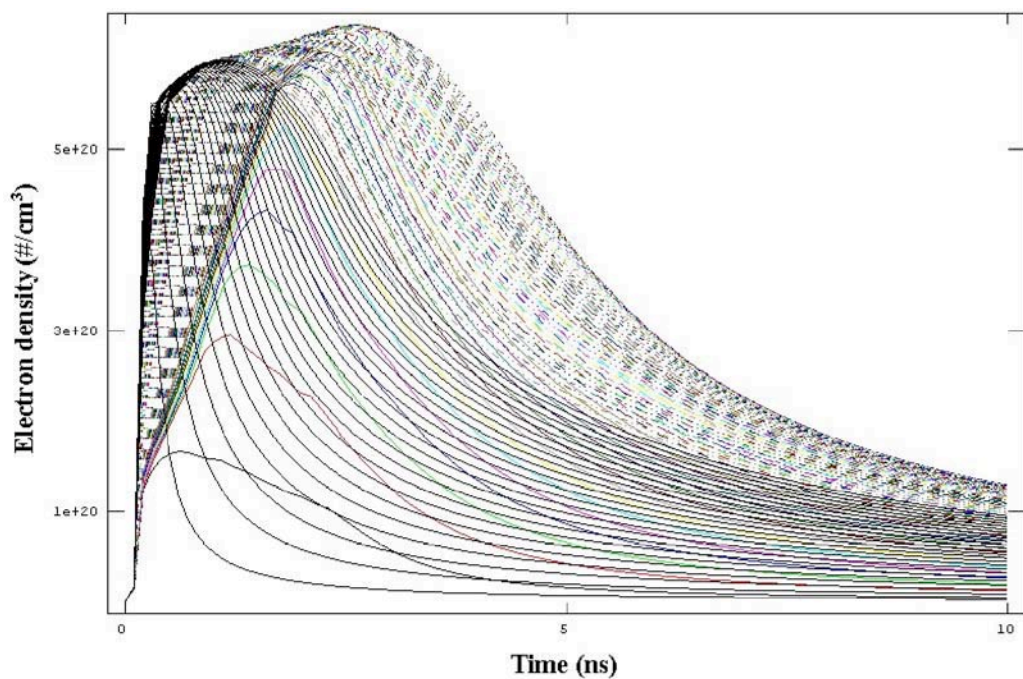


Figure 21. Electron density history for Helios using Sesame gray opacity and EOS

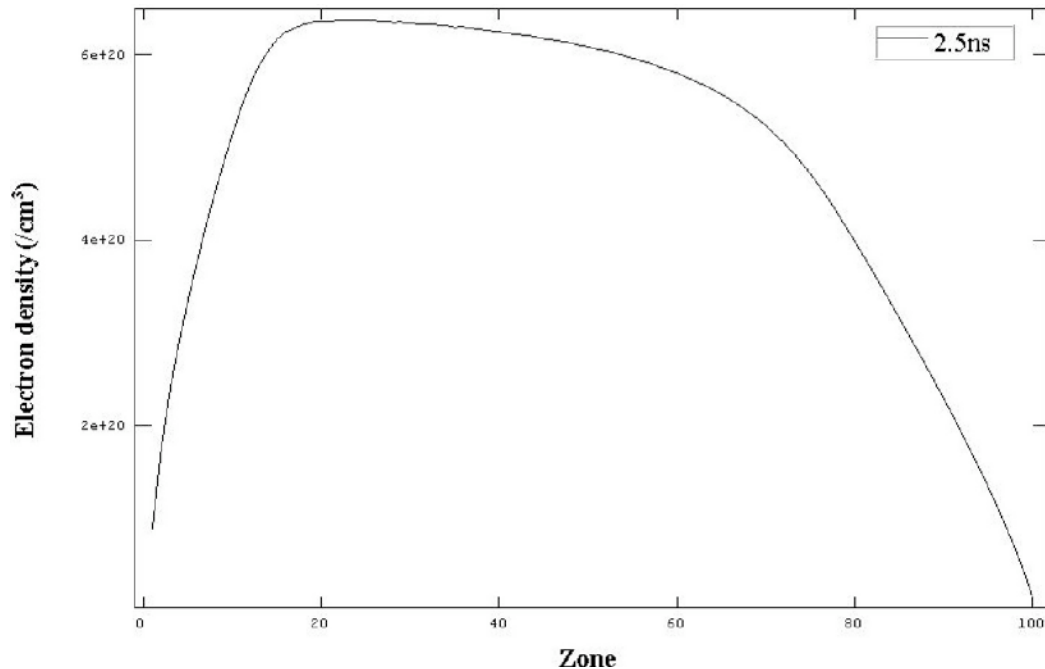


Figure 22. Electron density spatial profile at 2.5 ns for Helios using Sesame gray opacity and EOS

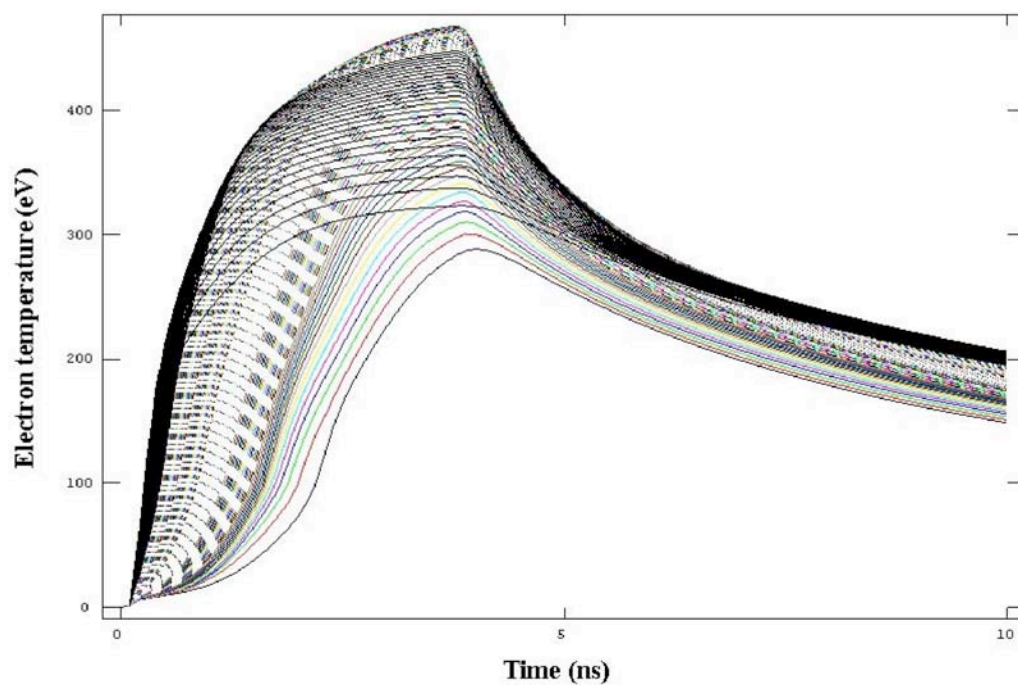


Figure 23. Electron temperature history for Helios using Sesame gray opacity and EOS

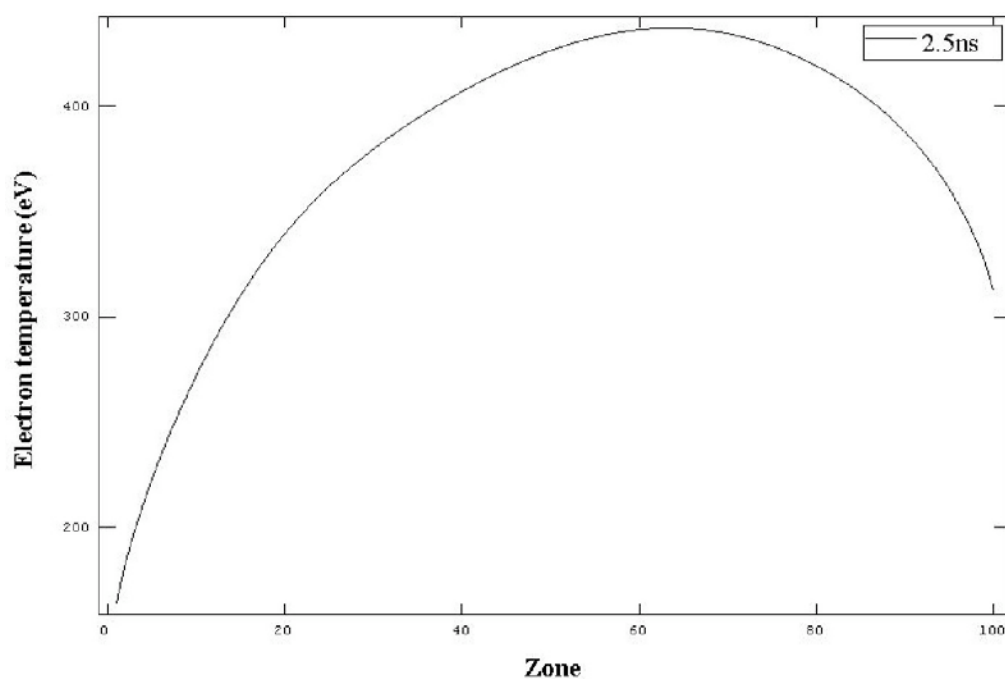


Figure 24. Electron temperature spatial profile at 2.5 ns for Helios
using Sesame gray opacity and EOS

2.2.4 Attempts at spectrally resolved results with Hyades

A typical Hyades run uses spectrally averaged EOS and opacity data extracted from the Sesame data library. User options are offered for multi-group radiation transport and spectrally resolved opacities. Attempts were made to introduce spectral resolution into Hyades *via* these two techniques. First, group radiation transport was attempted using the built-in multi-group transport model, and second, attempts were made to import spectrally resolved data from the Propaceos library.

When a GROUP statement is included in the HYADES input file, opacity data is generated using an internal algorithm which includes some atomic shell effects and crude x-ray line effects. We specified 100 spectral groups with a maximum energy of 3 keV, using the following input statement:

```
group 1 100 9.8e-5 3.0
```

All other input parameters remained identical to the base case. Figure 25 shows the electron temperature history resulting from this run. The maximum temperature rose to over 500 eV in this case. The most likely cause of such an unexpectedly high electron temperature is the presence of lower radiation emission. Radiation emission is the primary energy loss term which balances energy absorption by inverse bremsstrahlung; with reduced emissivity, the temperature will rise until the radiation emission equals the laser input power.

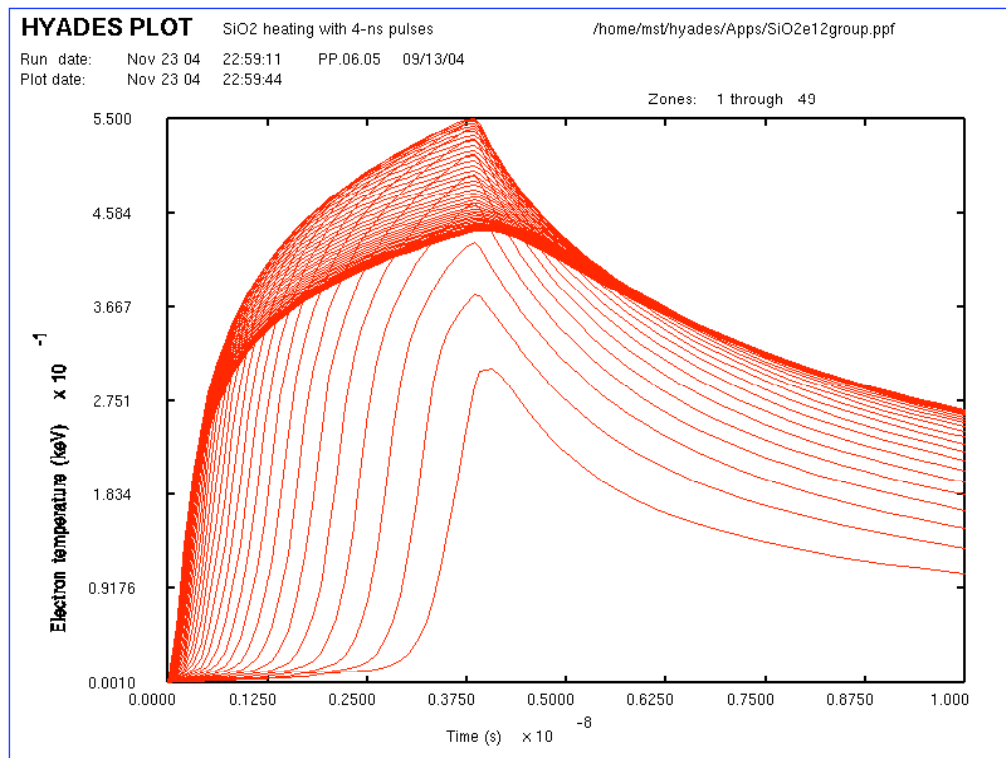


Figure 25. Electron temperature history using the Hyades group radiation transport module

The peak temperature achieved with Hyades using group radiation transport is similar to the temperature found with Helios using gray opacities. Most likely this is a coincidence coming from two separate effects.

Figure 26 shows the corresponding charge state of the plasma. The higher temperature causes the SiO₂ to rapidly strip to a fully ionized state. There is little delay at the He-like charge state of 8. The electron density in this case is a strongly varying function of both time and space.

In a second attempt to implement a spectrally resolved treatment of radiation, we tried to import data from PROPACEOS into Hyades. Hyades explicitly supports the option of importing an external spectrally resolved file in ASCII format. For simplicity, a routine was created with IDL (Interactive Data Language) to perform the conversion of the Propaceos file into a Hyades-compatible format. The content of the converted file was re-read and plotted with IDL, and was determined to match Helios data-viewer plots of the original Propaceos file.

A record was added in the HYADES input file to call the external opacity file directly by specifying its path and filename in the “EOS” record. We were not able to obtain results using this technique. Although the code supports externally generated multi-group opacity tables in principle, the import utility failed in mapping the data into a run. We are attempting to resolve this problem with the author of the code. In addition, the option of mapping the ASCII data into the binary opacity library is being explored.

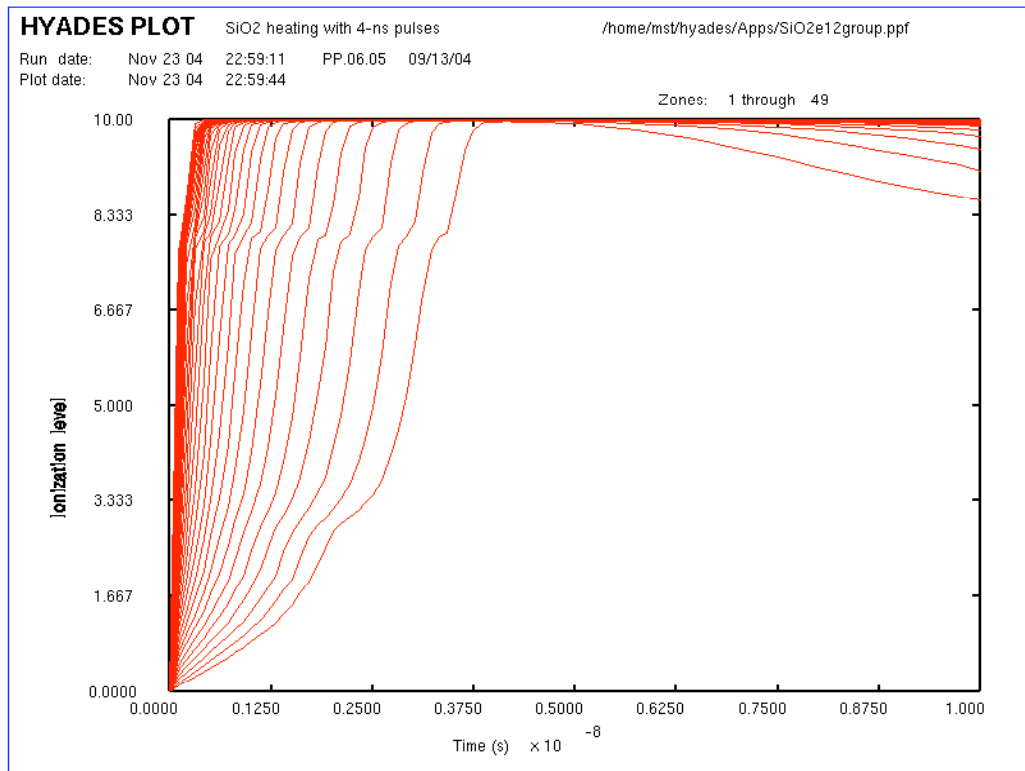


Figure 26. Charge state history using the Hyades group radiation transport module

2.2.5 Comparison of gray vs. spectrally-resolved opacities in Helios

The standard model in Helios uses spectrally resolved data from the PROPACEOS code. In Section 2.2.3, we showed results from Helios using Sesame gray opacities and compared those results with the spectrally resolved run. This helped to elucidate differences between Hyades and Helios, but is not a good test of the effect of spectral detail. Sesame and PROPACEOS data sets are obtained from different sources, and are therefore inherently different.

In this section we compare Helios results using three different levels of spectral detail. In Section 2.1.2 we already displayed results from the base case, in which 50 frequency groups were used. Here we add a case with 500 frequency groups and a case with one frequency group. The latter case is equivalent to using a Rosseland mean (gray) opacity.

The electron temperature history for the single-group case is shown in Figure 27. The temperature is about 5% lower than the base case, but otherwise very similar. Electron temperature is the most important parameter, and the one we have observed to depend the most on the data and models. Therefore, we conclude that the effect of spectral averaging is very minor. Inspection of the other parameters showed few discernable differences.

The electron temperature profile for the 500-group case at 2.5 ns is shown in Figure 28 together with the same profile for the single-group case. Except for the presence of a bump in temperature near the target center, the results are quite similar. The spectrally resolved case exhibits about 5% higher temperature in general.

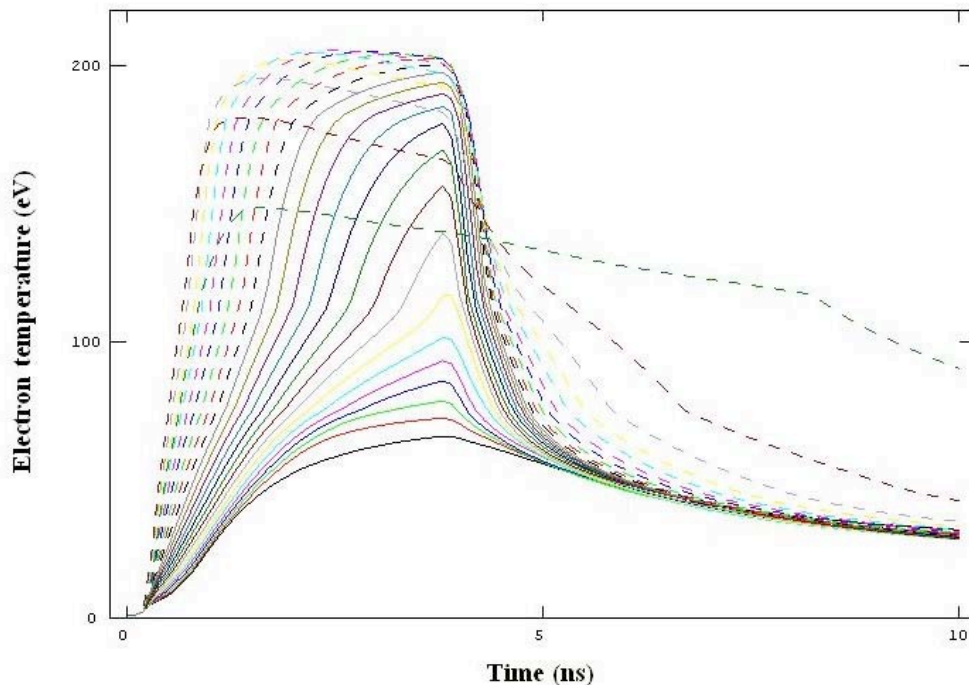


Figure 27. Electron temperature history from Helios using a single radiation group

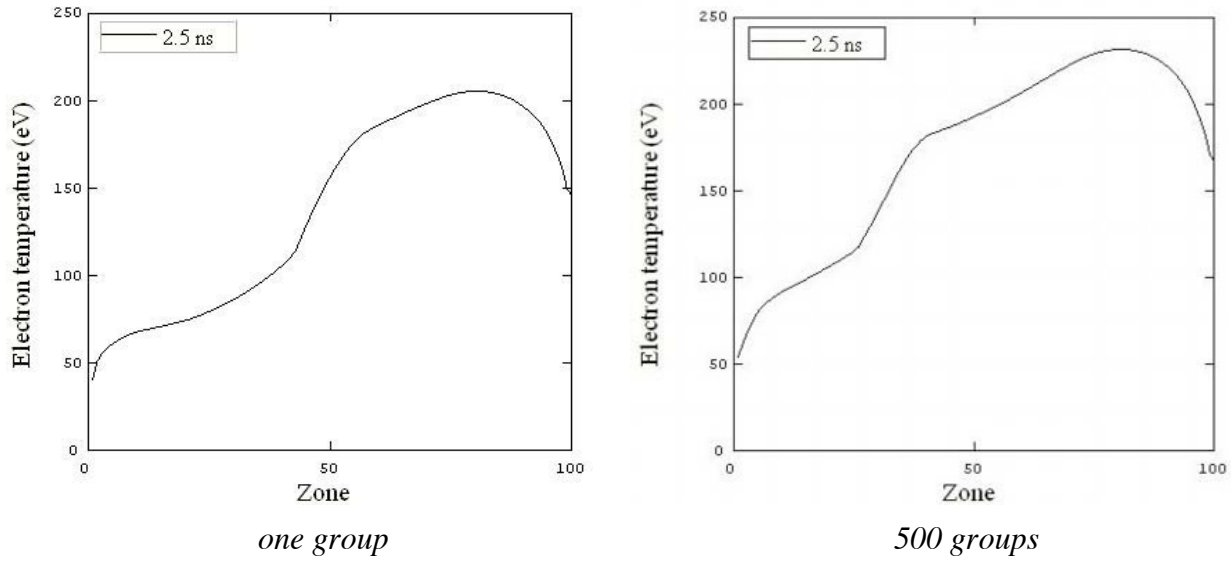


Figure 28. Comparison of electron temperature profiles using one or 500 radiation groups

3. Variation of parameters

3.1 Addition of dopant

3.1.1 Gray opacity results with Hyades

The experimental conditions of interest include doping of either 2% or 6% Ti by weight in a SiO₂ carrier. As discussed in Section 2.2.4, we were not able to input spectrally resolved opacities in Hyades, and results using the built-in multi-group transport algorithm were questionable. Therefore, Hyades modeling of the effect of a dopant was restricted to spectrally averaged cases. In order to model a mixture of Ti and SiO₂ in Hyades, we needed to generate new EOS and opacity data tables, as they are not included with the Hyades distribution. We used an arithmetic, density-weighted average to generate new EOS and gray opacity tables. Appendix B.3 contains a listing of the Fortran code we used to perform this averaging.

Figures 29–30 show the Rosseland mean opacity (the default opacity model used in Hyades) and internal energy as a function of temperature at a density of 0.002 g/cm³. Although the opacity of Ti is somewhat different than SiO₂ at lower temperatures, the averaging leads to nearly indistinguishable behavior for SiO₂-6% Ti as compared with pure SiO₂. The pressure and energy are even less affected. Based on the similarity of the data, we would not expect different radiation hydrodynamic behavior using gray opacities in Hyades.

Nevertheless, we ran a case with 6% Ti in order to demonstrate the differences quantitatively. Indeed, there is little difference. Figures 31 and 32, which show n_e and T_e at 2.5 ns, are representative of the differences. The use of gray opacities apparently leads to changes in plasma conditions roughly in line with the fraction of dopant – only a few percent.

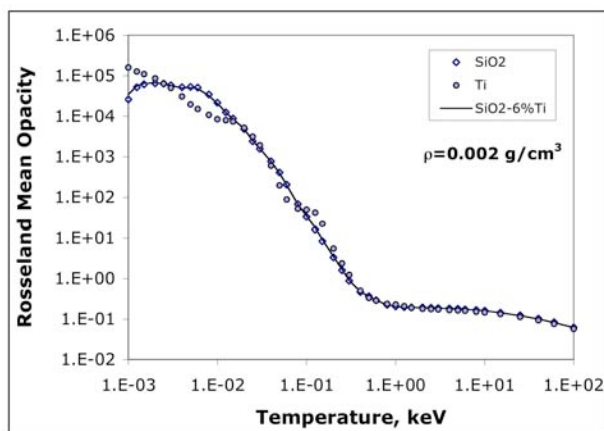


Figure 29. Rosseland mean opacity for SiO₂,
Ti and a mixture of SiO₂-6%Ti

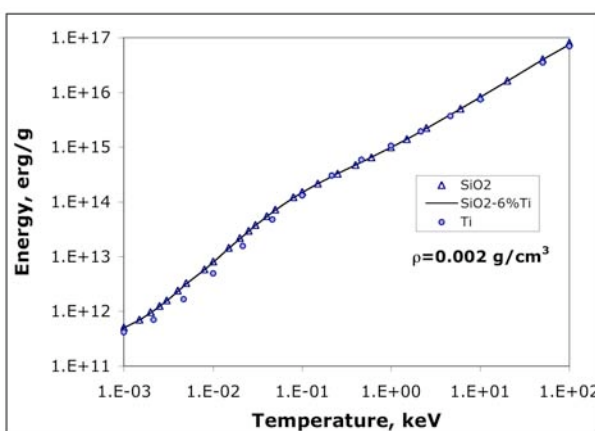


Figure 30. Internal energy EOS for SiO₂,
Ti and a mixture of SiO₂-6%Ti

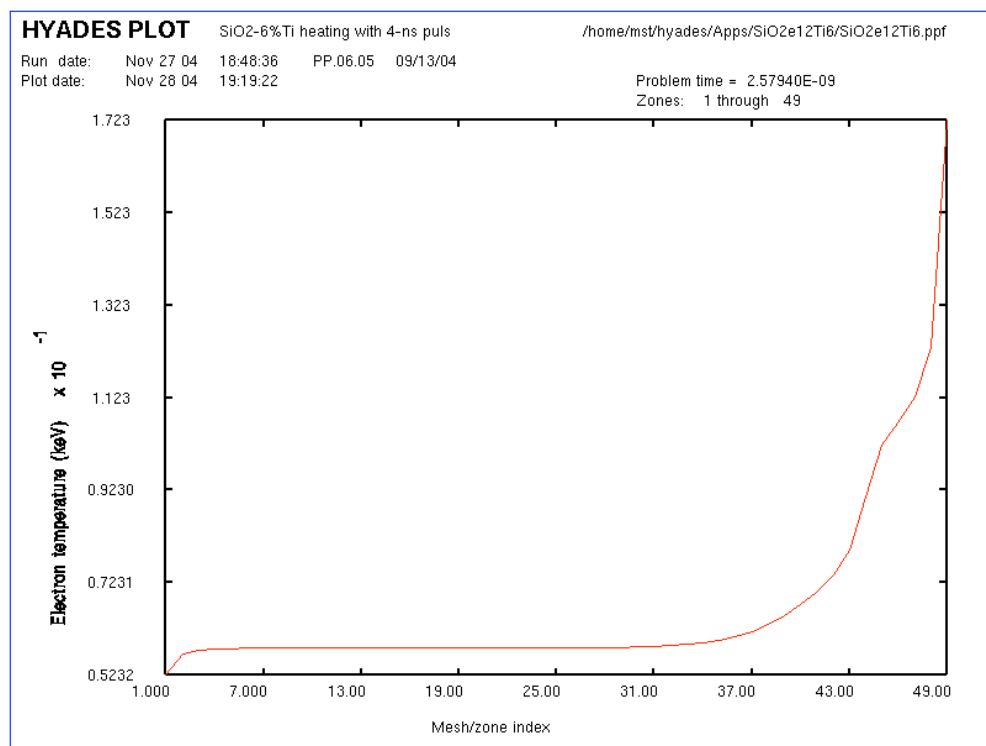


Figure 31. Electron temperature profile at 2.5 ns for SiO₂-6%Ti using gray opacities in Hyades

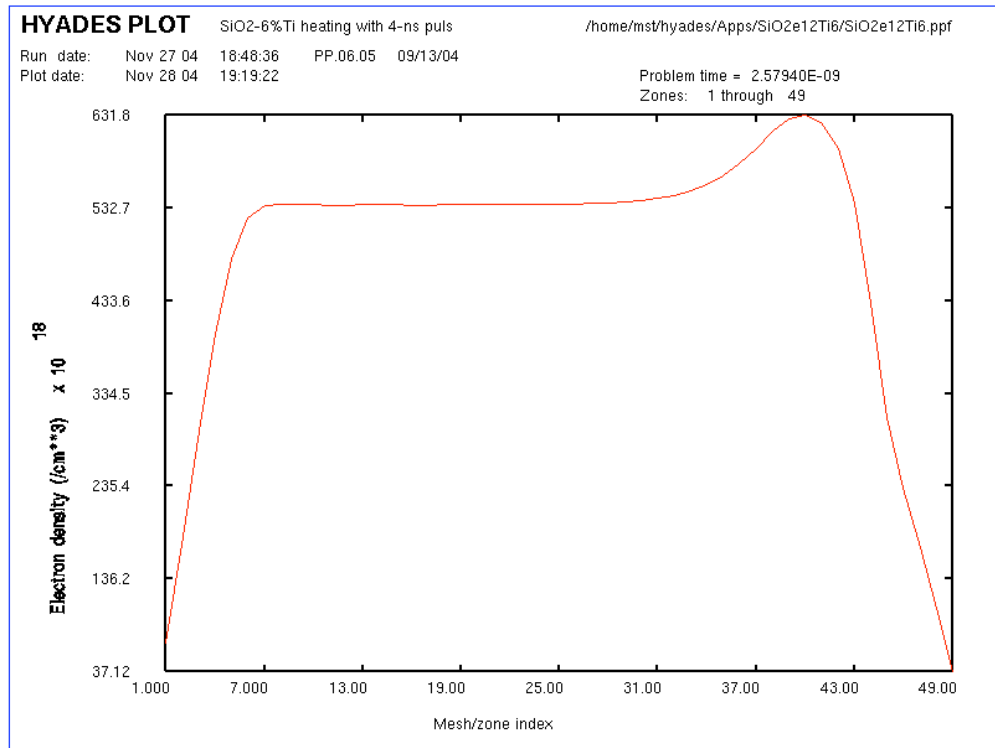


Figure 32. Electron density profile at 2.5 ns for SiO₂-6%Ti using gray opacities in Hyades

3.1.2 Spectrally resolved results with Helios

Helios includes spectrally resolved opacities from the PROPACEOS code. We obtained EOS and opacity data for mixtures of 2 w/% and 6 w/% Ti from Prism Computational Sciences and used these to compare with the base case.

Comparing Figure 33-34 with Figures 10 and 14, we can see a general decrease of electron temperature of about 25% for the case with 6% Ti doping. The case with 2% doping, shown in Figure 35, exhibited about 10% reduction in temperature. The temperature drop is most noticeable in the central region of the target. At present we do not have an explanation for this phenomenon.

The density profile, shown in Figure 36, exhibits some minor changes as compared with the base case. The magnitude remains in the range of $4\text{--}5 \times 10^{20}/\text{cm}^3$, with clear evidence of hydro expansion at 2.5 ns into the pulse. The peak occurs nearer the laser in the case of doping, which tends to indicate a change in the pressure balance.

Overall, the hydrodynamic behavior is changed only modestly by the inclusion of Ti doping up to 6%. The magnitude of temperature drops slightly, and the profile becomes more nonuniform. Changes in density indicate internal hydrodynamic motion has changed; these changes are of the order of 10-20%.

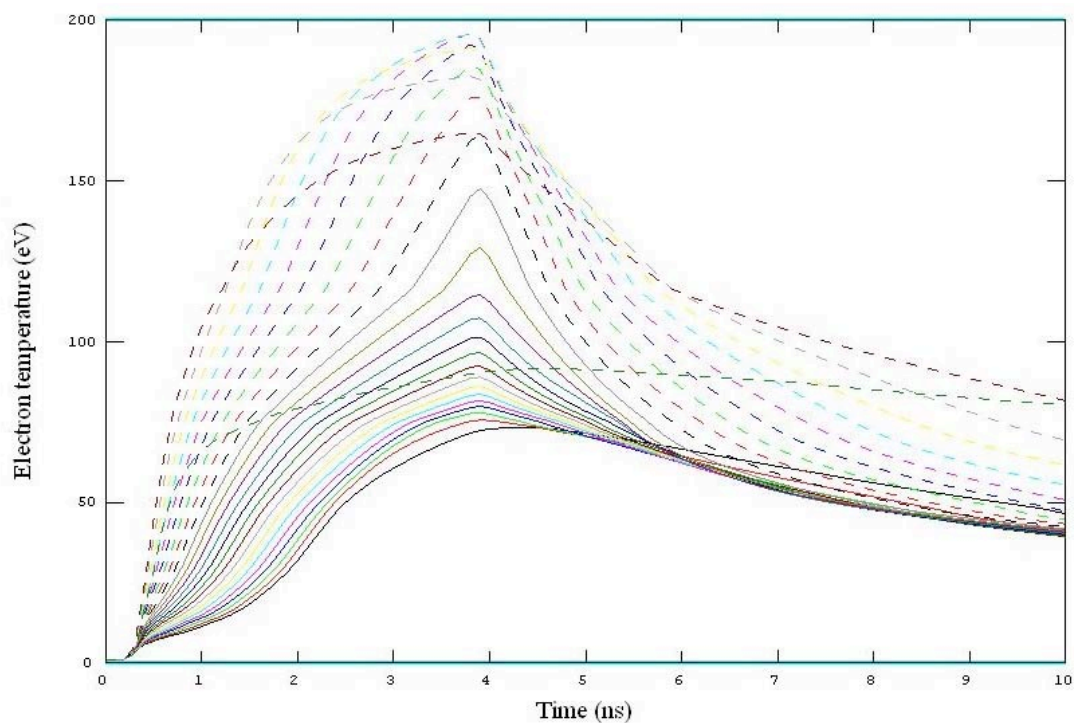


Figure 33. Electron temperature history for SiO₂-6% Ti using Helios

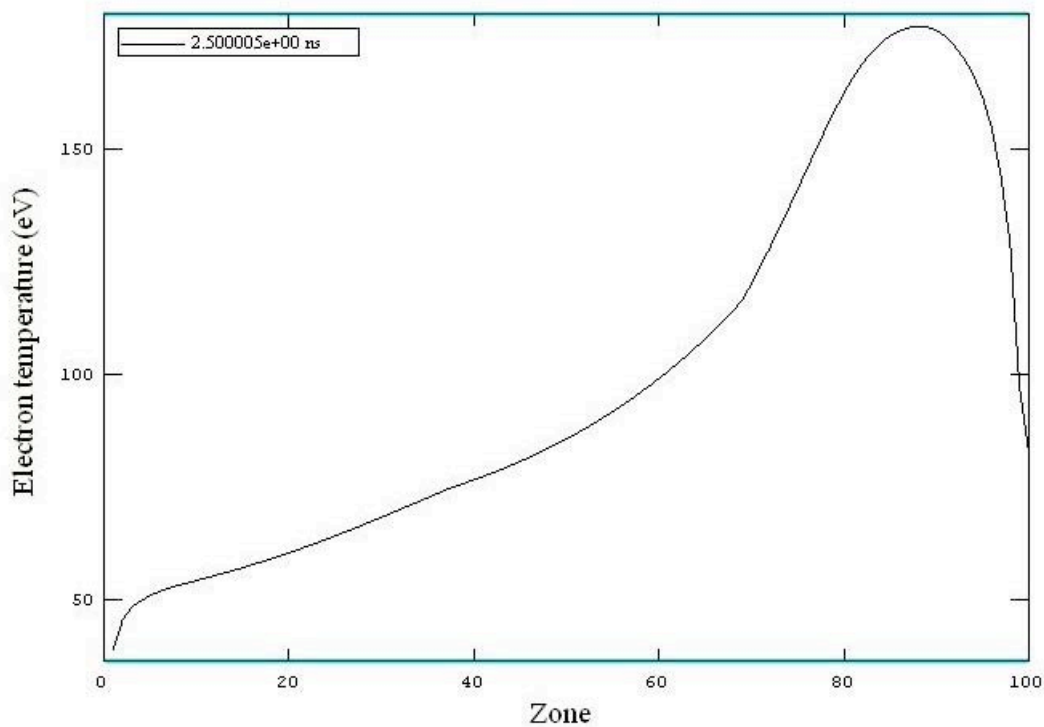


Figure 34. Electron temperature spatial profile at 2.5 ns for SiO₂-6% Ti using Helios

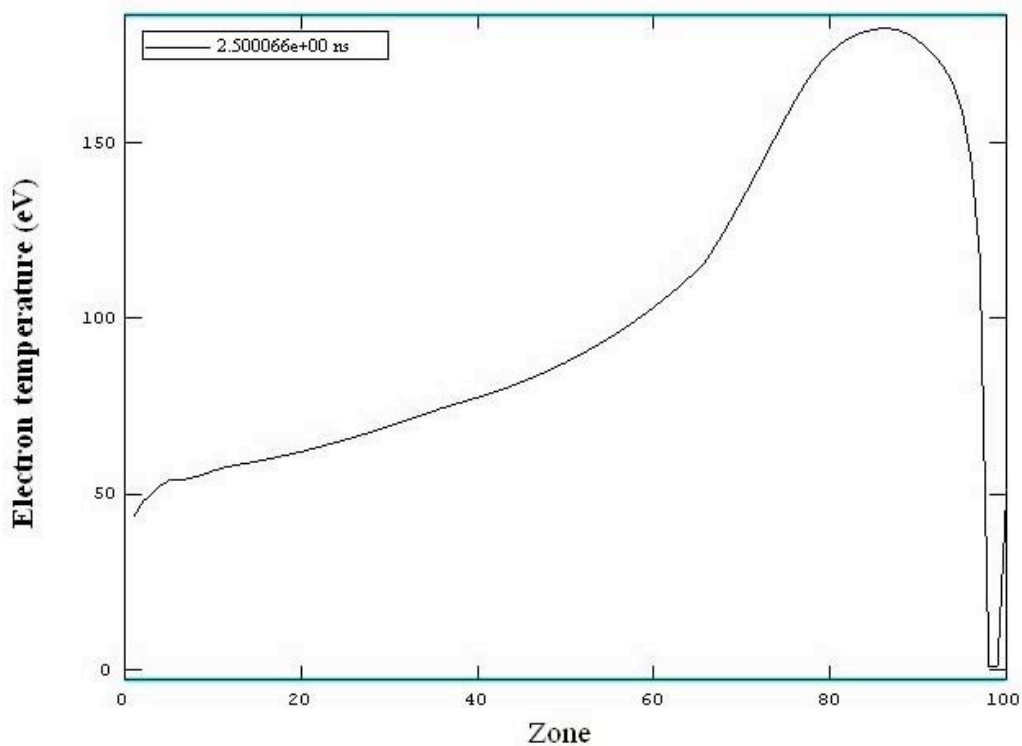


Figure 35. Electron temperature spatial profile at 2.5 ns for SiO₂-2% Ti using Helios

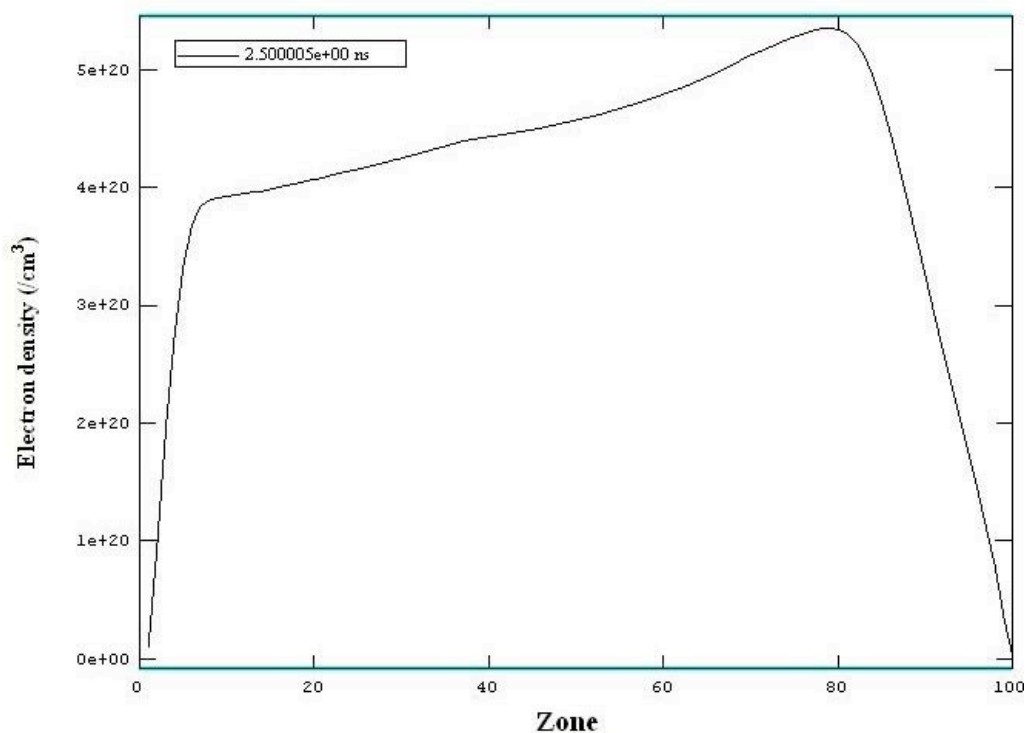


Figure 36. Electron density spatial profile at 2.5 ns for SiO₂-6% Ti using Helios

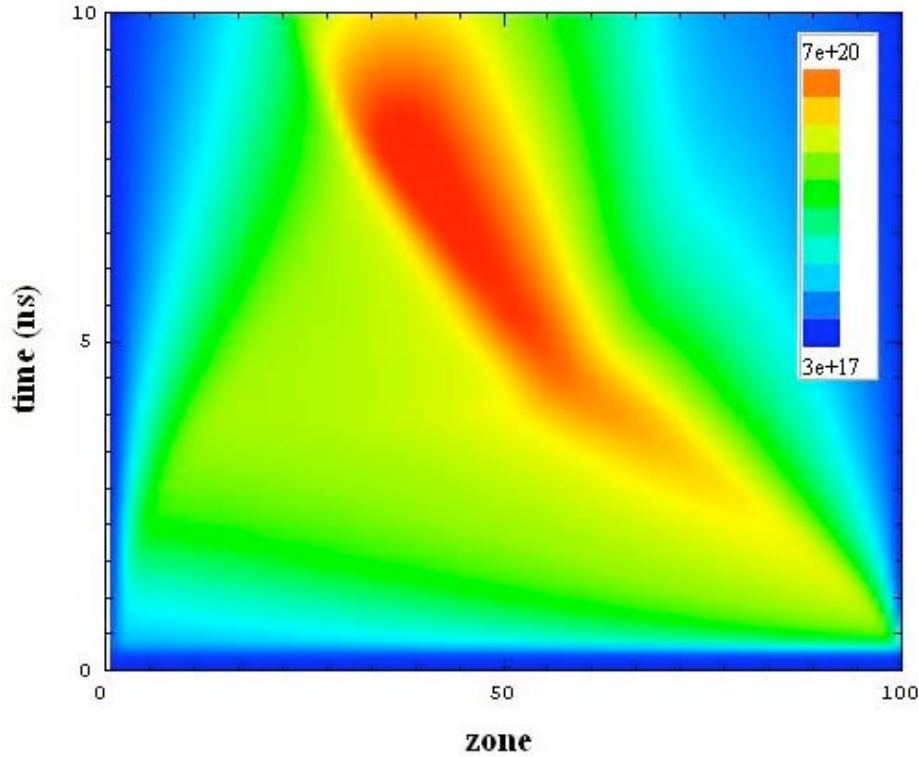


Figure 37. Contour plot of electron density for the 6% Ti case

As discussed in Section 2.1.2, we noticed a tendency for the electron density to rise in the central part of the target *after the laser is removed*. Figure 37 shows a color contour plot of the time and space dependence of electron density. The increase in electron density tracks an increase in mass density, which indicates that the target is being compressed toward the center by hydrodynamic blowoff on each end.

3.2 Increase in SiO₂ density from 2 to 8 mg/cm³

The second experimental parameter we varied was the density of the target. As shown in Figure 4, the laser is not penetrating into the target very well even for the case of 2 mg/cm³. Not surprisingly, Figure 38 shows even strong absorption at 8 mg/cm³. Only the outermost 5 nodes directly absorb the laser. Figure 39 shows the evolution of electron density.

After 2.5 ns, the target electron density is remarkably flat, with a value approximately four times higher than the 2 mg/cm³ targets. The charge state, similar to that of Figure 5, remains He-like during the majority of the pulse. The electron temperature profiles are also quite uniform after about 2.5 ns. The temperature of the front side of the target is depressed as compared with the 2 mg/cm³ case, but still quite uniform. Figure 39 shows a similar behavior for the electron density.

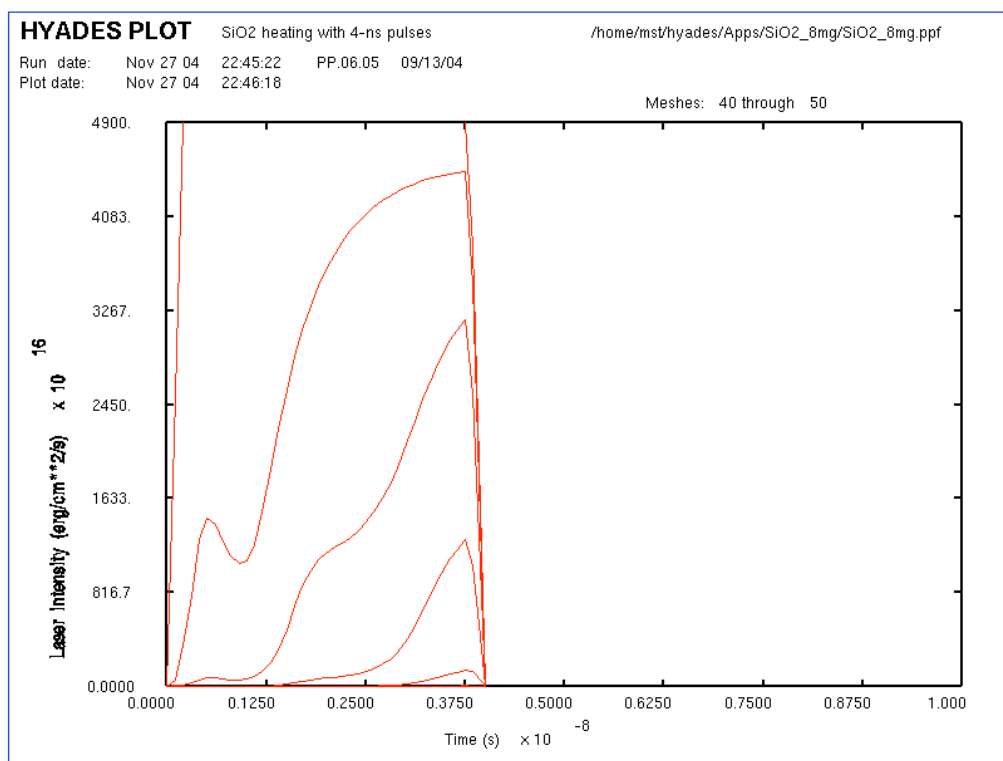


Figure 38. Time history of laser flux in the outermost 10 nodes of the 8 mg/cm^3 target

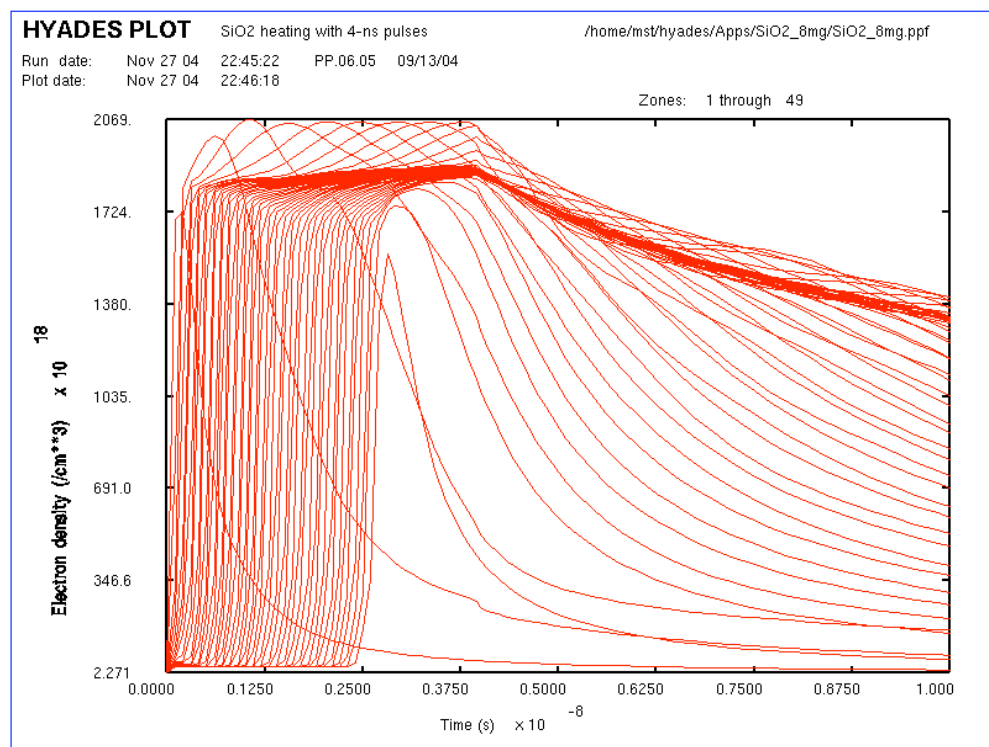


Figure 39. Electron density history for the 8 mg/cm^3 target

Figure 40 clearly shows the process of burn-through. Target heating in this case is not caused directly by the laser. Rather, a radiation driven “burn wave” propagates from front to back. Figure 41 shows the mesh radiative heat flux in erg/cm²/s. The magnitude reaches approximately 50% of the incident laser heat flux. The spectrum of re-emission is centered at shorter wavelengths where the plasma is underdense, permitting transport of radiation into the bulk of the target. After the 2.5 ns required to burn through, the final temperature profile is homogenized as a result of strong radiation coupling throughout the target.

3.3 Decrease of thickness to 0.5 mm

After observing the strong absorption of the laser the front half of the target in the low-density (2 mg/cm³) base case, we decided to examine a case that was tailored to allow all of the target to experience direct heating by the laser. We chose a case with 0.5 mm thickness, keeping all of the other parameters fixed.

Figure 42 shows the laser flux through each zone vs. time. Unlike the previous cases, the laser is clearly transmitted into the deepest parts of the target. The absorption is relatively uniform and relatively complete. The electron temperature, however, is **not** more uniform as compared with the base case. Figures 43 and 44 show that the magnitude of the electron temperature is roughly the same, but this case is slightly *less* uniform than the base case, and certainly less uniform than the high density case. It appears that optically thin laser absorption is less effective at homogenizing the temperature as compared with either a laser propagation wave or a radiation burn wave.

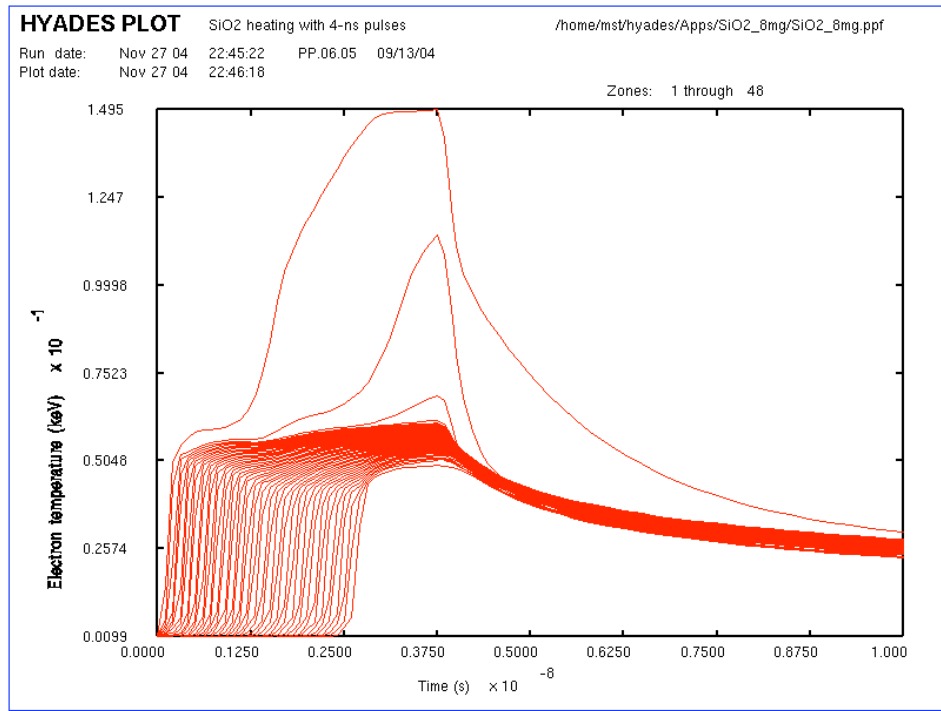


Figure 40. Electron temperature history for the 8 mg/cm³ target

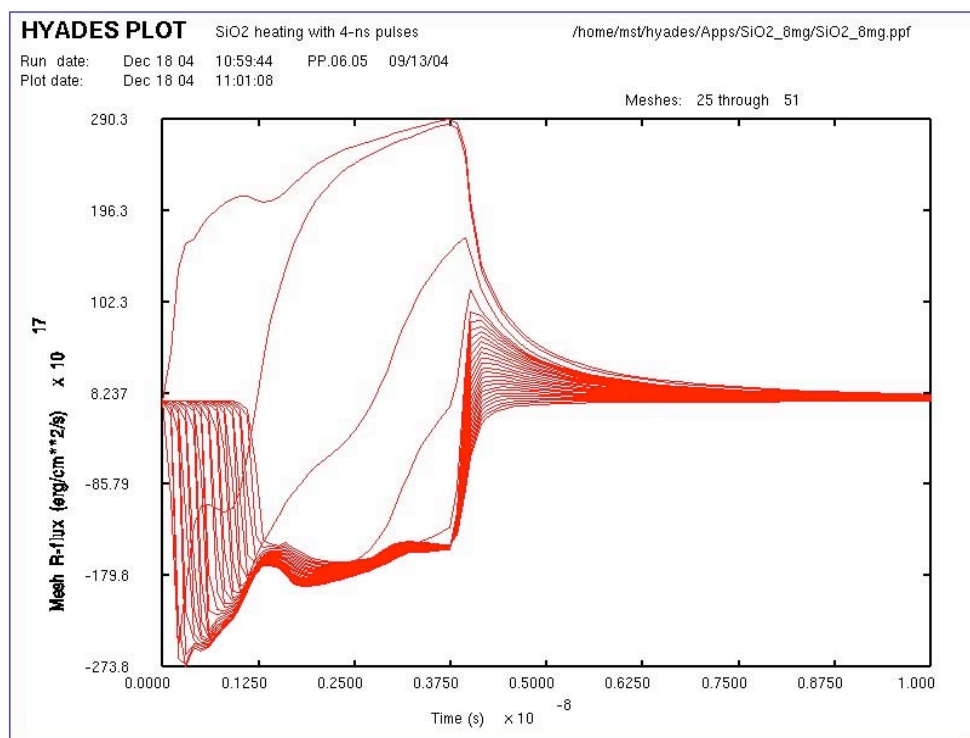


Figure 41. Mesh radiative heat flux as a function of time for the 8 mg/cm³ target

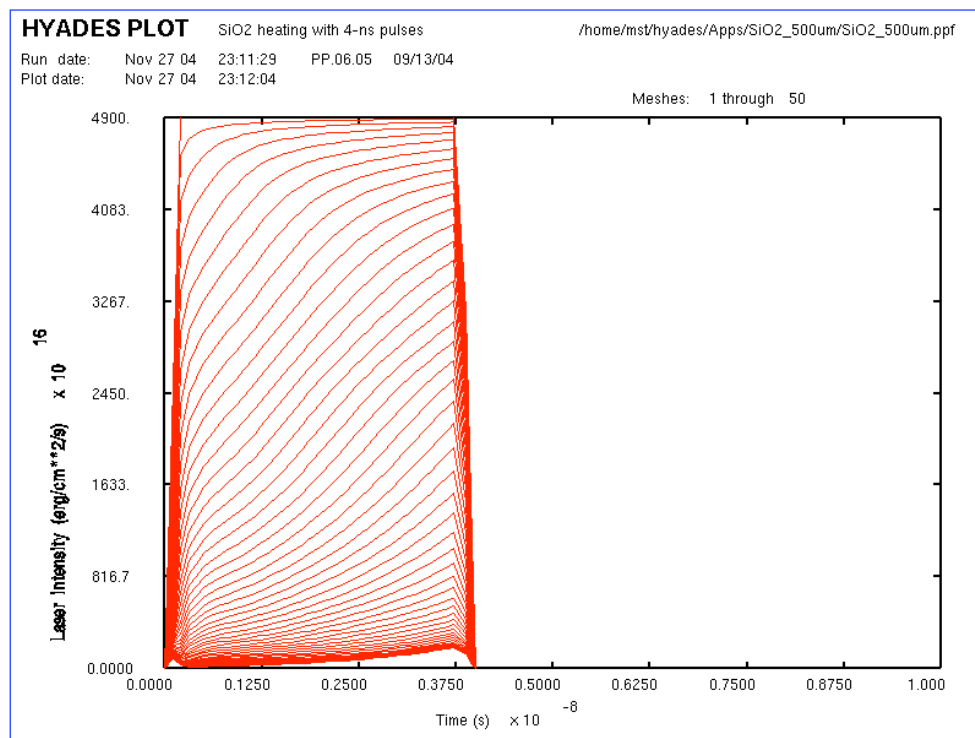


Figure 42. Time history of laser flux in the 0.5-mm thick, 2 mg/cm³ target

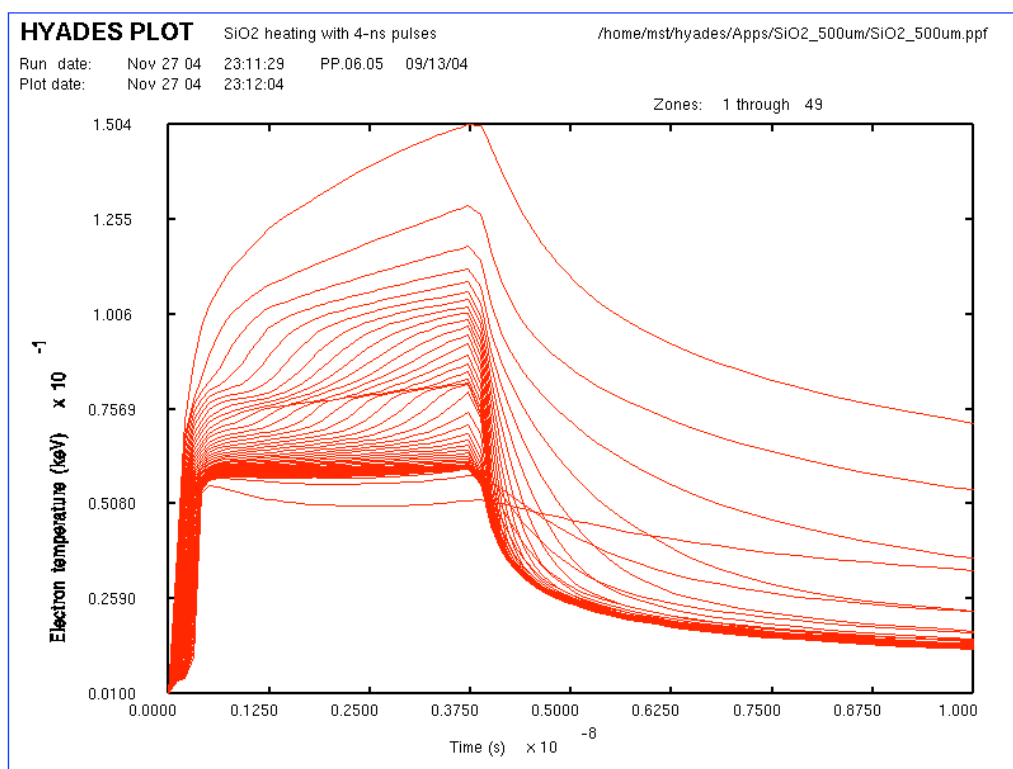


Figure 43. Electron temperature history for the 0.5-mm target

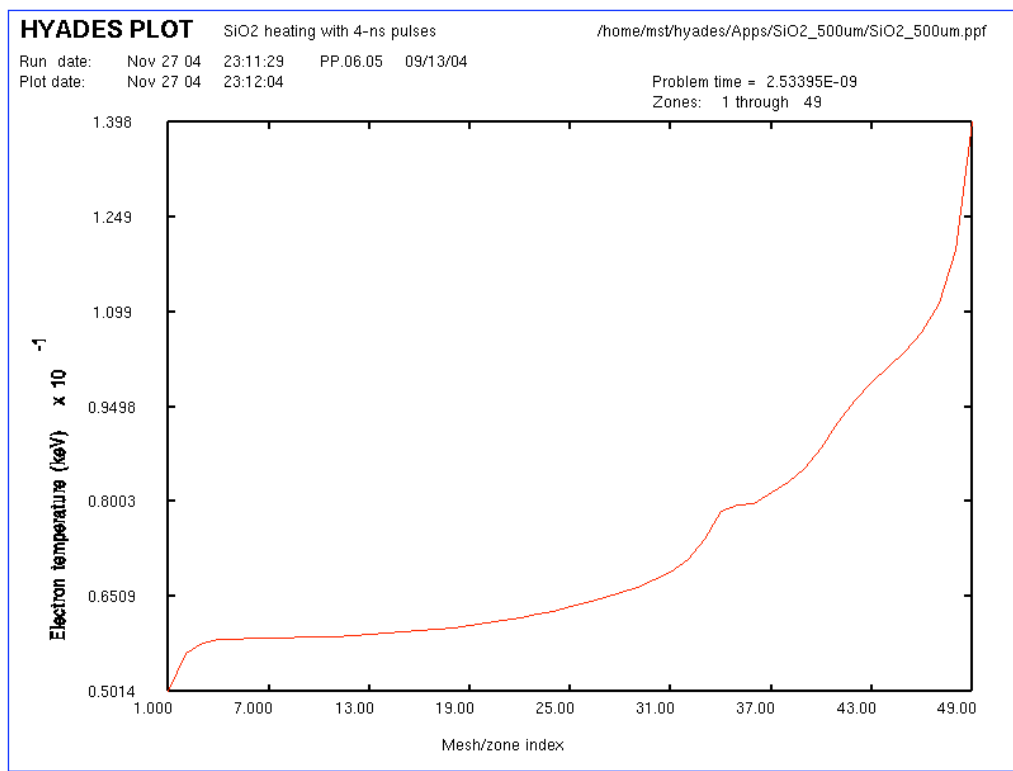


Figure 44. Electron temperature profile at 2.5 ns for the 0.5-mm target

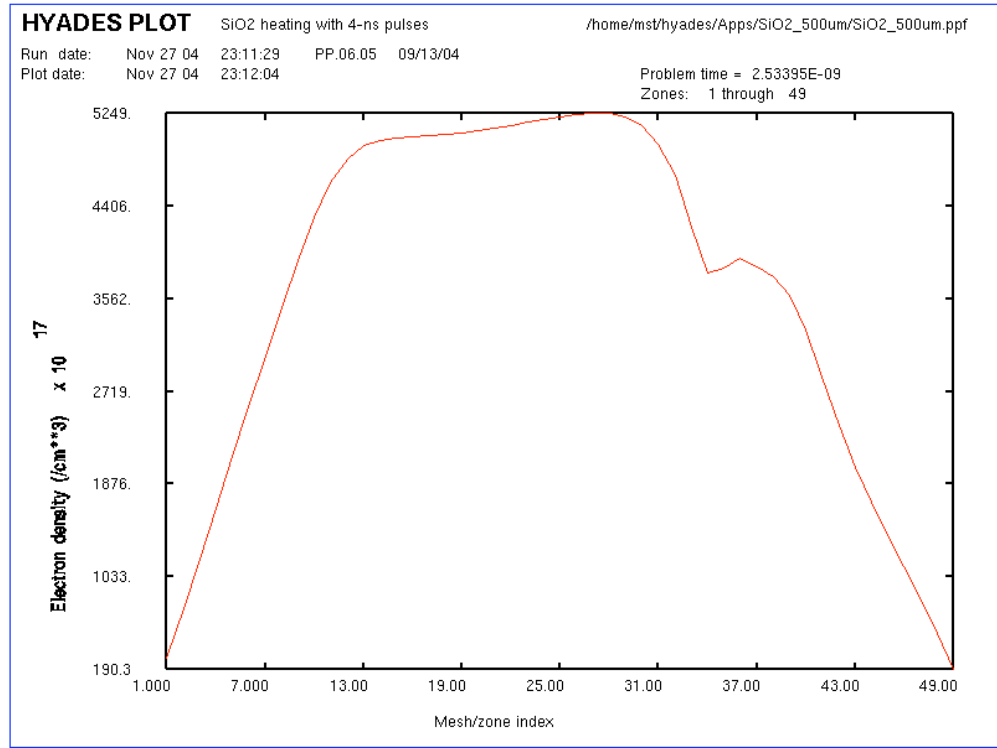


Figure 45. Electron density profile at 2.5 ns for the 0.5-mm target

Figure 45 shows the electron density profile at 2.5 ns for this case. The peak value is very similar to the other cases, but the hydrodynamically affected region appears somewhat larger. In fact, the thickness of the hydrodynamically expanded region is similar to the base case, but appears larger in a relative sense due to the smaller target thickness. If a target that is transparent to the laser is desired, then a better strategy would be to reduce the density further – to about 1 mg/cm³. However, the uniformity of the temperature is actually worse in this case, such that denser targets are probably more desirable.

3.4 Increase of laser intensity from 4.9×10^{12} W/cm² to 3.7×10^{14} W/cm²

3.4.1 High intensity Hyades result

Laser intensities above 10^{14} W/cm² provide much stronger interactions as compared with those at 4.9×10^{12} W/cm². The stability of codes such as Hyades and Helios are tested under these conditions. Figures 46 and 47 show the evolution of electron temperature and density for this laser intensity, keeping all other parameters identical to the base case. These plots provide spatial profiles for time increments of 0.2 ns from 0 to 4 ns. Results after the laser is turned off were excluded; the profiles rapidly collapse and tend to obscure the results during the pulse. Both figures indicate fluctuations in the early stage of the laser pulse. We ran a case with a finer

grid and observed similar behavior, although at a different location in the plasma. We believe these fluctuations are numerical in origin, and not indicative of the real plasma response.

These high-intensity cases are characterized by more rapid heating, more uniform temperature profiles, and a rapid achievement of full ionization (see Figure 48). The peak temperature observed is approximately 1.5 keV.

Figure 49 shows the Lagrangian zone locations vs. time. The target explodes much more rapidly under this value of incident laser intensity. By the end of the pulse (see Figure 47), the peak electron density has dropped by a factor of 2, and the profile has become considerably nonuniform.

Figure 50 shows the laser flux within the target as a function of time. It is apparent that this target becomes optically thin toward the incident laser rather quickly. By the end of the laser ramp-up, the rear side already sees direct exposure, with ~30% of the incident laser flux passing through the target completely. By the end of the pulse, approximately 80% of the incident laser leaks through the target without absorption.

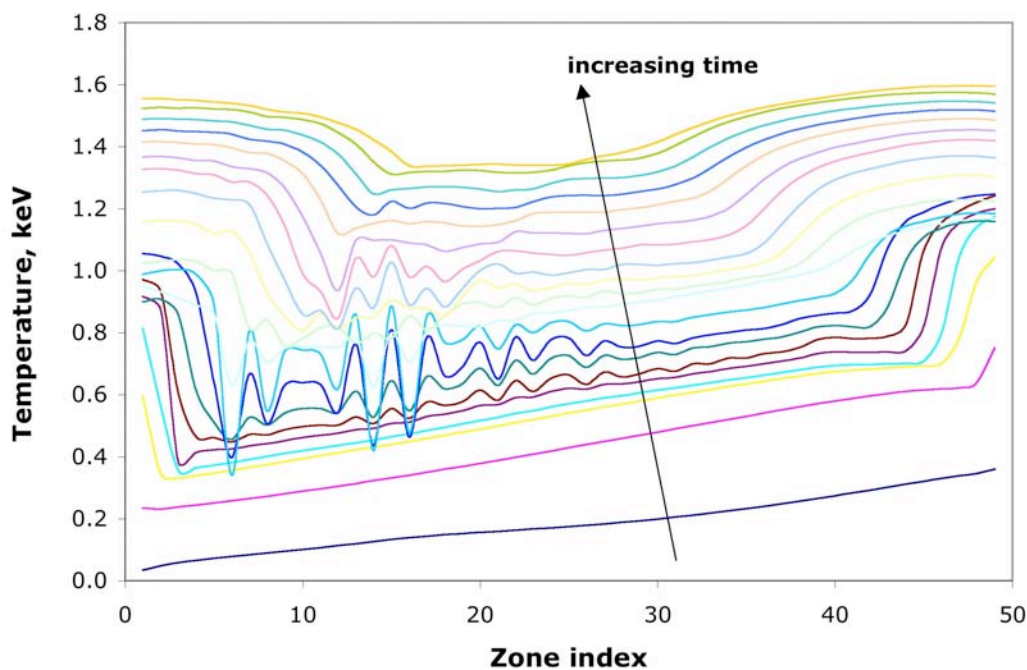


Figure 46. Electron temperature profiles at various times with 3.7×10^{14} W/cm² laser intensity

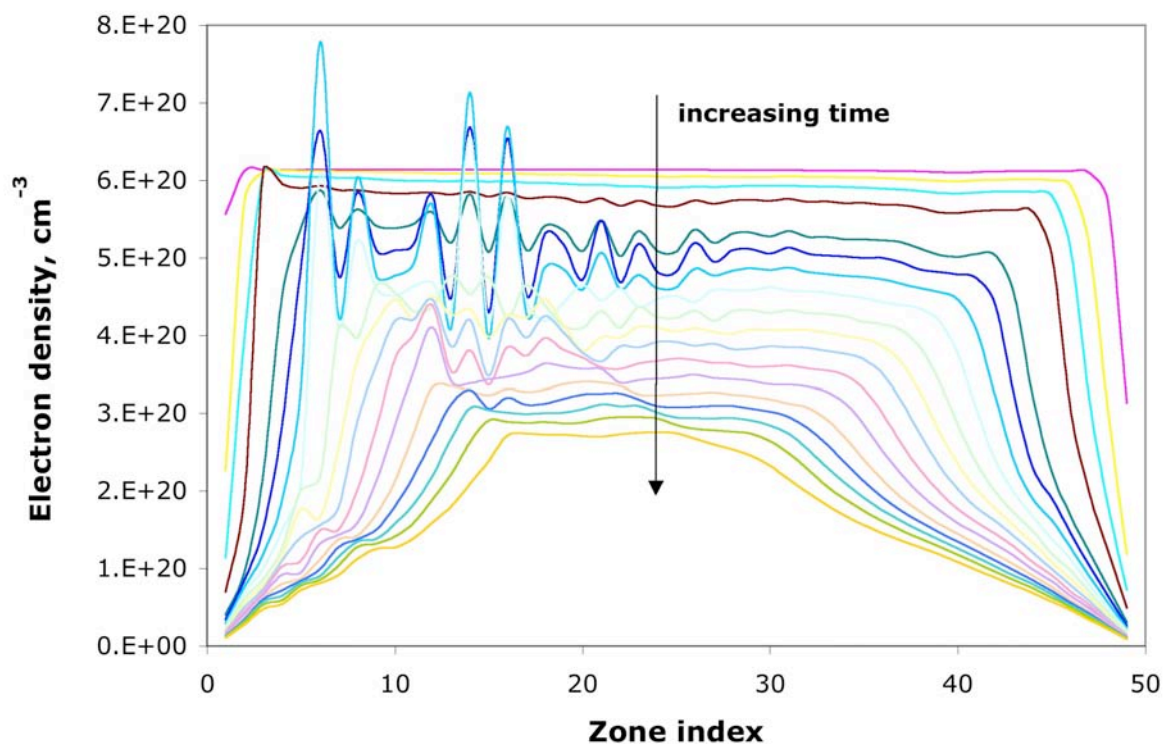


Figure 47. Electron density profiles at various times with $3.7 \times 10^{14} \text{ W/cm}^2$ laser intensity

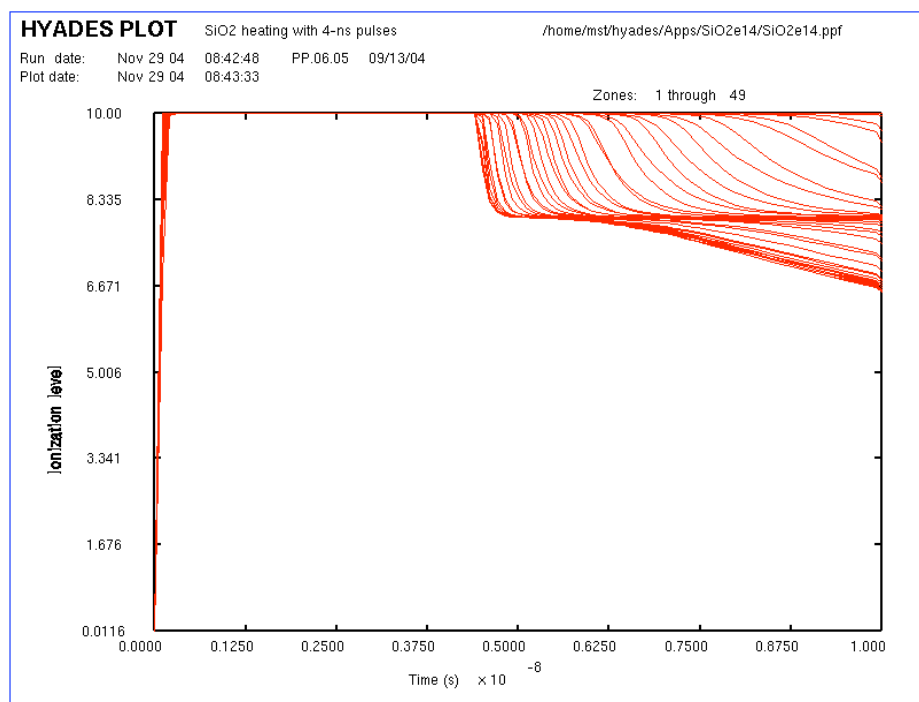


Figure 48. Time history of the charge state with $3.7 \times 10^{14} \text{ W/cm}^2$ laser intensity

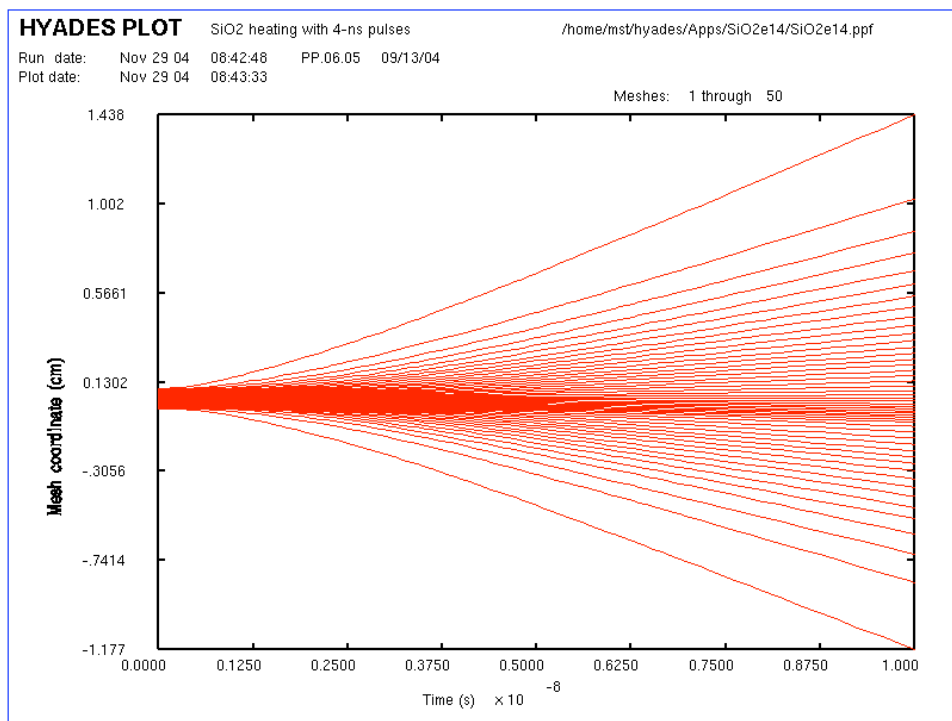


Figure 49. Radial location of the Lagrangian zones with 3.7×10^{14} W/cm² laser intensity

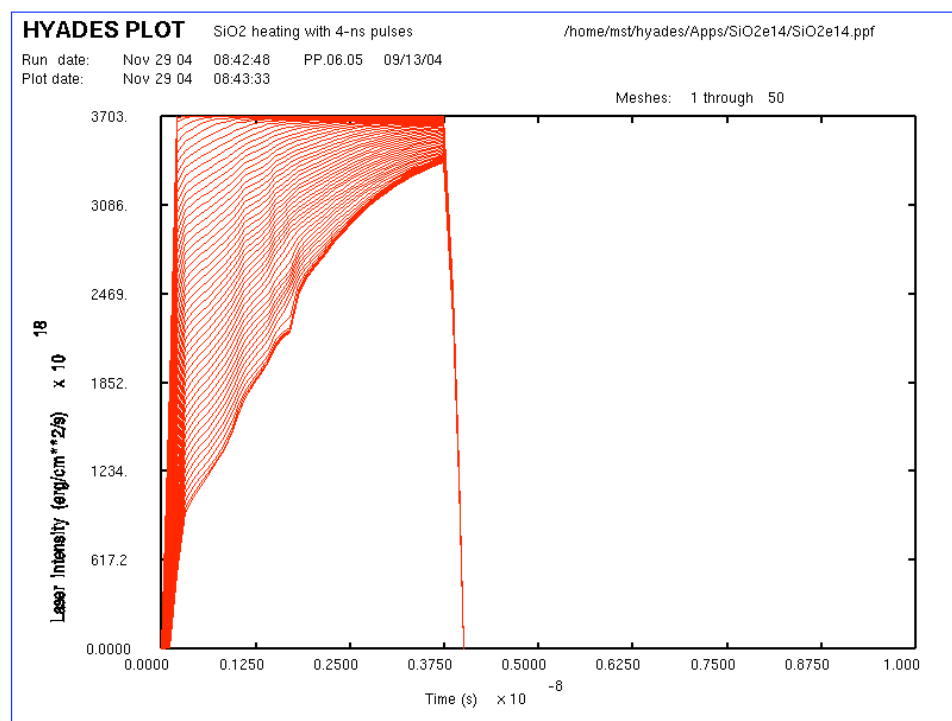


Figure 50. Time history of the laser flux with 3.7×10^{14} W/cm² laser intensity

3.4.2 High intensity Helios results, with and without doping

For the sake of comparison, we also explored the high intensity case using Helios. Figures 51–53 show the response for the target with 6% Ti doping. Figure 51 shows the electron temperature history, which can be compared with the Hyades high-intensity case (Figure 46). Similar to our earlier observations, Helios consistently predicts higher electron temperatures for the same conditions. The profiles are so flat that they can not be distinguished. Figure 52 shows a spatial profile at 2.5 ns. In order to explore the effect of doping at this elevated temperature, we also ran a case with no Ti. As seen in Figure 53, there is no distinguishable difference. This is not surprising; all of the atoms in this plasma are fully stripped, such that atomic processes are relatively unimportant during the laser pulse.

Figure 54 shows the electron density profile at 2.5 ns. The results are in general agreement with Hyades results, showing substantial hydrodynamic motion at this point in the laser pulse.

Based on the observation of the limited effect of dopant on the temperature evolution, we also explored the importance of spectral detail in the opacities. Figure 55 shows the result of this case. As the laser intensity is increased to $3.7 \times 10^{14} \text{ W/cm}^2$ and successive atomic shells become stripped, it is expected that the *early time* electron temperature of these underdense plasmas will be relatively unaffected by a lack of spectral detail in the gray opacity data. As the plasma cools and recombines, atomic shells begin to repopulate. The radiation produced from *late time* processes depends upon specific spectral line properties such as excited state energy levels, atomic oscillator strengths, degeneracies, and ground state populations (for self-absorption considerations). To properly account for the intensity of line emission and associated absorption coefficient, spectral detail then becomes necessary.

Figure 55 shows that the peak electron temperature varies less than 20% between the gray and full spectral opacity runs. Rapid cooling is indicated in the early phase of the laser pulse, dropping the temperature from over 2 keV to approximately 1.5 keV.

In the late time recombination phase of the plasma, the emission begins to deviate significantly from a Planckian spectrum, resulting in an elevated electron temperature for the spectrally resolved case. This suggests that above a certain threshold temperature, spectral lines may become self-absorptive, resulting in trapped radiation that couples to thermal electrons.

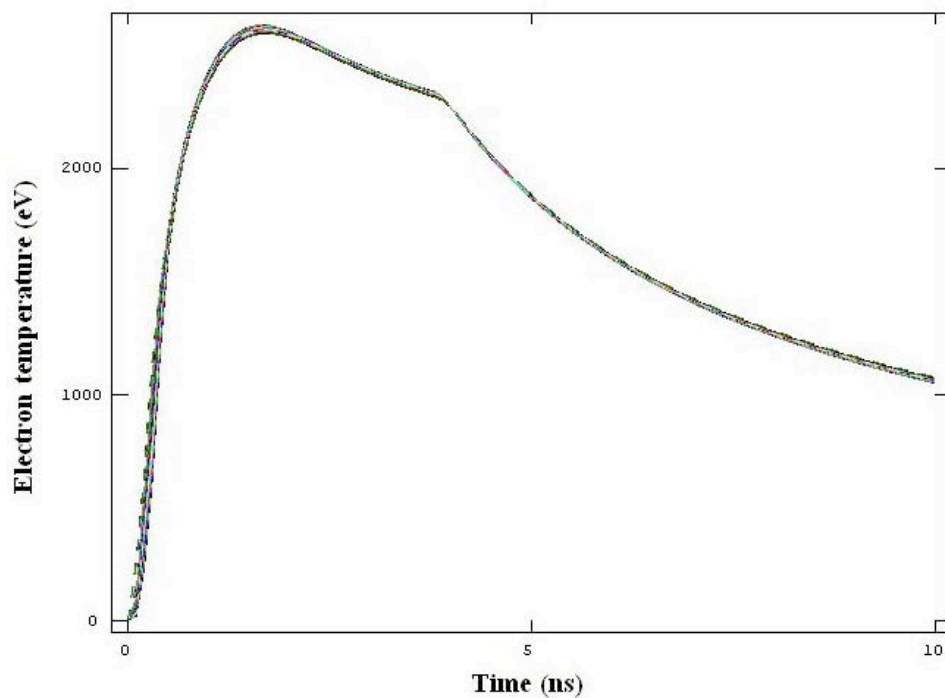


Figure 51. Electron temperature history for SiO₂-6% Ti using Helios

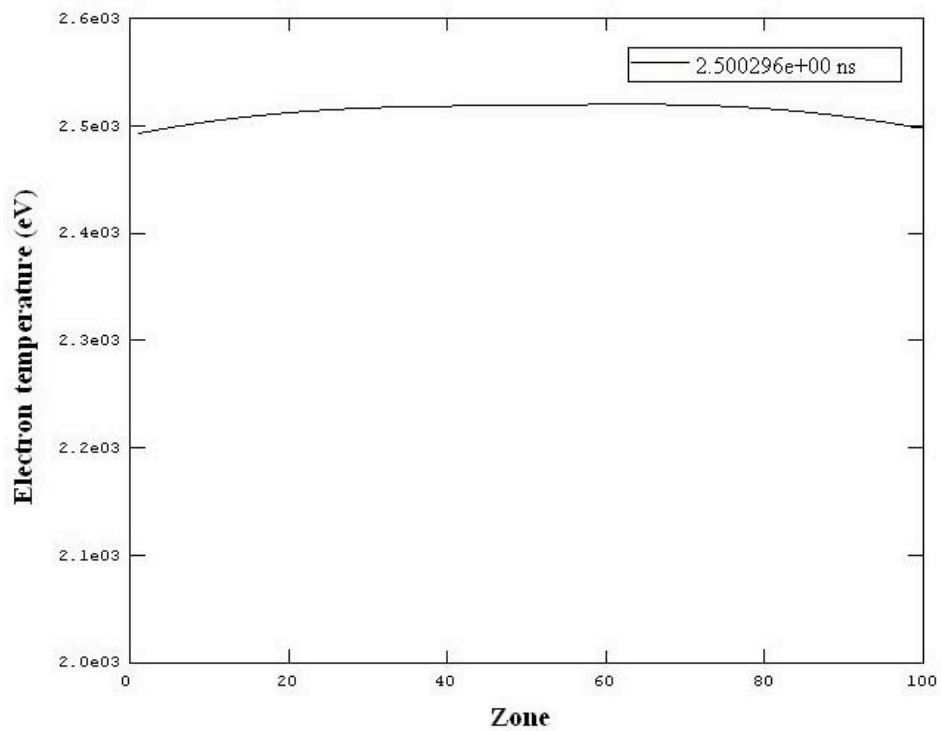


Figure 52. Electron temperature spatial profile at 2.5 ns for SiO₂-6% Ti using Helios

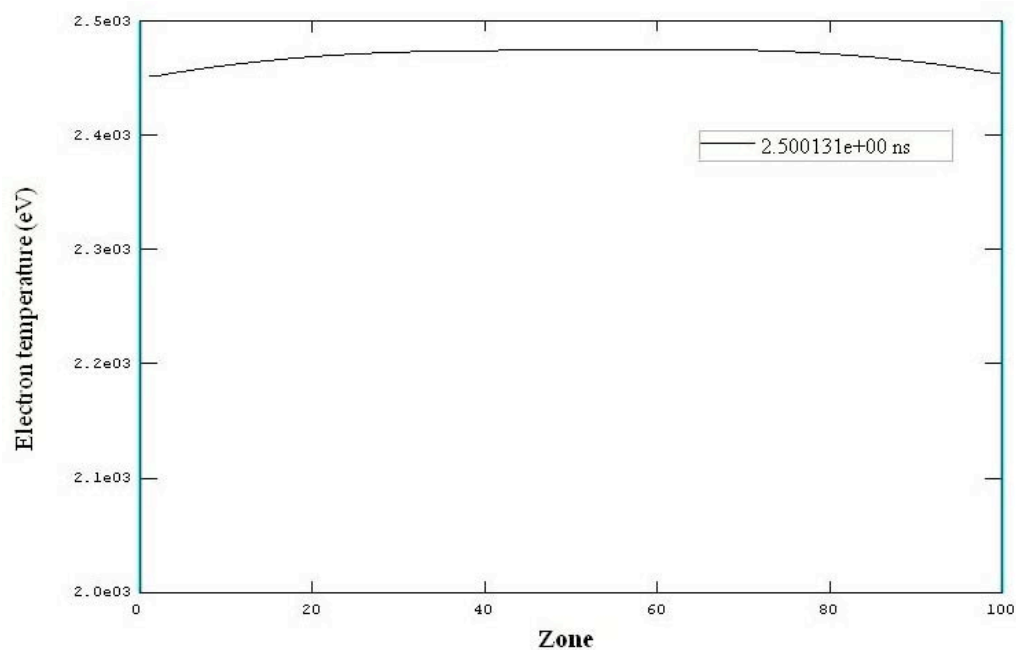


Figure 53. Electron temperature spatial profile at 2.5 ns for SiO₂-0% Ti using Helios

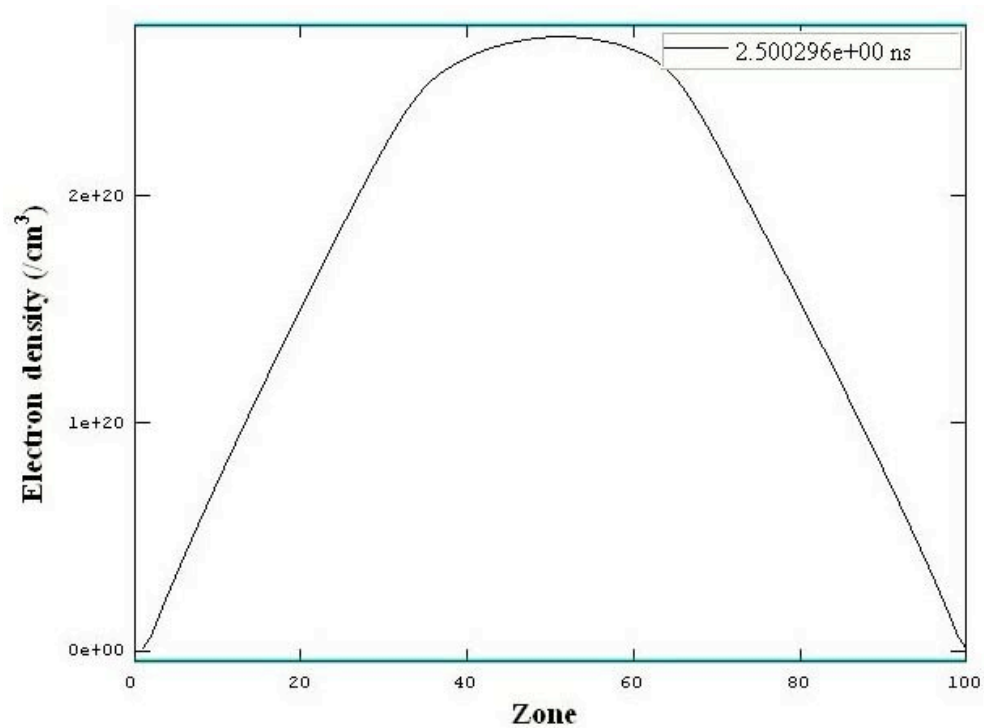


Figure 54. Electron density spatial profile at 2.5 ns for SiO₂-6% Ti using Helios

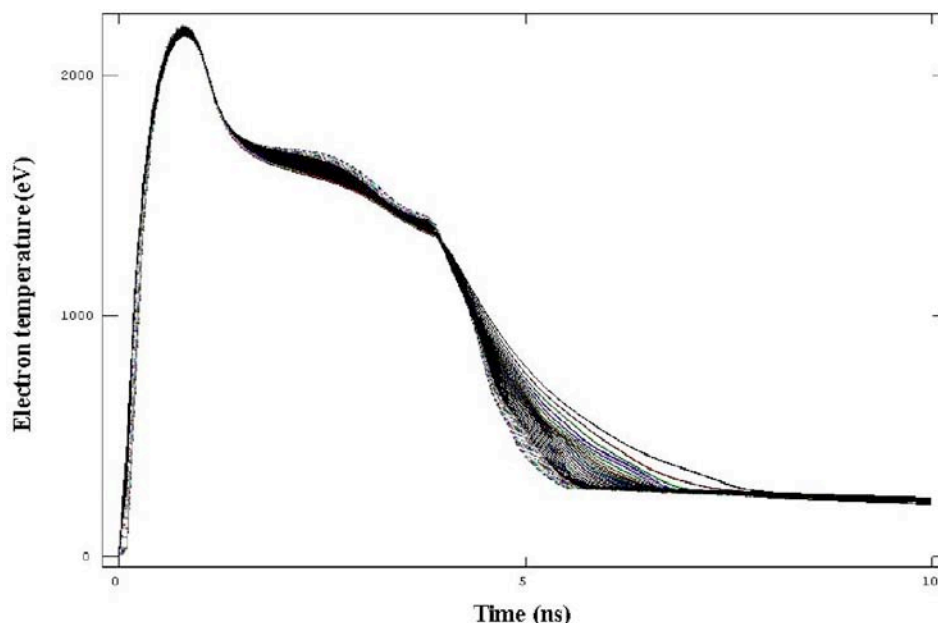


Figure 55. Electron temperature history for SiO₂-6% Ti using Helios with gray opacities

4. Summary and conclusions

We have examined the response of low-density SiO₂ aerogel targets to short pulse laser irradiation using the radiation hydrodynamic models Hyades and Helios. We explored the sensitivity of the results to changes in the models and data used, and then characterized the response over a range of parameters including Ti dopant concentration, target density, and laser intensity.

A “modeling base case” was explored in depth in order to understand the baseline behavior of a pure SiO₂ target exposed to the lower value of laser intensity. This study illuminated the basic behavior of the 2 mg/cm² underdense target. For this target, the laser “burns in” through a combination of a “laser absorption wave” and upconversion of energy to shorter wavelengths, which propagate more easily through the target. The rear of the target reaches a temperature of 50-100 eV (depending on the code used), and the front reaches 100-200 eV, with relatively strong gradients resulting from direct laser heating.

A laser propagation wave occurs in underdense plasmas as a result of the decrease in inverse bremsstrahlung absorption (which predominates in underdense cases) with heating. A radiation propagation wave occurs as a result of the upconversion of laser radiation into shorter wavelength atomic radiation. The optical depth generally decreases with increasing wavelength, and so the converted energy propagates more deeply as the front of the target becomes hotter.

In every case studied, the electron density achieves quite uniform values which are determined primarily by the ionization state of the target. At the lower intensity, the target becomes He-like ($\langle Z \rangle = 8$) and maintains a constant density until hydrodynamic expansion explodes the target.

This occurs near the end of the 4-ns laser pulse. At the higher intensity, the target is fully stripped ($\langle Z \rangle = 10$). Hydrodynamic expansion is far more rapid, and already results in a drop in density and very nonuniform profiles after 1 ns.

Targets with lower mass or mass density *do not* appear to heat more uniformly. The 8 mg/cm³ case had the most uniform temperature, although it required more time for a radiation wave to penetrate. Laser absorption in this target was confined to a few nodes near the surface throughout the entire pulse. The 0.5-mm low-density case heated quickly, but did not lead to a more uniform temperature. Apparently plasmas heated indirectly are able to establish more uniform profiles than those heated directly by the incident laser.

Since the 2 mg/cm² target was not optically thin toward the laser at the lower intensity level, we explored a case with 0.5 mm thickness. Indeed, this target allowed light to penetrate fully into the target, but the smaller dimension also led to a substantial fraction of the mass being ejected by hydro motion before the entire target heats up. A better way to achieve optically thin targets would be to reduce the mass density. However, as mentioned above, this *is not* likely to lead to more uniform temperatures unless the target is so thin optically that the intensity does not vary substantially through the target.

The high intensity case behaved dramatically different than the base case. Due to rapid, complete ionization, this case became relatively insensitive to atomic processes. The temperature profile remained extremely flat throughout the laser pulse. The electron density has reasonably uniform profiles initially, but the hydrodynamic expansion is so extreme that the density drops almost immediately (after 1 ns) and becomes centrally peaked. At the same time, the plasma temperature gradually increases until the end of the pulse. By the time the plasma reaches 1 keV (2 keV for Helios runs), the density profile is already significantly distorted.

Since radiation transport is one of the dominant mechanisms by which targets heat, cool and transport energy, treating the opacity, or absorption and re-radiation of photons is fundamental to determine the plasma evolution. We explored different opacity models and the effect of spectral resolution. In order to explore the effect of spectral detail in Hyades, we attempted to model multi-group radiation transport with the built-in model, and we attempted to import spectrally resolved PROPACEOS data. Unfortunately, neither of these efforts was successful.

Helios treats spectrally resolved opacities as an integral feature of the code. We analyzed cases with 1, 50, and 500 frequency groups. For the single-group case, the data are averaged using the Rosseland mean. The results in pure SiO₂ showed modest influence of spectral detail.

In order to explore the effect of dopant, we generated gray opacities for Hyades and we obtained data from Prism Computational Sciences for SiO₂-2% Ti and SiO₂-6% Ti. Not unexpectedly, dopant had little influence on the target evolution in the case of gray opacities. Spectral averaging effectively smears out atomic processes. However, even in the case of spectrally resolved opacities used in Helios, still there was very minor influence of the dopant for the low-intensity case. For the high-intensity case, there is even less effect due to the complete ionization of the target.

Future modeling activities will focus on modeling of non-LTE processes and a closer examination of the target emissions after the laser pulse.

Acknowledgements

The authors would like to thank Jon Larsen at Cascade Applied Sciences, Joe MacFarlane, Igor Golovkin and Pam Woodruff at Prism Computational Sciences for advice and assistance in the use and interpretation of their software and data.

References

1. J. T. Larsen and S. M. Lane, "HYADES – A plasma hydrodynamics code for dense plasma studies," *J. Quant. Spectrosc. Radiat. Transfer*, **51** (1994) 179-186.
2. I. E. Golovkin, J. J. MacFarlane, P. R. Woodruff, L. A. Welser, D. L. McCrorey, R. C. Mancini, J. A. Koch, "Modeling of Indirect-Drive ICF Implosions using 1D Hydrodynamic Code with Inline Collisional-Radiative Atomic Kinetics," *Inertial Fusion Science and Applications 2003*, Monterey CA, Sept. 2003 (pp. 166-169).
(see also <http://www.prism-cs.com>)
3. P. G. Burkhalter, M. J. Herbst, D. Duston, J. Gardner, M. Emery, R. R. Whitlock, J. Grun, J. P. Apruzese, and J. Davis, "Density and temperature profiles within laser-produced plasmas in the classical-transport regime," *Phys. Fluids* **26**, 3650-3659 (1983).
4. NLTE Code Comparisons Workshop reports, 1996 and 1998.
5. S. P. Lyon and J. D. Johnson (Eds.), "SESAME, the Los Alamos National Laboratory equation of state database," Los Alamos National Laboratory report LA-UR-92-3407 (1992).
(see also http://t1web.lanl.gov/newweb_dir/t1sesame.html)
6. J. Denavit and D.W. Phillion, "Laser ionization and heating of gas targets for long-scale-length instability experiments," *Phys. Plasmas* **1**, 1971 (1994).
7. R. Siegel and J. R. Howell, Thermal Radiation Heat Transfer, Hemisphere Publishing Corporation, 1992.

Appendices

Appendix A. Original Statement of Work

Proposal for Collaboration on EUV/XUV experiments and modeling

Mark S. Tillack

Mechanical and Aerospace Engineering Department
University of California, San Diego
11 June 2004

We propose to collaborate with LLNL on spectroscopy experiments and analysis related to x-ray emission in the EUV and XUV range from laser-produced plasmas. This work is in support of experiments in progress at the Nike and Janus laser facilities. Members of the fusion energy group at the University of California San Diego will run simulations and help analyze data as specified by LLNL personnel.

The following five elements are proposed for the scope of work:

1. Using the hydrodynamics code Hyades, provide analysis and predictions of the plasma conditions attained by Ti-aerogel in Nike and Janus laser experiments. This will include license fees for Hyades.
2. Support a graduate student to run calculations with Hyades and Cretin.
3. Evaluate the use of different atomic models for the simulations of the experiments.
4. Travel for discussions on results and future plans.
 - 1 week total to be split between LLNL and UCSD locations
5. Develop a detailed plan for continued collaboration and student support. This includes identifying appropriate experimental or theoretical themes of research relevant to the development of absolute spectroscopic diagnostics.

Appendix B. Input and source files

Appendix B.1 Hyades input file for the base case

```
SiO2 heating with 4-ns pulses
c
c 1 mm (.1 cm) slab of SiO2 with 50 nodes, NO feathering
c
mesh 1 51 0.00 0.1 1.0
c
c fully dense glass is 2.6 g/cc
c this run uses 0.1% dense SiO2 (2.04e-3 g/cc)
c and initial electron temperature of 1 eV
c
region 1 51 1 2.04e-3 0.001
c
c Z=10, A=20
c EOS for silica is 24
c opacity of quartz is 1022
c
material 1 10. 20. 1.
eos 24 1
eos 1022 1
c
c 4.9e+12 watts/cm**2 (10^21 erg/cm2/s), 0.248 um laser source
c rises in 5 fs, flat-topped for 10 fs
c
source laser 0.248 -51
tv 0. 0.
tv 0.2e-9 4.9e+19
tv 3.8e-9 4.9e+19
tv 4.0e-9 0.
c
pparray r dene te tr deplas grad u zbar xmass acc xlsint
c
c use 0.1 ns output time intervals initially, stop after 1 ns
c
parm postdt 1.e-10
parm tstop 1.e-8
c
```

Appendix B.2 Source listing for spectral averaging routine

```
implicit double precision (a-h,o-z)
character*120 header
character*15 filename
character*1 tab
dimension d(100), t(100), e(10000), a(10000)
dimension ross(100,100), plan(100,100), opacr(100), opacp(100)
external rossave, planckave, planck, planckd

tab = "\t"

open(unit=5, file="SiO2.dat", recl=132)
open(unit=6, file="averages", status="unknown")

read(5,*) nt                      ! number of temperatures
read(5,*) (t(i),i=1,nt)          ! temperatures
read(5,*) nd                      ! number of densities
read(5,*) (d(i),i=1,nd)          ! densities
read(5,*) ng                      ! number of energy groups
read(5,*) (e(i), i=1,ng+1)       ! energies

write(6,*) "Planck and Rosseland Averages"

do id=1,nd
do it=1,nt
  temp = t(it) * 11604.4

  read(5,2) header
  read(5,*) (a(n), n=1,ng)      ! Rosseland opacity

  read(5,2) header
  read(5,*) (a(n), n=1,ng)      ! Planck emission opacity

  read(5,2) header
  read(5,*) (a(n), n=1,ng)      ! Planck absorption opacity

c place these two statements after the appropriate read statement
  plan(it,id) = planckave(a,e,temp,ng)
  ross(it,id) = rossave(a,e,temp,ng)
c -----

  enddo
enddo

1 format(2x,10(2x,e12.4))
2 format(a120)

c at this point the data has been entered and averages done.
c next, we want to interpolate opacity vs. T at n=5x10^20/cm3

write(6,*) "opacity vs. temperature at n=5x10^20"

dout = 5.e20
```

```

ir = 1
do while (dout .gt. d(ir))
  ir = ir + 1
  if(ir.gt.nd) then
    write(*,*) "desired density outside range"
    stop
  endif
enddo

c ir is the index where the density data point exceeds 5e20
c frac=1 at dout=d(ir)
  frac = (dout-d(ir-1))/(d(ir)-d(ir-1))
  write(6,*) "ir=",ir
  write(6,*) "frac=",frac

c interpolate the opacity vs. temperature and write to output file
  do io = 1, nt
    opacr(io) = frac*ross(io,ir) + (1.-frac)*ross(io,ir)
    opacp(io) = frac*plan(io,ir) + (1.-frac)*plan(io,ir)
    write(6,5) t(io), tab, opacp(io), tab, opacr(io)
  enddo

3 format(e12.4,a1,e12.4)
5 format(e12.4,a1,e12.4,a1,e12.4)
stop
end

c *****
c Perform the Rosseland integration
  function rossave(a,e,temp,ngroup)
    implicit double precision (a-h,o-z)
    dimension e(10000), a(10000)

    top = 0.
    denom = 0.

    do i=1,ngroup
      de = e(i+1)-e(i)
      eave = 0.5*(e(i+1)+e(i))
      xl = 1.24/eave          ! wavelength in microns
      pl = planckd(temp,xl)
      top = top + de * pl / a(i)
      denom = denom + de * pl
    enddo
    rossave = denom/top

    return
  end

c *****
c Perform the Planck integration
  function planckave(a,e,temp,ngroup)
    implicit double precision (a-h,o-z)
    dimension e(10000), a(10000)

    top = 0.

```

```

denom = 0.
do i=1,ngroup
  de = e(i+1)-e(i)
  eave = 0.5*(e(i+1)+e(i))
  xl = 1.24/eave          ! wavelength in microns
  pl = planck(temp,xl)
  top = top + a(i) * pl * de
  denom = denom + pl * de
enddo

planckave = top/denom
return
end

c *****
c Evaluate the Planck function at T
  function planck(t,xl)
    implicit double precision (a-h,o-z)
    data c1, c2, pi / 5.9555e7, 1.4388e4, 3.1415926 /
    planck = 2.*pi*c1/xl**5/(exp(c2/xl/t)-1.)
    return
  end

c *****
c Evaluate the Planck derivative at T
  function planckd(t,xl)
    implicit double precision (a-h,o-z)
    data c1, c2, pi / 5.9555e7, 1.4388e4, 3.1415926 /

c we evaluate this by differencing because the function
c itself is ill-behaved

    t2=t*1.001
    p1 = planck(t,xl)
    p2 = planck(t2,xl)
    planckd = (p2-p1)/(t2-t)
    return
  end

```

Appendix B.3 Source listing for Sesame mixture generator

```

c This routine creates Hyades EOS and opacity files for mixtures
c using a mass-weighted arithmetic average of the two input datasets.
c We assume here that the mixture plasma has a single state (n,T),
c and that the eos and opacity of the constituents are evaluated at
c the mixture (n,T). The values of (n,T) in the output are chosen
c to match those of the primary constituent (file 1). Interpolation
c on (n,T) is used to add a fraction of the second dataset. The (n,T)
c ranges are truncated if the data range of the second constituent
c is smaller than the first. This avoids extrapolation outside the
c database for either constituent.

c INPUT FILE PARAMETERS (eosmix.dat)
c header      = output file header line
c numeos      = a unique eos numeric identifier for the mixture
c filename1   = first input file
c filename2   = second input file
c filename3   = output file name
c wtp         = mass fraction of the second constituent (2nd file)

c Sesame file format:
c line 1 -- header
c line 2 -- property identifier, Zbar, Abar, rho, npts
c           (where npts is the remaining number of variables in the file)
c line 3 -- number of density values, number of temperature values,
c           density array, temperature array, first property array,
c           second property array

c for opacities, properties are Rosseland and Planck opacities
c for EOS it's pressures and energies

c the order of indexing in the parameter arrays is to scan densities
c first -- i.e., p(nd,nt) scans through nd points, nt times

c plf1 - first property in first input file
c p2f1 - second property in first input file
c plf2 - first property in second input file
c p2f2 - second property in second input file
c plf2i - first property in second input file, interpolated
c p2f2i - second property in second input file, interpolated
c plf3 - first property in output file
c p2f3 - second property in output file

c -----
c -- BEGIN PROGRAM --
c -----
      character*80 header, dummy
      character*12 filename1, filename2, filename3
      real*4 array1(10000), array2(10000), array3(10000)
      real*4 d1(100), t1(100), d2(100), t2(100)
      real*4 plf1(100,100), p2f1(100,100), plf2(100,100), p2f2(100,100)
      real*4 plf2i(100,100), p2f2i(100,100), plf3(100,100), p2f3(100,100)

      external xmaxval, pack, unpack

```

```
c read the user supplied parameters
  open (unit=5,file='eosmix.dat')
  read(5,*) header
  read(5,*) numeos, filename1, filename2, filename3, wtp
  close(5)

c read the first dataset
  open(unit=5, file=filename1)
  read(5,*) dummy
  read(5,*) nonum, zbar1, abar1, rho1, n1
  read(5,*) (array1(i), i=1,n1)
  close(5)

c read the second dataset
  open(unit=5, file=filename2)
  read(5,*) dummy
  read(5,*) nonum, zbar2, abar2, rho2, n2
  read(5,*) (array2(i), i=1,n2)
  close(5)

c evaluate zbar, abar and rho
  zbar3 = (1.-wtp)*zbar1 + wtp*zbar2
  abar3 = (1.-wtp)*abar1 + wtp*abar2
  rho3 = (1.-wtp)*rho1 + wtp*rho2

c -----
c move input 1-d arrays into p1(nd,nt) and p2(nd,nt) 2-d arrays
c * for opacities, this is Rosseland and Planck opacities
c * for EOS it's pressures and energies
c -----

c unpack first array
  call unpack(array1,d1,t1,p1f1,p2f1,nd1,nt1,incr)

c check incr=n1 at this point, otherwise STOP
  if(incr.ne.n1)then
    open(unit=8, file='test.dat')
    write(8,*) 'STOP at increment check n1'
    stop
  endif

c unpack second array
  call unpack(array2,d2,t2,p1f2,p2f2,nd2,nt2,incr)

c check incr=n2 at this point, otherwise STOP
  if(incr.ne.n2)then
    open(unit=8, file='test.dat')
    write(8,*) 'STOP at increment check n2'
    stop
  endif

c -----
c Establish the output array size
c -----
```

```

c find the maximum values of n and T in file 2
    dmax2 = xmaxval(d2,nd2)
    tmax2 = xmaxval(t2,nt2)

c truncate the arrays, if needed:
c   find the largest value of (d1,t1) which are smaller than (d2,t2)
    i=nd1
    do while(d1(i).gt.dmax2)
        i=i-1
    enddo
    nd1 = i

    i=nt1
    do while(t1(i).gt.tmax2)
        i=i-1
    enddo
    nt1 = i

c the new maximum values of d1 and t1:
    dmax1 = d1(nd1)
    tmax1 = t1(nt1)

c -----
c Interpolate
c -----
c we need to evaluate the second data set at the (n,T)
c values of the first data set (by linear interpolation)
c (n,T) increments: (i,j) for first file, (m,n) for second

c It is assumed that d1(1)=d2(1) and t1(1)=t2(1)
c If not, then stop
    res = 1.e-6
    dcheck=abs(d1(1)-d2(1))/(d1(1)+d2(1))
    tcheck=abs(t1(1)-t2(1))/(t1(1)+t2(1))
    if(dcheck.gt.res) then
        open(unit=8, file='test.dat')
        write(8,*) 'STOP at d1(1)=d2(1)'
        stop
    endif
    if(tcheck.gt.res) then
        open(unit=8, file='test.dat')
        write(8,*) 'STOP at t1(1)=t2(1)'
        stop
    endif

c for each j of the first array we need the n point where Tn>Tj
    do j=1,nt1
        n=2
        do while (n.le.nt1 .and. t2(n).le.t1(j))
            n=n+1
        enddo
        gp = (t1(j)-t2(n-1))/(t2(n)-t2(n-1))
        gm = 1.-gp

c for each i of the first array we need the m point where dm>di
    do i=1,nd1

```

```

      m=2
      do while (m.le.nd1 .and. d2(m).le.d1(i))
        m=m+1
      enddo
      fp = (d1(i)-d2(m-1))/(d2(m)-d2(m-1))
      fm = 1.-fp

c now form the linear combinations
      p1f2i(i,j) = fp * gp * p1f2(m,n)
      .           + fp * gm * p1f2(m,n-1)
      .           + fm * gm * p1f2(m-1,n-1)
      .           + fm * gp * p1f2(m-1,n)
      p2f2i(i,j) = fp * gp * p2f2(m,n)
      .           + fp * gm * p2f2(m,n-1)
      .           + fm * gm * p2f2(m-1,n-1)
      .           + fm * gp * p2f2(m-1,n)
      enddo
      enddo

c now that we have the interpolated arrays, we simply
c weight the two datasets to form the output
      do j=1,nt1
      do i=1,nd1
        p1f3(i,j) = (1.-wtp)*p1f1(i,j) + wtp*p1f2i(i,j)
        p2f3(i,j) = (1.-wtp)*p2f1(i,j) + wtp*p2f2i(i,j)
      enddo
      enddo

c -----
c pack the output linear array for writing to the file
c -----

      call pack(array3,d1,t1,p1f3,p2f3,nd1,nt1,incr)

c check incr=n3 at this point, otherwise STOP
      n3 = 2 + nd1 + nt1 + 2*(nd1*nt1)
      if(incr.ne.n3)then
        open(unit=8, file='test.dat')
        write(8,*) 'STOP at increment check n3'
        write(8,*) 'incr=',incr,', n3=',n3
        stop
      endif

c -----
c OUTPUT
c -----

      open(unit=7, file=filename3)
      write(7,*) header
      write(7,1) numeos, zbar3, abar3, rho3, n3
      write(7,2) (array3(i), i=1,n3)
      close(7)

1 format(1x,i5,4x,1p3e15.8,3x,i5)
2 format(1p5e15.8)

```



```

        stop
        end

c *****
c EXTERNAL FUNCTION XMAXVAL
      function xmaxval(a,na)
        real*4 a(100)
        xmaxval=0.
        do i=1,na
          if(a(i).gt.xmaxval) xmaxval=a(i)
        enddo
        return
        end

c *****
c UNPACK a linear array into d(nd), t(nt), p1(i,j), p2(i,j)
      subroutine unpack(a,d,t,p1,p2,nd,nt,incr)
        real*4 a(10000), d(100), t(100), p1(100,100), p2(100,100)

c (0.01 is to avoid roundoff errors in integers)
        nd = aint(a(1)+0.01)
        nt = aint(a(2)+0.01)
        incr = 2

        do i=1,nd
          incr=incr+1
          d(i) = a(incr)
        enddo
        do i=1,nt
          incr=incr+1
          t(i) = a(incr)
        enddo

        do j=1,nt
          do i=1,nd
            incr=incr+1
            p1(i,j) = a(incr)
          enddo
        enddo
        do j=1,nt
          do i=1,nd
            incr=incr+1
            p2(i,j) = a(incr)
          enddo
        enddo
        return
        end

c *****
c PACK 2d arrays d(nd), t(nt), p1(i,j), p2(i,j) into a
      subroutine pack(a,d,t,p1,p2,nd,nt,incr)
        real*4 a(10000), d(100), t(100), p1(100,100), p2(100,100)

        a(1) = nd
        a(2) = nt

```

```
incr = 2

do i=1,nd
  incr=incr+1
  a(incr) = d(i)
enddo
do i=1,nt
  incr=incr+1
  a(incr) = t(i)
enddo

do j=1,nt
do i=1,nd
  incr=incr+1
  a(incr) = p1(i,j)
enddo
enddo
do j=1,nt
do i=1,nd
  incr=incr+1
  a(incr) = p2(i,j)
enddo
enddo
return
end
```